BROADBAND GROUND MOTION SIMULATION WITHIN DUZCE CITY (TURKEY)

A THESIS SUBMITTED TO
THE GRADUATE SCHOOL OF NATURAL AND APPLIED SCIENCES
OF
MIDDLE EAST TECHNICAL UNIVERSITY

BY

EKİN ÖZMEN

IN PARTIAL FULFILLMENT OF THE REQUIREMENTS
FOR
THE DEGREE OF MASTER OF SCIENCE
IN
EARTHQUAKE STUDIES

JANUARY 2019

Approval of the thesis:

BROADBAND GROUND MOTION SIMULATION WITHIN DUZCE CITY (TURKEY)

submitted by **EKIN ÖZMEN** in partial fulfillment of the requirements for the degree of **Master of Science in Earthquake Studies Department, Middle East Technical University** by,

Prof. Dr. Halil Kalıpçılar
Dean, Graduate School of **Natural and Applied Sciences** ________________

Prof. Dr. Ayşegül Askan Gündoğan
Head of Department, **Earthquake Studies** ________________

Prof. Dr. Ayşegül Askan Gündoğan
Supervisor, **Earthquake Studies, METU** ________________

Prof. Dr. Sevtap Ayşe Kestel
Co-Supervisor, **Institute of Applied Mathematics, METU** ________________

Examining Committee Members:

Prof. Dr. Murat Altuğ Erberik
Civil Engineering Dept., METU ________________

Prof. Dr. Ayşegül Askan Gündoğan
Earthquake Studies, METU ________________

Prof. Dr. Sevtap Ayşe Kestel
Institute of Applied Mathematics, METU ________________

Assoc. Prof. Dr. Berna Unutmaz
Civil Engineering Dept., HU ________________

Assist. Prof. Dr. Onur Pekcan
Civil Engineering Dept., METU ________________

Date: 29.01.2019

I hereby declare that all information in this document has been obtained and presented in accordance with academic rules and ethical conduct. I also declare that, as required by these rules and conduct, I have fully cited and referenced all material and results that are not original to this work.

Name, Surname: Ekin Özmen

Signature:

ABSTRACT

BROADBAND GROUND MOTION SIMULATION WITHIN DUZCE CITY (TURKEY)

Özmen, Ekin
Master of Science, Earthquake Studies
Supervisor: Prof. Dr. Ayşegül Askan Gündoğan
Co-Supervisor: Prof. Dr. Sevtap Ayşe Kestel

January 2019, 127 pages

Earthquakes have more hazardous and devastating effects in populated areas. To prevent damage and reduce the risks, broadband records are collected to use in the seismic hazard assessment and engineering seismology. In areas with significant seismic activity and insufficient seismic networks, the simulated ground motions become more important.

Broadband ground motion simulations are performed for 12 November 1999 Duzce earthquake. Deterministic simulations are performed for low frequency part and stochastic simulations are performed for high frequency part of the ground motion record. Broadband ground motion simulations are done using EXSIM program for the stochastic high frequency portion of the ground motion and COMPSYN program for the deterministic low frequency portion.

The comparisons of the real and simulated ground motion simulations are done in both time and frequency domains. For comparisons, four stations are selected, namely BOL, DZC, GYN and SKR which are located near Duzce City. Comparisons of observed damage with the distribution of simulated ground motion are also given. Additionally, attenuation of simulated data is compared against ground motion prediction equations.

Finally, simulated records of the 12 November 1999 Duzce earthquake are used in dynamic response analysis of three selected frames. The responses from simulated data is compared with those from the real data.

Keywords: Broadband ground motion simulation, stochastic finite-fault model, deterministic approach, building response simulation

ÖZ

DÜZCE ŞEHRİ (TÜRKİYE) GENİŞ BANTLI YER HAREKETİ SİMÜLASYONU

Özmen, Ekin
Yüksek Lisans, Deprem Çalışmaları
Tez Danışmanı: Prof. Dr. Ayşegül Askan Gündoğan
Ortak Tez Danışmanı: Prof. Dr. Sevtap Ayşe Kestel

Ocak 2019, 127 sayfa

Büyük nüfuslu bölgelerde, depremler daha tehlikeli ve yıkıcı hale gelir. Hasarı önlemek ve tehlikeyi azaltmak için, sismik tehlike analizi ve mühendislik sismolojisinde geniş bantlı kayıtlar toplanmaktadır. Sismik aktivite olarak önemli olan ve yetersiz sismik ağı bulunan alanlarda, simule edilmiş yer hareketi daha da önem kazanmaktadır.

Geniş bantlı yer hareketi simulasyonları 12 Kasım 1999 Düzce Depremi için yapılmıştır. Yer hareketi kaydının düşük frekans kısmı için deterministik, yüksek frekans kısmı için ise stokastik yöntem kullanılmıştır. Geniş bantlı yer hareketi simulasyonları, yer hareketi kaydının frekans bölgesi yüksek frekans aralığı olan stokastik simulasyon için EXSIM ve yer hareketi kaydının frekans bölgesi düşük frekans aralığı olan deterministik simulasyon için COMPSYN programları kullanılarak yapılmıştır.

Gerçek ve simüle edilmiş yer hareketi simülasyonlarının karşılaştırmaları zaman ve frekans alanında yapılmıştır. Karşılaştırmalar için Düzce şehri yakınlarında yer alan BOL, DZC, GYN ve SKR olmak üzere dört istasyon seçilmiştir. Simüle edilmiş yer hareketi dağılımı ile gözlemlenen hasar karşılaştırmaları verilmektedir. Ek olarak, yer hareketi tahmin denklemleri ile sentetik azalımlar uygulanmıştır.

Son olarak, 12 Kasım 1999 Duzce Depremi'nin bina tepki simülasyon kayıtları üç çerçeve sistem için uygulanmıştır. Simüle edilmiş verilerden gelen davranışlar, gerçek verilerden gelenler ile karşılaştırılmıştır.

Anahtar Kelimeler: Geniş bantlı yer hareketi simulasyonu, stokastik sonlu fay modeli, deterministik yaklaşım, bina tepkisi simülasyonu

To my advisors, my family and my friends

ACKNOWLEDGMENTS

I want to firstly thank my hardworking, endearious, heartening advisor Prof. Dr. Ayşegül Askan Gündoğan. She taught me not only researching, she taught to be curious about everything in the world, to desire for learning. The most important thing that I learned from her is that success is not for us but for humanity.

I want to thank my co-advisor Prof. Dr. Sevtap Ayşe Kestel for her help during my thesis. The study is developed under her guidance.

I want to thank Shaghayegh Naghshineh. Her support and teaching were eternal. In all steps of the project, everything that I have learned in this area, there is her labor. Thanks to A-team and Fatma Nurten Şişman for being always positive and helpful.

I am very lucky to have my family near me. I would like to thanks them waiting for me until and after midnight during my studies, giving support all the time and believing me. Without my mother, father, sister and lovely dog Piksel, I could not finish this thesis.

Also, I would also to thank my best friend, lovely husband Emre Özmen for giving his support and power not only during my thesis, as always.

The person gives me the first reason to want to be an earthquake engineer is Elena Salsano. Even being so far in kilometers, she is always so close to me as a colleague, friend and sister.

TABLE OF CONTENTS

LIST OF TABLES

TABLES

LIST OF FIGURES

FIGURES

CHAPTER 1

INTRODUCTION

1.1. General

Earthquakes affect urban areas with dense population significantly. Study of ground motion records is necessary not only for explaining past earthquakes but also for damage reduction and risk mitigation. Despite the growing seismic networks all over the world, there are still regions with significant seismic activity but insufficient networks. In such areas, simulations are vital for both seismological and earthquake engineering purposes.

Strong ground motion simulations are performed with the help of advanced mathematics, numerical analysis and geophysics theory. To obtain realistic ground motion simulations, the specific seismological properties of the study area such as site conditions, velocity and density properties and wave propagation properties should be well known.

Broadband ground motion simulations are obtained by two methods: Deterministic and stochastic. Deterministic approach uses numerical solutions for full-wave propagation. For higher frequencies, due to the need for very detailed earth-velocity structure information, the deterministic approach is unfavorable. Stochastic simulations give reliable results for higher frequencies by taking into account the inherent randomness of ground motion simulations.

In this thesis, both deterministic and stochastic solutions are used to obtain simulated ground motions over a broadband frequency range. Results from both techniques are summed up to yield hybrid broadband for motions.

The study area is selected as Düzce City, which is located in Turkey. More than 90 % of the total area is located in seismically active regions and unfortunately, more than 95 % of population of Düzce City is under earthquake threat. The solution that is used in this thesis, has inside rapid ground and structural vulnerability assessment techniques.

1.2. Literature Survey

To model broadband ground motion simulations, the solution is done by two approaches with respect to their frequency range: Low frequency region which is generally up to 1~2 Hz approximately and high frequency region mostly beyond 1~2 Hz.

For low frequency (long period) part of ground motions, deterministic solution is used. There are some different numerical methods for solving the corresponding partial differential equations. Some of the numerical methods used are finite difference (e.g.: Frankel and Vidale, 1992; Frankel, 1993; Yomogida and Egten, 1993; Olsen *et al.*, 1996; Olsen and Archuleta, 1996; Moczo *et al.*, 2002), boundary-element (e.g.: Kawase, 1988; Luco *et al.*, 1990; Pedersen *et al.*, 1994), finite element (e.g.: Li *et al.*, 1992; Rial *et al.*, 1992; Toshinawa and Ohmachi, 1992; Bao *et al.*, 1998) and the spectral element methods (e.g.: Cohen *et al.*, 1993; Priolo *et al.*, 1994; Komatitsch, 1997; Komatitsch and Vilotte, 1998; Komatitsch and Tromp, 1999; Komatitsch *et al.*, 2004).

Another deterministic technique is theoretical Green's function for an elastic layered medium for the solution of low frequencies (Bouchon, 1981; Hisada, 1994; Chen and Zhang, 2001). The empirical Green's function technique is an alternative method, which constructs the ground motion simulations for large earthquakes by superposing small ground motions, is introduced by Hartzell (1978) and advanced by Irikura (1986).

For high frequency part of ground motions, stochastic methods are used, because of the properties the seismic waves in that frequency region are random in nature. In addition, using deterministic approach solutions is not always feasible in the high frequency range.

The original modeling of the time histories by ground motion simulations using the stochastic method is introduced by Housner, (1947; 1955) and Thomson (1959). Further developments are done by Aki (1967) by improving the source model that decreases with the square of frequency (ϖ^2) in proportion. Later, it was found that the high frequency portion of the ground motions can be modeled with Gaussian white noise (Hanks and McGuire, 1981). This methodology is combined with the source model that was introduced by Aki (1967) and developed later by Brune (1971) that the source–time function is estimated from the effective stress near the fault plane (Boore, 1983). This method by Boore (1983) is named as stochastic point–source modeling and further modified by Beresnev and Atkinson for near–fault effects, which divides the fault into sub faults. These sub faults each represent a point–source and the ground motion is found by the combination of effects of all sub faults. Stochastic point–source modeling is improved by adding the dynamic corner concept (Motazedian and Atkinson, 2005). In this approach, the corner frequency reduces in inverse proportion with the ruptured area while the rupture propagates.

This study utilizes the combination of the DWFE using one-dimensional Green's function technique (Olson *et al.*, 1984; Spudich and Archuleta, 1987) for low frequencies and stochastic finite–fault methodology with dynamic corner frequency approach for high frequencies. The methods are applied to the 1999 Duzce earthquake. Necessary literature will be added throughout the text.

Stochastic ground motion simulation applications are frequently used all over the globe. Chronologically, Hanks and McGuire (1981), Boore (1983) and Motazedian and Atkinson (2005) studied earthquake ground motion simulations in California, Atkinson (1984), Boore and Atkinson (1987), Toro and McGuire (1987) studied in

North America, and Hanks and Boore (1984), Atkinson and Silva (2000) in Western America. The method is also applied in Italy by Castro *et al.* (2001 & 2008), Galluzzo *et al.* (2008), Ugurhan *et al.* (2012) and Karimzadeh *et al.* (2017a), in Iran by Motazedian and Moinfar (2006), Shoja-Taheri and Ghofrani (2007), in India by Raghukanth and Somala (2009). Stochastic method is also applied in some regions in Turkey: For the 1998 Ceyhan Earthquake by Yalcinkaya (2005), the 1999 Duzce earthquake by Ugurhan and Askan (2010), Karimzadeh *et al.* (2017a), for the 1992 Erzincan earthquake by Askan *et al.* (2013), for the Van 2011 earthquake by Akinci and Antonioli (2013), Zengin and Cakti (2014).

The hybrid methods are also studied by several researches in the past (e.g.: Kamae *et al.*, 1998; Pitarka *et al.*, 2000; Hisada and Bielak, 2003; Pulido *et al.*, 2004; Pacor *et al.*, 2005; Ameri *et al.*, 2008; Hisada, 2008; Nickham and Eslamian, 2010; Baykal *et al.*, 2012; Ameri *et al.*, 2011; Shahjouei and Pezeshk, 2015).

1.3. Objective and Scope

Broadband ground motion simulations are performed for 12 November 1999 Duzce earthquake. Deterministic approach is performed for the low frequency part and stochastic simulations are performed for the high frequency part of the ground motion records. Broadband ground motion simulations are performed using two different algorithms to simulate the low and high frequencies. The low frequency portion is simulated by COMPSYN program (Spudich and Xu, 2003) which is a common open source software that involves the numerical algorithms by Spudich and Archuleta (1987) for simulations with Discrete Wavenumber Finite Element (DWFE) method. It should be noted that COMPSYN program has some limitations for stations very close to a surface fault rupture, for equal fault and station depths, and lastly for inadequate sampling for stations very close to a fault (Spudich and Xu, 2003). For simulating the high frequency portion of ground motions, EXSIM (Motazedian and

Atkinson, 2005) is used in which stochastic finite–fault method based on a dynamic corner frequency approach is implemented.

In Chapter 2, broadband ground motion simulation methodology is presented. In the beginning of that chapter, broadband (hybrid) ground motion simulation methodology is explained. Later, theories for the stochastic and deterministic ground motion simulations are presented in detail. The stochastic modeling is presented in two parts: Stochastic point–source modeling and stochastic finite–fault modeling. The input parameters for stochastic and deterministic modeling are also described.

In Chapter 3, broadband ground motion simulations of the 12 November 1999 Duzce earthquake is presented. The study area is briefly mentioned and the strong ground motion database and the selection of input parameters for stochastic and deterministic modeling are given. The results are discussed by comparing the observed and simulated ground motion data for selected stations. The comparisons of simulated peak amplitudes with empirical estimates from GMPE's are represented. Next, ground motion simulations of selected stations are performed for the 1999 Duzce earthquake ($M_w = 7.1$). Additionally, scenario earthquakes are modeled for different moment magnitudes at 48 nodes in a selected region where the epicenter of 1999 Duzce earthquake is located. In the last part of this chapter, application of attenuation of simulated data with GMPE's and comparisons of observed damage with the distribution of these simulated ground motions are presented.

In Chapter 4, dynamic responses of selected three frames due to the simulated records of 1999 Duzce earthquake are presented. The methodology used for dynamic analysis of buildings are explained. OpenSees platform (http://opensees.berkeley.edu) which uses finite element method is employed for dynamic analysis of buildings. OpenSees platform has some limitations on graphical user interface (GUI) and library of reference material (http://opensees.berkeley.edu). The responses from simulated data is compared against the corresponding real data of 1999 Duzce earthquake.

In Chapter 5, the summary and conclusions of the study are presented. Future recommendations are also stated.

CHAPTER 2

A BROADBAND GROUND MOTION SIMULATION METHODOLOGY

2.1. General

This chapter presents the broadband ground motion simulation approach used for the 12 November 1999 Duzce earthquake.

In Section 2.2, the broadband (hybrid) ground motion simulation approach is explained in detail. In Section 2.3, the stochastic strong ground motion simulation methodology is presented. The details of stochastic point-source modeling and stochastic finite-fault modeling are given in Section 2.3. In Section 2.4, deterministic strong ground motion simulation methodology is explained.

2.2. Broadband (Hybrid) Ground Motion Simulation Approach

A hybrid ground motion simulation methodology is the combination of a stochastic method for high frequencies and a deterministic approach for low frequencies. Broadband frequencies are generally defined as 0.10 Hz ≤ f ≤ 10 Hz in engineering interest. Deterministic approach gives reasonable results for frequencies generally up to approximately 1-2 Hz.

In this study, the broadband ground motions are obtained by combining low and high frequencies following the hybridization approach of Mai and Beroza (2003) as implemented in Moratto *et al.* (2015). The Fourier amplitude spectra of low and high frequency seismograms are combined in the frequency domain as given in Equation (2.1) (Mai and Beroza, 2003):

$$A(f) = A^{LF}(f) \cdot W^{LF}(f) + A^{HF}(f) \cdot W^{HF}(f) \qquad (2.1)$$

where $A(f)$ is the broadband spectrum, $A^{LF}(f)$ is the low frequency spectrum and $A^{HF}(f)$ is the high frequency spectrum. $\mathrm{W}^{\mathrm{LF}}(\mathrm{f})$ and $W^{HF}(f)$ are the smoothed frequency-dependent weighing functions for the low and high frequencies, respectively.

The low frequency results are taken from the deterministic solution, while the high frequency results are taken from the stochastic solution. Because of the combination, there can be some potential uncertainties. As a result, the average ratio of HF / LF velocity amplitude spectra is used as a scaling ratio. The ratio is given in a previously defined frequency range which is connected with the deterministic-stochastic transition. The ratio is applied to scale the stochastic frequency part to deterministic frequency part. While solutions are obtained in the time domain, and with the Fourier transformation the broadband ground motions are formed in the frequency domain. To obtain the final results in the time domain, inverse Fourier transformation is applied.

In Figure 2.1, the flowchart for the broadband ground motion simulation algorithm used in this thesis is given with the related frequency ranges for each simulation method. In general, the higher frequency limit for deterministic ground motion simulations is given as 1 Hz. On the other hand, this cross-over limit can change for different seismic regions approximately up to 2 Hz.

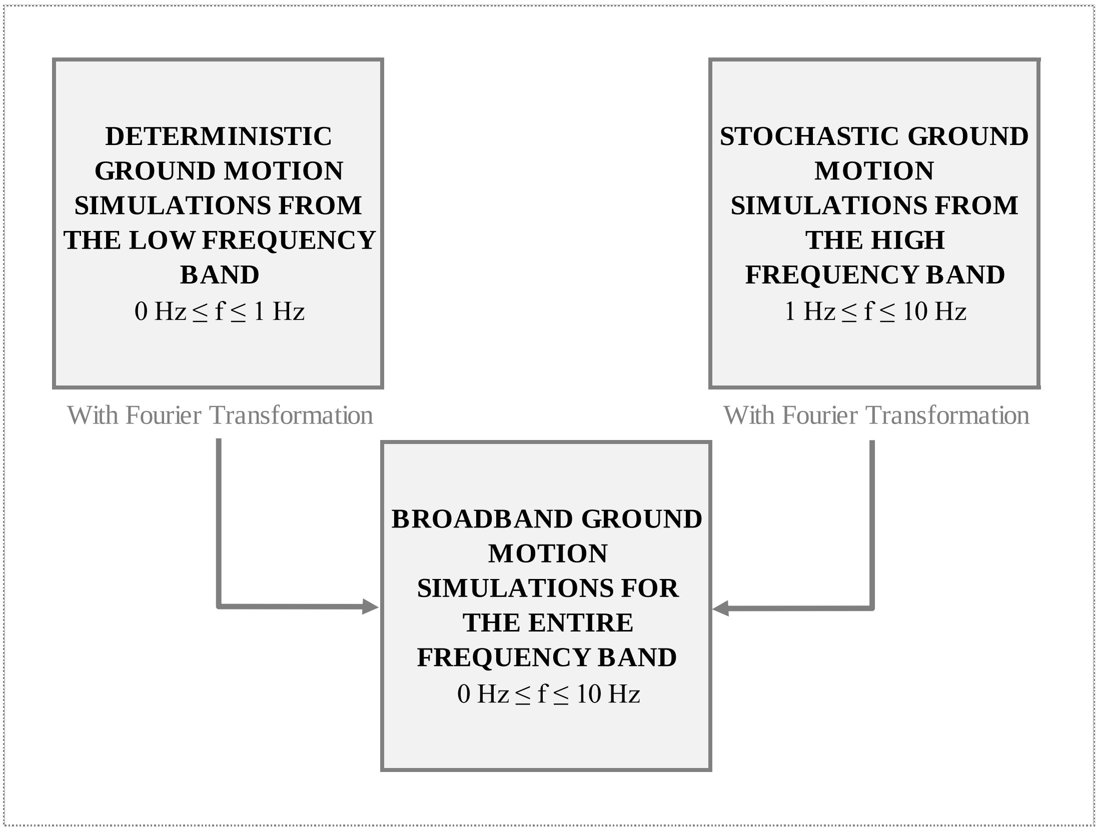

Figure 2.1. Flowchart for broadband ground motion simulation results

2.3. Stochastic Strong Ground Motion Simulation Methodology

Stochastic approach is used for high frequencies since the high frequency ground motions are random in nature. These frequencies are generally higher than 1 Hz. To use deterministic approaches in higher frequencies, detailed soil profiles are necessary which is generally not possible due to lack of information on site conditions. Stochastic strong ground motion simulation method can be divided into two methods: Stochastic point-source modeling and stochastic finite-fault modeling.

2.3.1. Stochastic Point-Source Modeling

The research on study of the stochastic point-source modeling taken its origin from the study of Hanks and McGuire (1981).

Based on this study, to model high frequency part of S-waves in acceleration-time series, a method is developed by Boore (1983) where shear waves can be presented as finite duration, band–limited, white Gaussian noise. The finite duration is $0 \leq t - \frac{R}{\beta} \leq T_d$. In this interval, R is the source to receiver distance; β is the shear–wave velocity and T_d is the faulting duration. The band can be presented with the frequency interval of $f_0 \leq f \leq f_{max}$ where f_0 is the corner-frequency of the far-field shear radiation and f_{max} is the highest frequency recorded by the seismometer. With this methodology, the objective is to generate a transient time series where amplitude spectrum matches the desired spectrum.

In this modeling approach by Boore (1983), first, random band-limited Gaussian white noise is generated with a unit variance for a specified finite duration of motion. This noise is windowed by Saragoni-Hart or boxcar windows to get more realistic acceleration-time series. By transforming the ground motions from the time domain to the frequency domain, the amplitudes are normalized by cutting the frequencies above the cut-off frequency (Brune, 1970). After, the modeled and shaped-noise spectrum is transferred by inverse Fourier transformation to stochastic acceleration-time series (Boore, 2003). The steps are demonstrated in Figure 2.2.

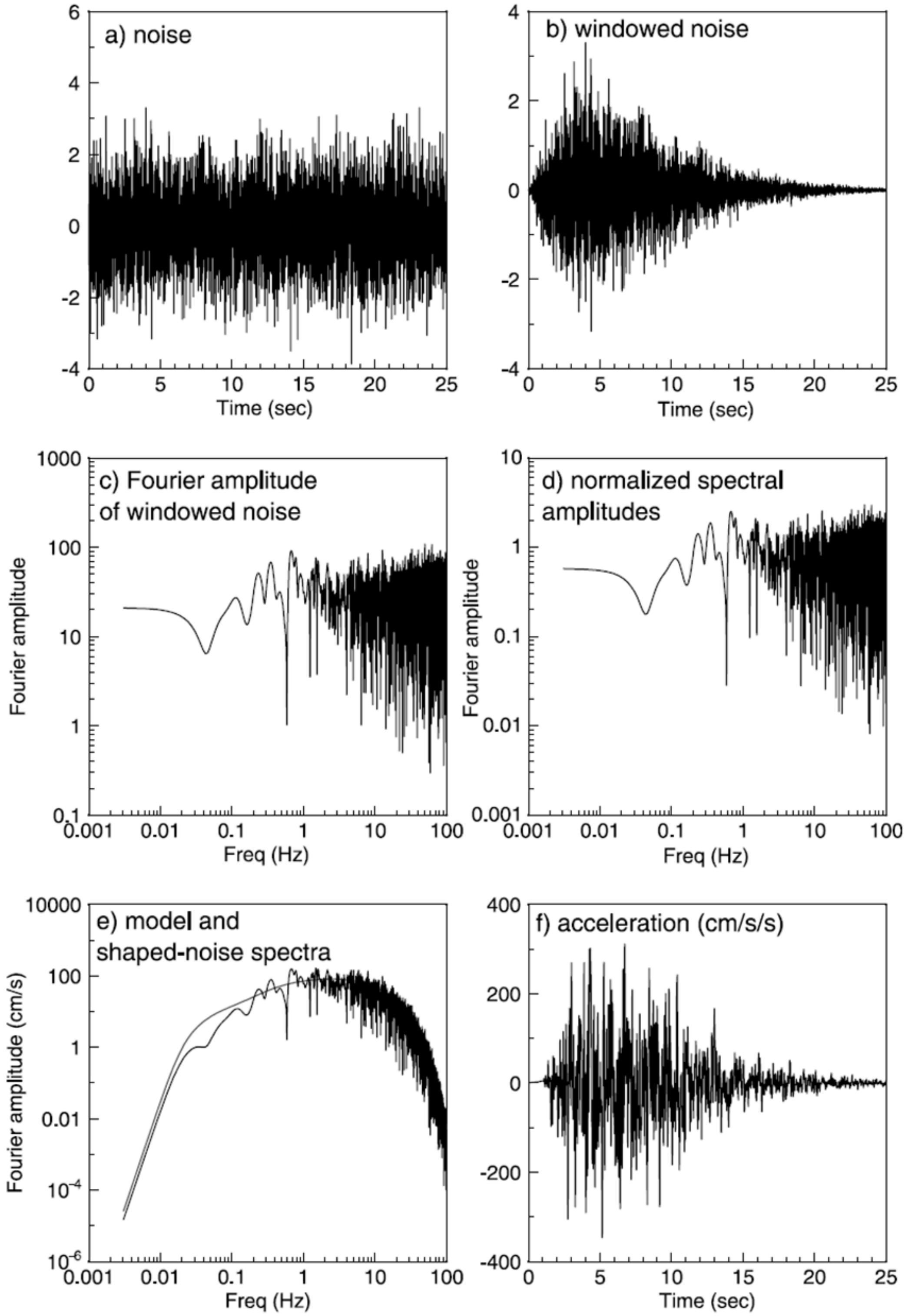

Figure 2.2. Flowchart for point-source stochastic ground motion simulation (Adapted from Boore, 2003)

Stochastic ground motion modeling is based on two parts: The stochastic time series and Green's function solution of elastic wave propagation equation. Hanks and McGuire (1981) decreased the misfits in estimating peak ground accelerations by the $\bar{\omega}^2$ spectrum (Aki, 1967).

The filter functions are defined as the source function $E(M_0, \omega)$, path function $P(R, \omega)$, site function $G(\omega)$ and the instrument response $I(\omega)$. Fourier Amplitude Spectrum of a seismic signal in stochastic point-source modeling is given as:

$$A(M_0, R, \omega) = E(M_0, \omega) \cdot P(R, \omega) \cdot G(\omega) \cdot I(\omega) \tag{2.2}$$

where M_0 is the seismic moment, ω is the frequency and R is the source to receiver distance. Next, these filter functions will be described briefly.

2.3.1.1. The Source Function

The source function is dependent on earthquake magnitude, frequency, source-time function and the shear modulus of the earth material at fault depth. The definition of the source function where the far-field shear wave displacement is in a homogeneous, isotropic and unbounded medium due to a point shear dislocation is as follows:

$$u(x, t) = \frac{\Re^{\theta\gamma}}{4\pi\rho\beta^3 R} \cdot M'(t) \cdot \left(t - \frac{R}{\beta}\right) \tag{2.3}$$

where $u(x, t)$ is the dynamic displacement field at point x and at time t, $\Re^{\theta\gamma}$ is the radiation pattern reflecting the variation of the displacement field for different directions due to a shear dislocation, ρ is density, and lastly β is shear wave velocity, R is the source to receiver distance and $M'(t)$ is the time derivative of the seismic moment $M(t)$ (Aki and Richards, 1980).

The seismic moment is given in as follows

$$M(t) = \mu \cdot \bar{u}(t) \cdot A \tag{2.4}$$

where μ is the shear modulus or rigidity at the crustal level, $\bar{u}(t)$ is the source-time function and A is the dislocation area.

The source-time function has indefinite characteristics: The representation of the seismic displacements is evaluated as a step function by Aki (1967), while Haskell (1964) utilized as a ramp function. In the stochastic point–source modeling, the source-time function derived by Brune (1970) is used. This function is modified by Beresnev and Atkinson (1997) as follows:

$$\bar{u}(t) = \frac{\sigma}{\mu} \cdot \beta \cdot \tau \cdot \left[1 - \left(1 + \frac{t}{\tau}\right) \cdot e^{-\frac{t}{\tau}}\right] \tag{2.5}$$

whereas -the velocity is:

$$\overline{u'}(t) = \frac{\sigma}{\mu} \cdot \beta \cdot \left(\frac{t}{\tau}\right) \cdot \left(e^{-\frac{t}{\tau}}\right) \tag{2.6}$$

where τ is the time parameter which controls the rate of displacements and σ is the effective stress which acts on the dislocation surface.

Using Equation (2.4), Equation (2.3) is modified as:

$$u(x,\omega) = \frac{\Re^{\theta\gamma} M_0}{4\pi\rho\beta^3 R} \cdot \left(\frac{t - \frac{R}{\beta}}{\tau}\right) \cdot e^{-\frac{\left[t - \frac{R}{\beta}\right]}{\tau}} \tag{2.7}$$

The Fourier transformation of Equation (2.7) is then as follows:

$$u(x,\omega) = \frac{\Re^{\theta\gamma} M_0}{4\pi\rho\beta^3 R} \cdot \left[\frac{1}{1 + \left(\frac{\omega}{\omega_c}\right)^2}\right] \tag{2.8}$$

Brune (1-970, 1971) derived the corner frequency as $f_c = \omega_c/2\pi$. Here the corner frequency is explicitly expressed as:

$$f_c = 4.9 \times 10^6 \cdot \beta \cdot \left(\frac{\Delta\sigma}{M_0}\right)^{1/3} \tag{2.9}$$

where the corner frequency f_c is presented in Hertz (Hz), shear-wave velocity β in km/sec, stress drop $\Delta\sigma$ in bars and the seismic moment M_0 in dyne·cm.

The source function is expressed in general in terms of constants C, seismic moment and source displacement spectrum as:

$$E(M_0, \omega) = C \cdot M_0 \cdot S(\omega, \omega_c) \tag{2.10}$$

C is the combination of constants given in Equation (2.8) expressed as:

$$C = \frac{\mathfrak{R}^{\theta\gamma} \cdot FS \cdot PRTITN}{4\pi\rho\beta^3} \tag{2.11}$$

where FS is the free surface amplification factor which is assumed as 2 in general. $PRTITN$ is a factor which is applied to reflect the effect of shear–wave energy partitioning into two horizontal components. Its value is taken as $1/\sqrt{2}$ in general. $\mathfrak{R}^{\theta\gamma}$ is the radiation pattern constant and taken to be 0.55 for shear waves.

As stated in Equation (2.4), the seismic moment of an earthquake is represented by M_0. The relationship between M_0 and moment magnitude, M_w derived by Hanks and Kanamori (1979) is stated as follows:

$$log\, M_0 = 1.5\, log\, M_w + 16.1 \tag{2.12}$$

Thus, the source displacement spectrum is defined based on previous derivations as follows:

$$S(\omega, \omega_c) = \frac{1}{1 + \left(\frac{\omega}{\omega_c}\right)^2} \quad (2.13)$$

The source effects are complex and mostly not well known. Thus, the accuracy of the ground motion simulations is directly affected by the source model. The simulation of the low frequency portion is particularly difficult in large earthquakes if the source effects are not well-defined (Askan *et al.*, 2013).

2.3.1.2. The Path Function, P(R,ω)

The path function is used to model the changes in characteristics of seismic waves while traveling through the layers of earth. The path function parameters are geometric spreading, quality factor (anelastic attenuation factor) and duration functions.

Geometric spreading can be defined as a factor that reflects wave amplitude reduction because of the traveled distance of seismic waves. If Earth was thought as a homogeneous spherical body, the geometric spreading can be expressed inversely proportional to the distance, R. Since, Earth is not a homogeneous body, thus the definition of geometric spreading becomes more difficult.

The path function used in stochastic modeling is given in as follows:

$$P(R, \omega) = Z(R) \cdot e^{\frac{\pi f R}{Q(f)\beta}} \quad (2.14)$$

where $Z(R)$ is the geometric spreading, $Q(f)$ is the frequency–dependent quality factor.

The geometric spreading term is defined as a piecewise continuous function:

$$Z(R) = \begin{Bmatrix} \frac{R_0}{R}, & R \le R_1 \\ Z(R_1)\left(\frac{R_1}{R}\right)^{p_1}, & R_1 \le R \le R_2 \\ \vdots & \\ Z(R_n)\left(\frac{R_n}{R}\right)^{p_n}, & R \le R_n \end{Bmatrix} \quad (2.15)$$

The $e^{\frac{\pi f R}{Q(f)\beta}}$ term is the representation of anelastic attenuation which affects directly the high frequency spectrum shape (Motazedian, 2006). The frequency-dependent anelastic attenuation expressed in terms of quality factor function is given as follows:

$$Q(f) = Q_0 f^n \quad (2.16)$$

A duration function is required to obtain the time history of ground motion simulations. The function used in stochastic modeling is given as folllows:

$$T = T_0 + b \cdot R_{hypo} \quad (2.17)$$

where T_0 is the source duration that increases proportional to the size of an earthquake, b is a region-dependent parameter and R_{hypo} is the hypocentral distance (Atkinson and Boore, 1995).

2.3.1.3. The Site Function

The amplification and diminution of the strong ground motions are affected by the soil profile of the site. The site function is related to reflection and refraction processes within the heterogeneous Earth structure at the sites. The most important function parameters are soil type, layer thickness, and wave velocity. One-dimensional soil layers can be used for practically.

The frequency content, seismic wave amplitude and duration are affected by site conditions. The soil density and velocity decrease from deeper soil layers to surface level in general. Therefore, the seismic impedance also decreases. Thus, as Kramer

(1996) stated that wave amplitudes must increase for conserving elastic wave energy. However, the amplitude can also decrease because of seismic wave damping that occur in softer soils. As a result, the site function used in stochastic modeling of ground motions is expressed by multiplication of an amplification function, $A(f)$, and a diminution function, $D(f)$, as follows:

$$G(f) = A(f) \cdot D(f) \tag{2.18}$$

Amplification function is one of the important functions used in simulating ground motions. To determine amplification factors, several methods are used. The theoretical method, the most frequently used and the most accurate one, can be used with a well-defined velocity profile at a site.

Velocity profiles can be obtained by invasive in-situ techniques, such as borehole drilling, are expensive and applied in shallows layers only. For this reason, surface waves are measured in a broadband frequency range as an alternative method to obtain velocity profiles. Some “active sources” are used in surface wave methods such as hammers, electromechanical shakers, weight drops, bulldozers and seismic vibrators. Two popular techniques in surface wave measurement are defined by Stokoe *et al.* (1994) as spectral analysis of surface waves (SASW) and by Park *et al.* (1999) as Multi-Channel array surface waves (MASW).

When a well-defined velocity profile is obtained, the site amplifications can be estimated in one-dimension (1D) (Haskell, 1960; Schnabel *et al.*, 1972; Kennett, 1983). With this method, through infinite horizontal soil layers, wave propagation is solved in 1D to obtain the theoretical transfer function. This amplification functions can also be obtained by two-dimensional (2D) (Sánchez–Sesma, 1987) and three-dimensional (3D) (Pitarka *et al.*, 1998) soil profiles which are more complex to define.

The “passive seismic” surface wave methods are obtained by measuring and analyzing microtremors or ambient noise. These methods are passive refraction microtremor (ReMi) by Louie (2001), frequency wavenumber (f–k) by Schmidt (1986) and spatially averaged coherency (SPAC) by Asten *et al.* (2003) based on the findings of Aki (1957).

Another theoretical method is the quarter wavelength approach derived by Joyner and Fumal (1985) where the amplification is defined as follows:

$$A\big(f(z)\big) = \sqrt{\frac{\rho_s \beta_s}{\overline{\rho(z)}\bar{\beta}(z)}} \tag{2.19}$$

where $f(z) = 1/[4 \times S_{tt}(z)]$ is the frequency corresponding to depth *z* where $S_{tt}(z)$ is the *S* travel time from the surface to depth *z*. $\rho(z)$ is the density at depth *z*. $\bar{\beta}(z) = z/S_{tt}(z)$ is the average velocity at depth *z*. The subscript *s* represents the corresponding values in the vicinity of the source.

The amplifications obtained from Equation (2.19) are computed for different NEHRP soil classes by Boore and Joyner (1997). Thus, these generic amplification functions can be used whenever NEHRP soil class is known at a site.

There is an alternative empirical method developed by Nakamura (1989) named as Horizontal-to-Vertical ratio (H/V) which can be used when a velocity profile at a site of interest is unknown. The site amplifications are obtained by assuming that the vertical component of ground motion at surface level and bedrock level are identical. The source and path effects can be eliminated by dividing the mean horizontal ground motion amplitude to the vertical one. Similarly, weak ground motions or aftershocks can also be used to get the amplification. (e.g.: Lermo and Chávez-García (1994), Suzuki *et al.* (1995), Huang and Teng (1999), Raghukanth and Somala (2009))

In this study, velocity model for Duzce Region to simulate the low frequency portion of the ground motion is taken from Asten *et al.* (2014) where SPAC and H/V methods are used. On the other hand, for the high frequency portion, amplification from the H/V method is used (Ugurhan and Askan, 2010).

In the high frequency portion of ground motions, there is a rapid decay of the spectral amplitudes. The attenuation during wave propagation does not cause this diminution effect (Boore *et al.*, 1993). This decay is investigated in several studies: Papageorgiou and Aki (1983) state that the decay is due to the source processes; while Hanks (1982) and Atkinson (2004) mention that the near-surface site conditions cause this decay.

There are two filter types to model this spectral decay: f_{max} filter (Hanks, 1982) and the kappa operator. The diminution function $D(f)$ is given as follows:

$$D(f) = \left(1 + \left(\frac{f}{f_{max}}\right)^8\right)^{-0.5} \tag{2.20}$$

where f_{max} is the cut–off frequency.

The second filter type, the kappa parameter (Anderson and Hough, 1984) is defined as an exponential decay to represent the diminution function. To obtain the kappa parameter, first Fourier Amplitude Spectra (FAS) of the records is plotted using a semi–logarithmic scale. Then, a best fit line is drawn to the decaying part of FAS. The kappa parameter is obtained by dividing the best fit line slope to $-\pi$. To eliminate the effects of the path from hypocenter to station, a zero-distance kappa value (κ_0) is used in site effect calculations. To get this κ_0 value, kappa values of the records versus corresponding epicentral distances are plotted. The zero–distance kappa value (κ_0) is computed to be the ordinate of the best fit line. The diminution filter function with κ_0 used in the stochastic modeling is given as:

$$D(f) = e^{-\pi\kappa_0 f} \tag{2.21}$$

2.3.2. Stochastic Finite Fault Modeling

Stochastic point-source modeling gives accurate simulations for stations that are located at distances from the fault larger than fault dimensions (far-field stations). Similarly, it does not work well for large events. The near-field simulations should be done by taking into account the fault dimensions. Stochastic finite-fault simulation method is developed found by Beresnev and Atkinson (1997). In this method, the modeled fault is divided into smaller sub faults where each of them is assumed as a stochastic point-source. To get the time history, each sub fault response is summed up in the time domain. The approach for large event discretization and superposition of sub fault contribution in the discretized space is adapted from Hartzell (1978).

In finite fault modeling, the fault plane is assumed as rectangular and divided into sub faults which are modeled as point-sources with ω^2 spectrum. The rupture propagation is assumed to start radially from the hypocenter with a constant rupture velocity (ν_r), where the center of one sub fault is selected as the hypocenter. In this method, while the rupture reaches the center of a sub fault, other sub faults are triggered. Accordingly, the contributions of all sub faults are summed with a kinematic time delay of each sub fault for obtaining the contribution of the entire fault plane (Atkinson *et al.*, 2009). This summation in the time domain is as follows:

$$a(t) = \sum_{i=1}^{nl} \sum_{j=1}^{nw} a_{ij} \cdot \left(t - \Delta t_{ij} - T_{ij}\right) \tag{2.22}$$

where $a(t)$ is the ground motion acceleration from the entire fault at time t and a_{ij} is the ground motion acceleration obtained from the ij^{th} sub fault modeled as a point-source (Boore, 1983); nl and nw are the number of sub faults along the length and width of the main fault, respectively. The term T_{ij} is the fraction of the rise time of a sub fault where the rise time is defined as the sub fault radius divided by the rupture velocity (Atkinson *et al.*, 2009).The term Δt_{ij} is the time delay for each sub fault which is the summation of the time required for the rupture front to reach the element and the time required for the shear-wave to reach the receiver after the element has been triggered (Beresnev and Atkinson, 1997).

Along the fault plane, it is assumed that slip values are distributed homogeneously. Thus, the seismic moment of each sub fault is represented as follows:

$$M_{0_{ij}} = \frac{M_0}{N} \tag{2.23}$$

where M_0 is the seismic moment and N is the total number of sub faults.

When the sub fault dimensions are not identical, the seismic moment of each sub fault is calculated by taking into account the slip weight of each sub fault (Motazedian and Moinfar, 2006). The seismic moment for this case is given in as:

$$M_{0_{ij}} = \frac{M_0 \cdot S_{ij}}{\sum_{k=1}^{nl} \sum_{l=1}^{nw} S_{kl}} \tag{2.24}$$

where S_{ij} is the relative slip weight of each sub fault.

The acceleration spectrum of each sub fault A_{ij}, is considered as stochastic point–source in early work by Beresnev and Atkinson (1997) as:

$$A_{ij}(f) = \frac{C \cdot M_{0_{ij}} \cdot (2\pi f)^2}{1 + \left(\frac{f}{f_{c_{ij}}}\right)^2} \cdot \left(\frac{1}{R_{ij}}\right) \cdot e^{-\frac{\pi f R_{ij}}{Q\beta}} \cdot D(f) \cdot e^{-\pi\kappa f} \tag{2.25}$$

where $f_{c_{ij}}$ is the static corner frequency of each sub fault which is given as:

$$f_{c_{ij}} = 4.9 \times 10^6 \cdot \beta \cdot \left(\frac{\Delta\sigma}{M_{0_{ij}}}\right)^{\frac{1}{3}} \tag{2.26}$$

This static corner frequency approach was used in the original stochastic finite-fault code FINSIM (Beresnev and Atkinson, 1998). In this method, the acceleration spectrum depends on the size and number of the sub faults. The program is updated and named as EXSIM by Motazedian and Atkinson (2005) who introduced the dynamic corner frequency approach. The dynamic corner frequency changes in inverse proportion with the rupture area while the rupture propagates. The dynamic corner frequency is given as:

$$f_{c_{ij}} = N_R(t)^{-\frac{1}{3}} \, 4.9 \cdot 10^6 \beta \left(\frac{\Delta\sigma}{M_{0_{ave}}} \right)^{\frac{1}{3}} \tag{2.27}$$

where $\mathrm{N_R}(t)$ is the cumulative number of ruptured sub faults at time t and $M_{0_{ave}} = M_0/N$ is the average seismic moment of sub faults.

In the dynamic corner frequency approach, the number of ruptured sub faults changes in proportion as rupture progresses, while the dynamic corner frequency changes in inverse proportion. Thus, the radiated energy at higher frequencies decreases. A frequency–dependent scaling factor H_{ij}, is applied to the spectrum by Motazedian and Atkinson (2005) to counteract the decrease in the radiated energy at higher frequencies. The final acceleration spectrum is then obtained as:

$$A_{ij}(f) = C \cdot M_{0ij} \cdot H_{ij} \cdot \frac{(2\pi f)^2}{\left[1 + \left(\frac{f}{f_{c_{ij}}}\right)^2\right]} \cdot e^{-\frac{\pi f R_{ij}}{Q(f)\beta}} \cdot D(f) \cdot e^{-\pi\kappa f}$$

$$H_{ij} = \left(N \frac{\sum \frac{f^2}{1+\left(\frac{f}{f_c}\right)^2}^2}{\sum \frac{f^2}{1+\left(\frac{f}{f_{c_{ij}}}\right)^2}^2} \right)^{\frac{1}{2}} \tag{2.28}$$

Motazedian and Atkinson (2005) further modified the methodology by defining a concept of pulsing sub fault. The modification is originated from “self–handling model” that belongs to Heaton (1990). Rupture propagates until a percentage of each sub fault is ruptured, which is called as “pulsing area percentage” in EXSIM. The behavior of active (pulsed) cells reduces the dynamic corner frequency until they reach the defined pulsing area percentage; whereas the passive cells have no contribution to this frequency. This pulsing area percentage controls the percentage of the maximum ruptured area. This parameter is a free parameter such as the stress drop and both can change the amplitude of the spectrum.

In this thesis, for simulating high frequencies of the studied earthquake, the stochastic finite–fault methodology with a dynamic corner frequency concept (Motazedian and Atkinson, 2005) is used.

2.4. Deterministic Strong Ground Motion Simulation Methodology

The low frequency simulations are fundamentally modeled by using deterministic Green's function approach (f ≤ 1–3 Hz).

2.4.1. Deterministic Green's Function Modeling

Deterministic Green's function modeling based on the findings of Hartzell (1978) and developments done by Irikura (1986) is used for low frequency portion of the ground motions.

In Hartzell's method, the aftershocks of a large earthquake are used as Green's function to model the strong ground motion of the corresponding large earthquake. The ground motion of the large earthquake $U(t)$ is presented by summing the response of aftershocks $U_i(t)$ which are defined as a point–source:

$$U(t) = \sum_{i=1}^{n} [U_i(t) * Q_i(t)] \cdot H(t - \tau_i) \tag{2.29}$$

$$U_i(t) = S_i(t) * M_i(t) \; * R_i(t) \tag{2.30}$$

where $*$ is used for indicating convolution; $Q_i(t)$ is a generalized scaling factor; n is the number of total point–sources on the fault plane; H is the Heaviside unit step function and τ_i is a phase delay term that affected by both rupture propagation and travel time from source to receiver. In Equation (2.30), $S_i(t)$ is the source function,

$M_i(t)$ is the earth response and $R_i(t)$ is the receiver function which is constant. It is assumed that the focal mechanism of aftershocks is identical to the main event. The phase delay term τ_i, depends on the rupture velocity and direction. To get accurate τ_i values, the rupture initiation point should be known in detail.

Irikura (1986) developed the ground motion equation for a large event by superposing observed records of a small event as follows:

$$U(x,t) = \sum_{i=1}^{l}\sum_{j=1}^{m}\sum_{k=1}^{n}\frac{F_{ij}^{s}}{F_s}\cdot\frac{r_o}{r_{ij}}\cdot u\left(x-t-t_\xi-t_d\right) \tag{2.31}$$

where $U(x,t)$ is the synthetic motion for large event, u is the observed record for a small event, F_{ij}^{s} and r_{ij} are the radiation pattern and focal distance for (i,j) element, l, m and n are the parameters that determined from the scaling relations (Kanamori and Anderson, 1975). The phase term, t_ξ is expressed in as:

$$t_\xi = \frac{r}{v_s} + \frac{\xi_{ij}}{v_r} \tag{2.32}$$

where v_r and v_s are the rupture and S–wave velocities, ξ_{ij} is a distance parameter from the point where rupture starts to $(i,j)^{th}$ element and r is the distance between large event and a receiver.

In addition, t_d is the uniform time shift given as follows:

$$t_d = (k-1)\cdot\frac{\tau}{n} \tag{2.33}$$

where τ is the rise time of the large event and n is the parameter that determined from the scaling relations (Kanamori and Anderson, 1975) for (k) element.

Irikura (1986) stated that Equation (2.31) has some problems. Revisions are done in terms of periodicity, time shifts and assuming the parameters l, m and n of Equation (2.33) are all equal to N:

$$U(R,t) = \sum_{n=1}^{N\times N} \left(\frac{R_0}{R_n}\right) \cdot F\left(t - \frac{\xi_n}{v_r} - \frac{R_n}{v_s}\right) \cdot u(R_0, t) \tag{2.34}$$

Where R, R_0, and R_n are the large event to receiver distance, the small event to receiver distance and distance from n^{th} sub fault to the receiver, respectively. The fault plane is divided into sub faults as $N \times N$. $F(t)$ is the function which corrects the slip velocity difference between the target and small event. The term ξ_n is another distance parameter from the point where rupture starts to n^{th} sub fault. Finally, v_r and v_s are the rupture and S–wave velocities, respectively.

The function $F(t)$ is expressed by a delta function $\delta(t)$, and a boxcar function $b_T(t)$, and amplitude D as follows:

$$F(t) = \delta(t) + D \cdot b_r(t) \tag{2.35}$$

2.4.1.1. Discrete Wavenumber Finite Element Method (DWFE)

The method used to compute Green's function in this thesis is discrete wavenumber finite element method (DWFE) (Olson *et al.*, 1984; Spudich and Archuleta, 1987) which models the Earth in one-dimension. This approach is implemented in the COMPSYN program (Spudich and Xu, 2003).

In the DWFE method, separable solutions of elastic equations for the horizontal dependence of the seismic wavefield with the finite element method and the finite differences numerical solutions for the vertical and time dependence are combined. Olson *et al.* (1984) derived the Fourier-Bessel series representation of the elastic displacement field due to the point force vectors and point-couple force systems. The expression for the displacement is given as:

$$\boldsymbol{u}(r,\phi,z,t) = \sum_m \int_0^\infty \frac{k}{2\pi}\left[U_{zk}^m(z,t)\boldsymbol{R}_k^m(r,\phi) + U_{rk}^m(z,t)\boldsymbol{S}_k^m(r,\phi) + U_{\phi k}^m(z,t)\boldsymbol{T}_k^m(r,\phi)\right]dk \tag{2.36}$$

where the vertical derivative is:

$$\boldsymbol{u}'(r,\phi,z,t) = \sum_m \int_0^\infty \frac{k}{2\pi}\left[{U'}_{zk}^m(z,t)\boldsymbol{R}_k^m(r,\phi) + {U'}_{rk}^m(z,t)\boldsymbol{S}_k^m(r,\phi) + {U'}_{\phi k}^m(z,t)\boldsymbol{T}_k^m(r,\phi)\right]dk \tag{2.37}$$

where $\boldsymbol{R}_k^m$, $\boldsymbol{S}_k^m$ and $\boldsymbol{T}_k^m$ are the surface vector harmonics (Olson *et al.*, 1984), r, ϕ and z are the radial, azimuthal and vertical cylindrical coordinates in the far–field, k is the horizontal wavenumber that enters into argument of m order Bessel function $J_m(kr)$, where m is the integer angular frequency. The expansion coefficients $U_{zk}^m(z,t)$, ${U'}_{zk}^m(z,t)$, $U_{rk}^m(z,t)$, ${U'}_{rk}^m(z,t)$, $U_{\phi k}^m(z,t)$ and ${U'}_{\phi k}^m(z,t)$ are derived by a time stepping finite element method.

The definitions of the surface vector harmonics are given as follows:

$$\begin{aligned}
\boldsymbol{R}_k^m(r,\phi) &= \boldsymbol{Y}_k^m(r,\phi)e_z \\
\boldsymbol{S}_k^m(r,\phi) &= \frac{1}{k}\partial_r \boldsymbol{Y}_k^m(r,\phi)e_r + \frac{1}{kr}\partial_\phi \boldsymbol{Y}_k^m(r,\phi)e_\phi \\
\boldsymbol{T}_k^m(r,\phi) &= \frac{1}{kr}\partial_\phi \boldsymbol{Y}_k^m(r,\phi)e_r - \frac{1}{k}\partial_r \boldsymbol{Y}_k^m(r,\phi)e_\phi
\end{aligned} \tag{2.38}$$

where $\boldsymbol{Y}_k^m(r,\phi) = J_m(kr)e^{im\phi}\ for\ m = 0, \pm 1, \pm 2, \ldots$

To verify the definition of the (r,ϕ) dependence of the separable solution to the equation of motion by surface vector harmonics, a body force density vector $\boldsymbol{f}$ and displacement vector $\boldsymbol{u}$ are defined by Olson *et al.* (1984) and given in Equation (2.39).

The (r, ϕ) dependence of these vectors is expressed by the identical surface harmonics as follows:

$$\begin{aligned} \boldsymbol{f}(r,\phi,z,t) &= F_{zk}^{m}(z,t)\boldsymbol{R}_k^m(r,\phi) + F_{rk}^{m}(z,t)\boldsymbol{S}_k^m(r,\phi) \\ &\quad + F_{\phi k}^{m}(z,t)\boldsymbol{T}_k^m(r,\phi) \\ \boldsymbol{u}(r,\phi,z,t) &= U_{zk}^{m}(z,t)\boldsymbol{R}_k^m(r,\phi) + U_{rk}^{m}(z,t)\boldsymbol{S}_k^m(r,\phi) \\ &\quad + U_{\phi k}^{m}(z,t)\boldsymbol{T}_k^m(r,\phi) \end{aligned} \tag{2.39}$$

The other dependence (z, ϕ) is described by the complex scalar coefficients which are given also in Equation (2.39): F_{zk}^m, F_{rk}^m, $F_{\phi k}^m$, U_{zk}^m, U_{rk}^m and $U_{\phi k}^m$.

Olson *et al.* (1984) also expressed a discrete wavenumber expansion for the impulse response of the elastic medium which is the solution of the equation of motion (wave equation) given as follows:

$$(\lambda+\mu)\nabla(\nabla\cdot\boldsymbol{u}) + \mu\nabla^2\boldsymbol{u} + \nabla\lambda(\nabla\cdot\boldsymbol{u}) + 2(\nabla\mu)\cdot\boldsymbol{E} + \boldsymbol{f} = \rho\partial_{tt}\boldsymbol{u} \tag{2.40}$$

where λ and μ are the Lamé parameters, $\boldsymbol{u}$ is the displacement field, **E** is Cauchy's infinitesimal strain tensor, **f** is the force density vector and ρ is the material density. E is expressed as:

$$\boldsymbol{E} = \frac{1}{2}[\nabla\boldsymbol{u} + (\nabla\boldsymbol{u})^T] \tag{2.41}$$

In addition, the terms $\nabla\mu$ and $\nabla\lambda$ involved in Equation (2.40) are zero in a homogeneous medium and the equation of motion becomes simpler.

The total motion of the half-space due to the horizontal point load at z_0 is given in as follows:

$$\boldsymbol{u}_z^1(r,\phi,z,t;z_0) = \sum_{n=0}^{\infty} W_n^1 U_{zk_n}^1(z,t;z_0) J_1(k_n r)\cos(\phi) \tag{2.42}$$

$$\boldsymbol{u_r^1}(r,\phi,z,t;z_0) = \sum_{n=0}^{\infty} W_n^1 \left[U_{rk_n}^1(z,t;z_0) \left(\frac{1}{k_n r} J_1(k_n r) - J_2(k_n r) \right) \right.$$
$$\left. + U_{\phi k_n}^1(z,t;z_0) \frac{1}{k_n r} J_1(k_n r) \right] \cos(\phi)$$

$$\boldsymbol{u_\phi^1}(r,\phi,z,t;z_0) = -\sum_{n=0}^{\infty} W_n^1 \left[U_{\phi k_n}^1(z,t;z_0) \left(\frac{1}{k_n r} J_1(k_n r) - J_2(k_n r) \right) \right.$$
$$\left. + U_{rk_n}^1(z,t;z_0) \frac{1}{k_n r} J_1(k_n r) \right] \cos(\phi)$$

$$W_n^1 = \frac{1}{\pi [R J_0(k_n R)]^2}$$

where $J_0(k_n r)$, $J_1(k_n r)$ and $J_2(k_n r)$ are Bessel functions over the interval $0 \leq r \leq R$.

2.4.2. Model Parameters

In this thesis, for low frequency simulations, the open-source code COMPSYN program which works with a discrete wavenumber finite element method (DWFE) is used. The numerical techniques used in COMPSYN program belong to Spudich and Archuleta (1987).

2.4.2.1. The Fault Information

To calculate Green's function in the frequency domain, the fault surface with the stations studied on should be well–known. In the fault geometry, the parameters are the dip of fault, the strike of fault, and the strike (x_1 and x_2) and downdip (z_1 and z_2) coordinates as shown in Figure 2.3 where the red line illustrates the fault plane.

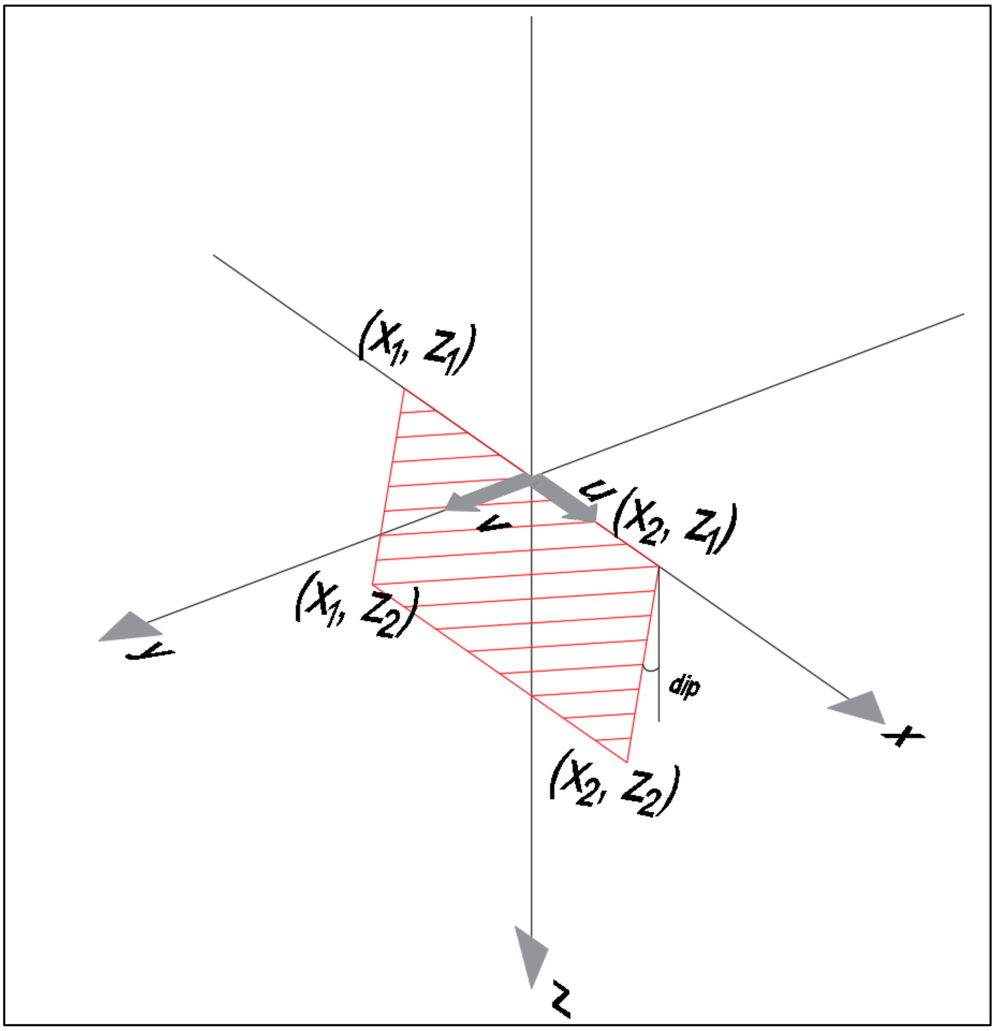

Figure 2.3. Fault geometry definition

2.4.2.2. The Earthquake Slip Distribution

Slip is the relative displacement between two points: On sub fault centers and on earthquake hypocenter. In the slip distribution calculations, the slip velocity time-function form is the same at all points of fault. This can be a decaying exponential function, a boxcar function or another suitable functional form. The function characteristics are duration and amplitude of slip velocity function, and the slip initiating time.

2.4.2.3. The Earth-Velocity Structure

In COMPSYN program, the earth-velocity structure is constructed as one-dimensional in depth where the free surface is assumed at where the depth is zero.

The required parameters to construct the earth–velocity structure for solving Green's function are the depth of the earthquake, P-wave (V_p), and S-wave (V_s) velocities and density values at each depth interval. Depending on the detail of Earth-velocity structure, the accuracy of deterministic Green's function modeling does vary.

CHAPTER 3

BROADBAND GROUND MOTION SIMULATION OF THE 12 NOVEMBER 1999 DUZCE EARTHQUAKE

3.1. Introduction

One of the main insufficiencies for alternative ground motion simulation methods is modeling in a limited frequency range. From an engineering point of view, the necessary frequencies are generally between 0.10 Hz $\leq$ f $\leq$ 10 Hz. Due to this reason, a hybrid ground motion simulation framework is presented to obtain broadband ground motion time histories of past and potential events in Duzce (Turkey) region in this study. As explained in Chapter 2, the broadband ground motion simulations are the combination of deterministic and stochastic methods which covers a wide frequency range.

In Section 3.2, background information on the study area and 12 November 1999 Duzce earthquake is given. Strong ground motion database of the studied earthquake is mentioned in Section 3.3. The parameters used both in deterministic and stochastic solutions are presented in Section 3.4. Finally, in Section 3.5 the results of broadband ground motion simulations and related discussions are presented.

3.2. Background Information

The study area is selected as the Duzce region (Turkey) which is located on the North Anatolian Fault Zone (NAFZ).

In the recent past, two destructive earthquakes occurred in Duzce Region. The first earthquake was on August 17, 1999, Kocaeli with moment magnitude $M_w =$ 7.4 (Earthquake Research Department of the General Directorate of Disaster Affairs, Turkey ERD).The second earthquake that is studied was on November 12, 1999, with moment magnitude $M_w = 7.1$ (Kandilli Observatory and Earthquake Research Institute of Bogazici University (KOERI)). In Figure 3.1, the major earthquakes on the NAFZ during the last century are shown.

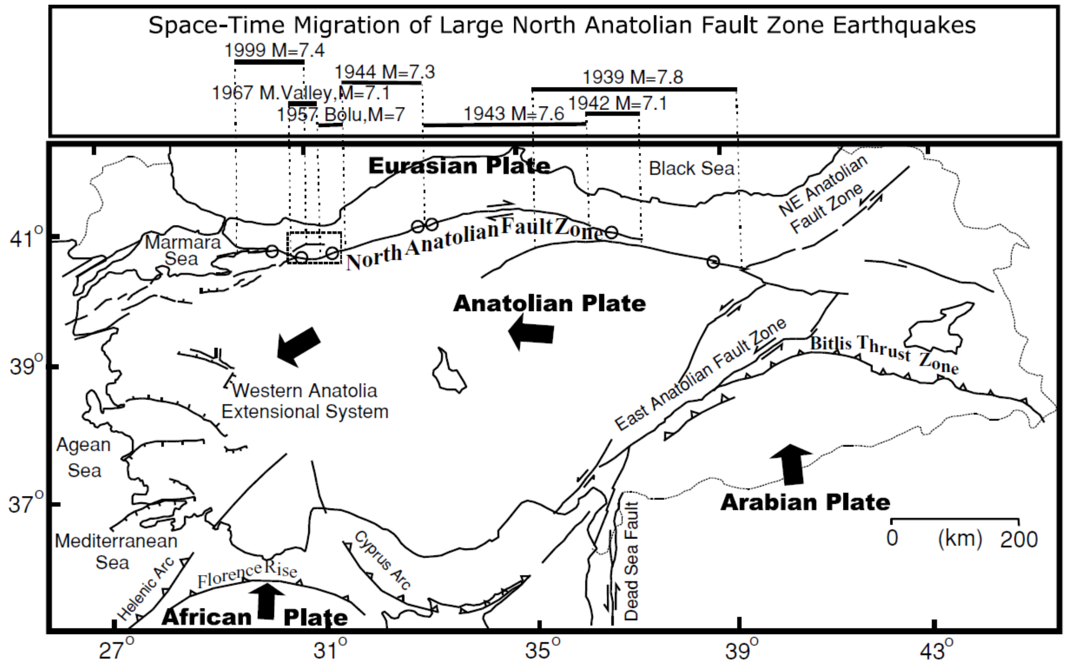

Figure 3.1. Tectonic Map of Turkey and major earthquakes on the NAFZ in the last century (adapted from Akyuz et al., 2002) where the red box shows the study area

The epicentral coordinates of 12 November 1999 Duzce earthquake are 40.82°N & 31.20°E (ERD). The fault orientation, dimensions, coordinates are presented in Table 3.1.

3.3. Strong Ground Motion Database

There are 32 strong-motion stations that recorded the 12 November 1999 Duzce earthquake. These stations belong to ERD, KOERI and Istanbul Technical University (ITU).

Out of 32 strong-motion stations most of them are far field stations where detailed velocity models were not available. Thus, in this study, only four near field stations are selected for ground motion modeling. Figure 3.2 shows the stations with black triangles and the epicenter of the earthquake with a black star.

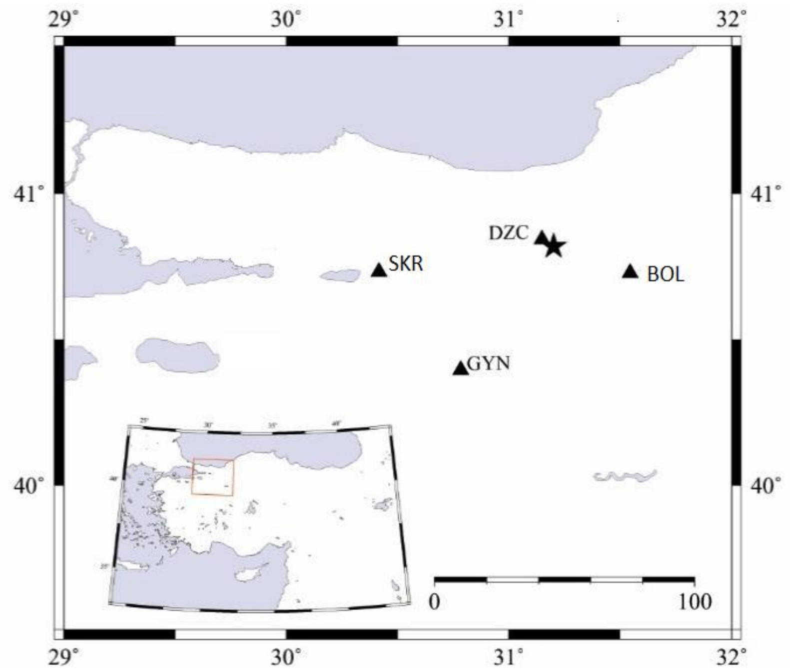

Figure 3.2. Map showing the epicenter of the 1999 Duzce earthquake with the locations of the stations

Table 3.1. *Broadband simulation model parameters for 12 November 1999 Duzce earthquake*

Moment Magnitude		7.1	
Fault Orientation		Strike: 264° Dip: 64°	
Fault Dimensions		North Anatolian Fault (NAF) - 65 km × 25 km	
East end Coordinate of the Fault		40.93°N - 31.49°E	
West end Coordinate of the Fault		40.71°N - 30.91°E	
Epicenter		40.82°N - 31.20°E	
Specific Parameters of Deterministic Ground Motion Simulations		**Specific Parameters of Stochastic Ground Motion Simulations**	
Soil Profiles at 4 Stations BOL, DZC, GYN and SKR	Asten et. al. (2014)	**Stress Drop**	100 bars
		Pulsing Area Percentage	30%
Subfault Dimensions	5 km × 5 km	**Duration Model**	$T = T_0 + 0.05$
Crustal Shear Wave Velocity (β)	3700 m/s	**Quality Factor**	$Q = 88f^{0.9}$
Rupture Velocity	0.8 β	**Geometrical Spreading**	R^{-1} $R \leq 30$km $R^{-0.4}$ $30 < R \leq 60$km $R^{-0.6}$ $60 < R \leq 90$km $R^{-0.8}$ $90 < R \leq 100$km $R^{-0.5}$ $R > 30$km
Crustal Density	2800 kg/m³	**Windowing Function**	Saragoni - Hart
		Kappa Factor	Regional Kappa Model (0.047)
Slip Distribution	Yagi and Kikuchi (2000)	**Site Amplification Factors**	H/V ratios and NEHRP D Amp. F. (Boore and Joyner, 1997)

Table 3.2. *The 1999 Duzce earthquake recorded strong ground motion station information*

Station Name	Code	Latitude °N	Longitude °E	Site Class	R_{EPI} (km)	R_{JB} (km)	PGA EW (cm/s²)	PGA NS (cm/s²)	PGV EW (cm/s)	PGV NS (cm/s)
Bolu	BOL	40.7457	31.6073	D	39.03	11.31	805.88	739.51	66.61	57.78
Düzce	DZC	40.8436	31.1489	D	9.31	0.14	513.78	407.69	90.78	66.47
Göynük	GYN	40.3966	30.7831	D	55.16	38.46	24.82	27.89	8.68	9.84
Sakarya	SKR	40.7371	30.3801	C	64.52	29.03	24.72	17.33	5.17	4.81

3.4. Selection of Model Parameters

For an accurate broadband ground motion simulation; source, path and site parameters must be known in detail. The model parameters for the 1999 Duzce earthquake for broadband simulation are given in Table 3.1. These parameters are respectively explained in detail in Section 3.4.1 and Section 3.4.2 for deterministic and stochastic solutions separately.

3.4.1. Parameters for Deterministic Modeling

The open source code used to model deterministic simulations is COMPSYN program for which the fault parameters (location and rupture area), earthquake slip distribution parameters (rise time, rupture propagation, velocity, etc.), earth-velocity structure parameters (V_p, V_s, density), and seismic moment are required.

3.4.1.1. Fault Parameters

The outputs of the earth-velocity structure model in COMPSYN program are Green's functions in frequency, wavenumber, and depth domain. COMPSYN program employs detailed source parameters including the hypocenter, fault mechanism, seismic moment, and slip model on the fault plane as main inputs.

3.4.1.2. Earthquake Slip Distribution Parameters

The slip distribution is adapted from Umutlu et al. (2004) as explained in Section 3.4.2.1. The slip velocity type is selected as a boxcar function. Ground motion spectrum and slip spectra are obtained as the main outputs.

3.4.1.3. Earth Velocity Structure Parameters

In Duzce Region, the earth-velocity structure is poorly known. Various velocity models in 1D are compared which have been developed by Bulut *et al.* (2007) for Izmit Region; Bouin *et al.* (2004), Umutlu *et al.* (2004), Konca *et al.* (2010) for Duzce Region; and Asten *et al.* (2014) for both Bolu and Duzce Region.

In this study, the velocity model by Asten *et al.* (2014) is used. In this velocity model, the surface shear-wave velocity for Duzce Region is 100 m/s, and for Bolu Region is 155 m/s. P-wave velocity (V_p), S-wave velocity (V_s) and densities (ρ) with respect to depths are given in Table 3.3 and Table 3.4, respectively. In Figure 3.3, velocity profiles used in the model are illustrated. The earth-velocity structure has been modified for the code used in the application COMPSYN program.

Table 3.3. *1D velocity model for Duzce region in simulations*

Layer	Depth (km)	V_p (km/sec)	V_s (km/sec)	ρ (g/cm³)
1	0.002	0.40	0.10	1.78
2	0.006	0.40	0.20	1.80
3	0.014	1.50	0.24	2.00
4	0.046	2.00	0.40	2.14
5	0.096	2.00	0.60	2.14
6	0.136	2.00	0.65	2.14
7	0.336	2.94	1.00	2.39
8	0.736	2.94	1.15	2.39
9	2.036	2.94	1.30	2.39
10	10	3.03	1.38	2.42
11	30	3.25	1.57	2.51
12	50	3.45	1.77	2.59
13	∞	4.00	2.25	2.80

Table 3.4. *1D velocity model for Bolu region in simulations*

Layer	Depth (km)	V_p (km/sec)	V_s (km/sec)	ρ (g/cm³)
1	0.00075	0.80	0.16	1.78
2	0.003	0.60	0.16	2.00
3	0.005	1.50	0.19	2.00
4	0.013	1.50	0.22	2.00
5	0.045	2.00	0.39	2.14
6	0.109	2.00	0.50	2.14
7	0.209	2.00	0.60	2.14
8	0.409	2.94	1.05	2.39
9	0.609	2.94	1.05	2.39
10	2.209	2.94	1.20	2.39
11	10	3.11	1.32	2.45
12	30	3.56	1.62	2.55
13	50	4.00	1.92	2.70
14	∞	4.50	2.25	2.80

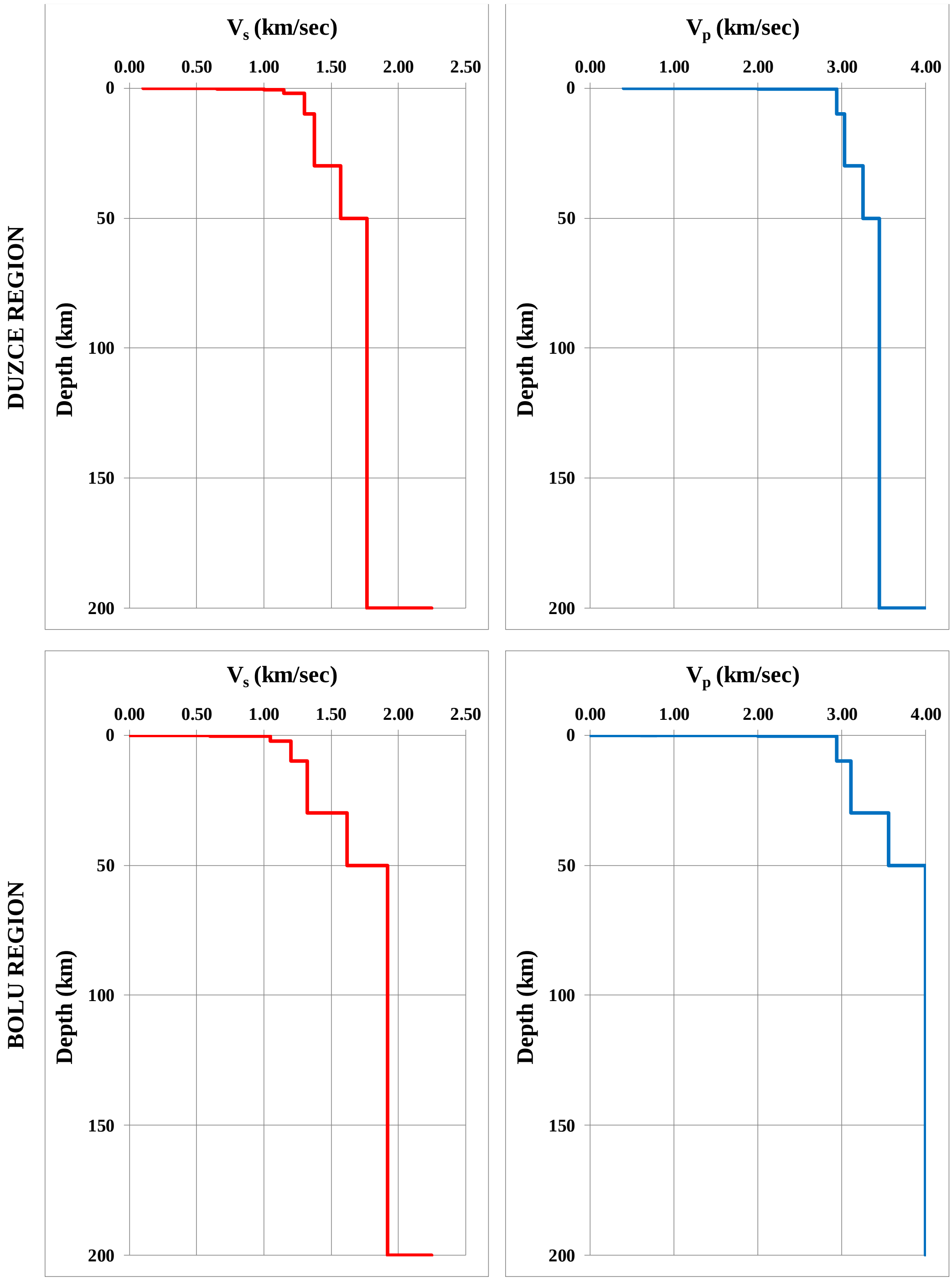

Figure 3.3. 1D velocity models for the Duzce and Bolu Region used in simulations

3.4.1. Parameters for Stochastic Finite-Fault Modeling

The simulation parameters for stochastic finite–fault modeling are adapted from Ugurhan and Askan (2010) while some modifications suggested by Karimzadeh et al. (2017a) are applied. For the high frequency portion of the ground motion simulations, EXSIM program is used (Motazedian and Atkinson, 2005).

3.4.1.1. Source Parameters

The source parameters required are the orientations of the fault (dip and strike angles), the fault dimensions, depth and coordinates of hypocenter, slip distribution along the fault plane, stress drop and pulsing area percentage.

As mentioned, the orientations of the fault, the fault dimensions, depth and coordinates of hypocenter are given in Table 3.1. The slip distribution is adapted from the study of Umutlu *et al.* (2004), where the single and multiple fault plane models obtained from geodetic, teleseismic and strong–motion data are used (The most accurate stress drop and pulsing area percentage are selected from parameters listed in Ugurhan and Askan (2010)). The sub fault dimensions are selected as 5 × 5 km along the strike and dip directions.

3.4.1.1. Path Parameters

The path parameters represent geometric spreading, anelastic attenuation and distance-dependent duration model. The geometric spreading model is adapted from Ansal *et al.* (2009) for Marmara Region. The model is given as follows:

$$\begin{array}{ll} R^{-1} & R \leq 30\ km \\ R^{-0.4} & 30 < R \leq 60\ km \\ R^{-0.6} & 60 < R \leq 90\ km \\ R^{-0.8} & 90 < R \leq 100\ km \\ R^{-0.5} & R > 100\ km \end{array} \tag{3.1}$$

where Q is the quality factor model belongs to Boore (1984) and is given as follows:

$$Q(f) = 88 \cdot f^{0.9} \tag{3.2}$$

The distance-dependent duration model is adapted from Hermann as follows:

$$T = T_0 + 0.05 \tag{3.3}$$

where T_0 is the source duration.

3.4.1.2. Site Parameters

For the high frequencies, H/V technique is used to get the site amplification factors. In Ugurhan and Askan (2010), aftershock and mainshock records are used to obtain H/V ratios from all available records of the 1999 Duzce earthquake. In H/V method, the vertical components of the seismic waves are assumed to be not exposed to local soil amplification which the horizontal components experience. The average H/V ratios are adopted from the study of Ugurhan and Askan (2010). The H/V ratios of the studied stations are given in Figure 3.4.

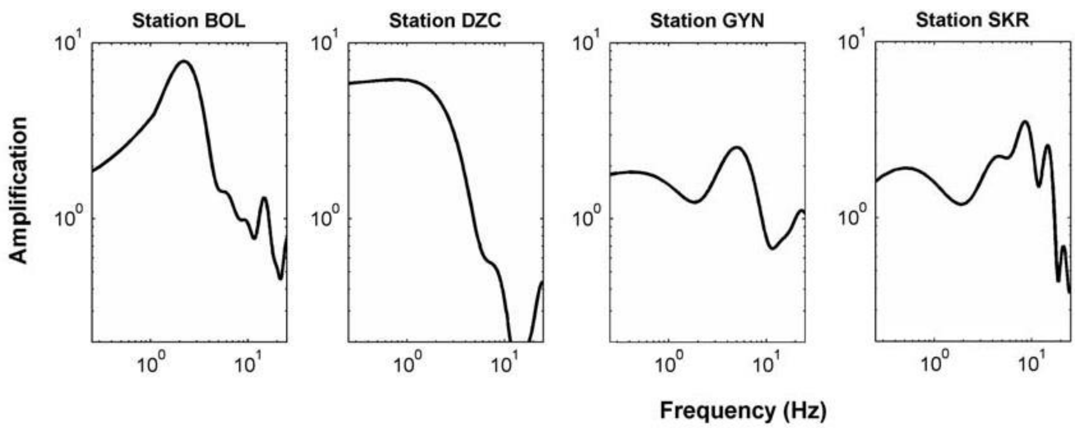

Figure 3.4. The average H/V ratios of the studied stations based on mainshock and aftershock recordings from the 1999 Duzce earthquake (Ugurhan and Askan, 2010)

3.5. Results of Simulations and Discussions

The results and discussions are given for the stations separately. Summary of results and discussions is given in Chapter 5.

3.5.1. Comparison of Observed and Simulated Data

The comparisons are made between deterministic approach results, stochastic method results, broadband result and real records. As mentioned in previously, four stations have been examined in the study: BOL, DZC, GYN and SKR stations. The comparisons of results are illustrated in terms of Fourier Amplitude Spectrum (FAS), Response Spectrum (RS), PGA and PGV values. The details are given in the following sections.

3.5.1.1. Validation of Results

In order to find the misfit between observed and simulated data, a misfit function is used in the frequency domain (Karimzadeh *et al.*, 2017a) as follows:

$$Misfit_{FAS} = \frac{1}{n_f} \cdot \sum_f \left| log(\frac{FAS_{syn}(f)}{FAS_{obs}(f)} \right| \tag{3.4}$$

where n_f is the number of discrete frequencies, $FAS_{syn}(f)$ and $FAS_{obs}(f)$ are the synthetic and observed Fourier amplitudes at frequency f, respectively.

Another misfit is quantified between observed and simulated data in terms of response spectra as follows:

$$Misfit_{RS} = \frac{1}{n_T} \cdot \sum_T \left| log(\frac{RS_{syn}(T)}{RS_{obs}(T)} \right| \tag{3.5}$$

where n_T is the number of discrete periods, $RS_{syn}(f)$ and $RS_{obs}(f)$ are the synthetic and observed response spectral amplitudes at period T, respectively.

Additional types of misfits are defined in terms of PGA and PGV follows (Karimzadeh *et al.*, 2017a):

$$Misfit_{PGA} = \left| \frac{PGA_{syn}}{PGA_{real}} \right| - 1 \tag{3.6}$$

$$Misfit_{PGV} = \left|\frac{PGV_{syn}}{PGV_{real}}\right| - 1 \quad (3.7)$$

where PGA_{syn} and PGA_{real} are the simulated and real PGA, and PGV_{syn} and PGV_{real} are the simulated and real PGV, respectively.

3.5.1.2. Station DZC

Station DZC is placed in the city of Duzce and it is the nearest station to the epicenter of the 1999 Duzce earthquake. The coordinates of the station are 40.84364 N°-31.14888 E°.

The station is located at 0.14 km R_{JB} distance from the hypocenter of the 1999 Duzce earthquake which causes unrealistic results by the deterministic approach (Spudich and Xu, 2003). In other words, COMPSYN program has a significant limitation to calculate static displacements very close to a fault which ruptures the surface of Earth (Spudich and Xu, 2003). Hence, the results of the stochastic method are used instead of broadband simulation results. The results reveal at station DZC that estimated PGA from the stochastic method matches closely to the PGA observed in N-S direction.

The acceleration-time history comparisons are given in Figure 3.5. The simulated PGA value is 333.32 cm/s², whereas the observed peak ground acceleration in E-W direction is 513.78 cm/s² and N-S direction is 407.69 cm/s². The simulated results are in good match with the observed data.

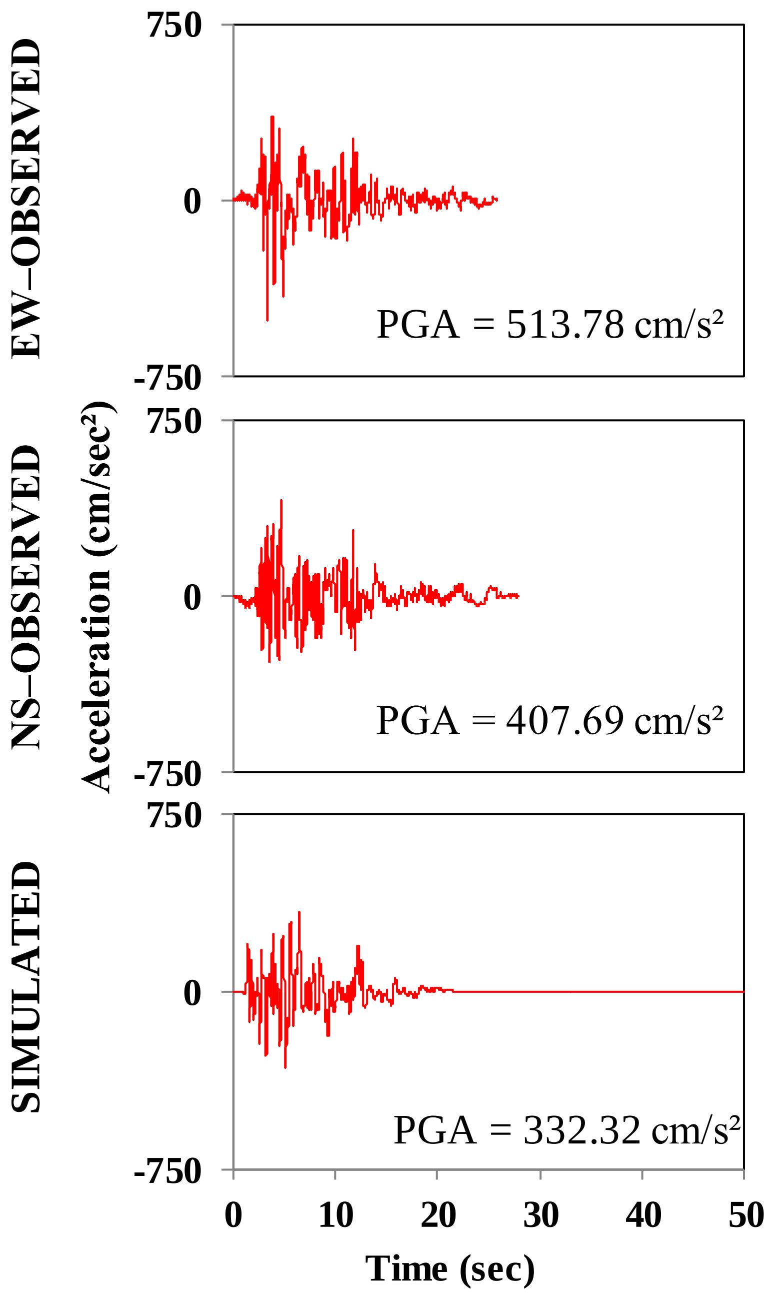

Figure 3.5. Comparison of acceleration-time histories of stochastic method results with real data for the 12 November 1999 Duzce earthquake in E-W and N-S direction – station DZC

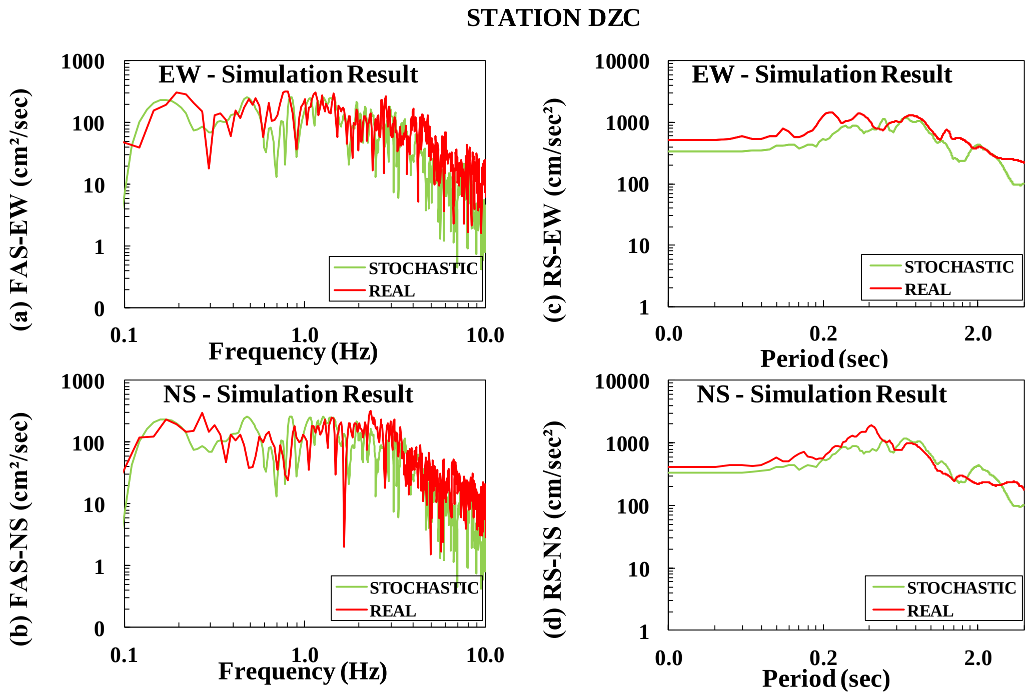

Figure 3.6. Comparison of real and simulated FAS [(a),(b)] and RS with 5% damping [(c),(d)] at station DZC for E-W and N-S components for the 12 November 1999 Duzce earthquake

FAS and RS amplitudes give a close match for the frequency range of $0 < f < 10\ Hz$ (Figure 3.6). FAS and RS misfits for station DZC are given both for stochastic method simulations in Table 3.5 and Table 3.6, respectively. Due to use of only stochastic method results at this station, there is no matching frequency in the corresponding tables.

The misfits are better for N-S direction. FAS misfits are calculated as 0.4205 for E-W component and 0.3844 for N-S component. In addition, the simulations match well with the real records in both directions. RS misfits are calculated as 0.1768 for E-W component and 0.1721 for N-S component where the results are satisfactory as FAS misfits. Misfits for PGA and PGV are given in Table 3.7.

Table 3.5. *FAS misfits of real records and simulation results for E-W and N-S components – station DZC*

Station DZC	Broadband Simulation Misfit			Stochastic Method Misfit
Directions	Matching f	0 Hz - f	f - 10 Hz	0 - 10 Hz
(E-W)	-	0.4205		0.4205
(N-S)	-	0.3844		0.3844

Table 3.6. *RS misfits of real records and simulation results for E-W and N-S components – station DZC*

Station DZC	Broadband Simulation Misfit	Stochastic Method Misfit
Directions	0 - 4 sec	0 - 4 sec
(E-W)	0.1768	0.1768
(N-S)	0.1721	0.1721

Table 3.7 *PGA and PGV misfits of real records and simulation results for E-W and N-S components – station DZC*

Station DZC / Directions	$Misfit_{PGA}$	$Misfit_{PGV}$
(E-W)	-0.35	-0.22
(N-S)	-0.18	0.06

3.5.1.3. Station BOL

Station BOL is placed in the city of Bolu (Turkey). The coordinates of the station are 40.74567 N°-31.60732 E°.

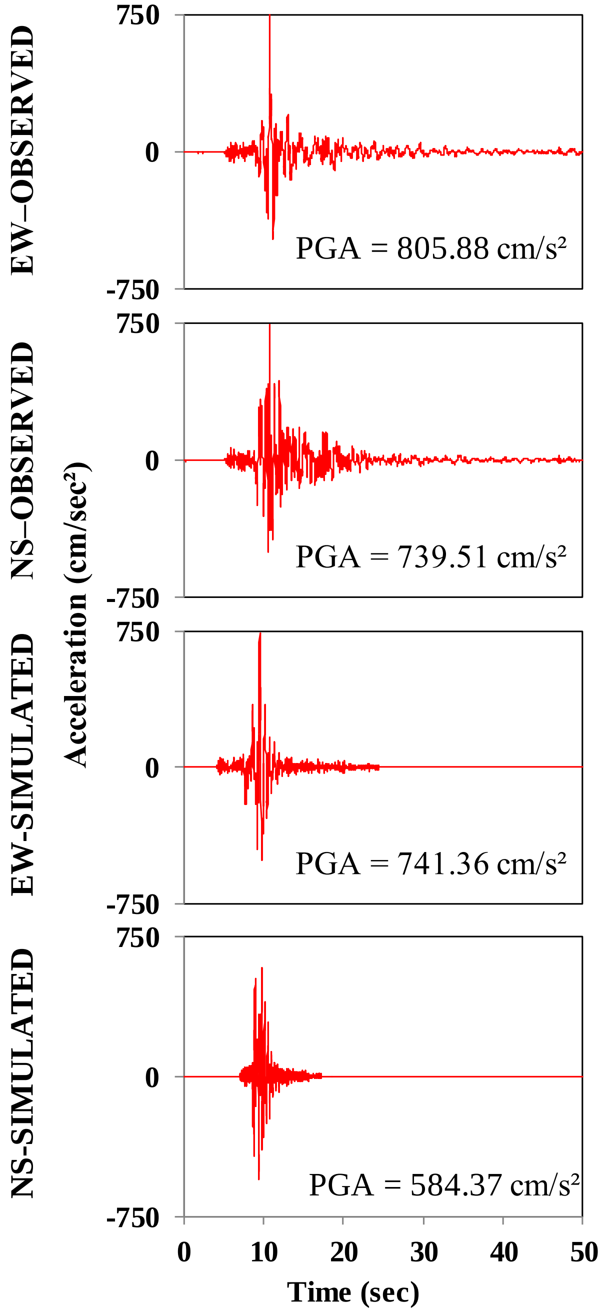

Figure 3.7. Comparison of acceleration-time histories of broadband results with real data for the 12 November 1999 Duzce earthquake in E-W and N-S direction – station BOL

The acceleration-time history comparison for station BOL is given in Figure 3.7. The simulated PGA value in E-W direction is 741.36 cm/s² and in N-S direction is 584.37 cm/s², whereas PGA values recorded by station BOL for the 1999 Duzce earthquake, in E-W direction is 805.88 cm/s² and N-S direction is 739.51 cm/s². Simulated record in N-S direction slightly underestimates the PGA value whereas PGV value in same direction is overestimated.

In Figure 3.8, Comparison of Fourier Amplitude Spectra and the Response Spectra (with 5% damping ratio) of simulation results with real data for the 12 November 1999 Duzce earthquake at station BOL is given. When the result at BOL station is studied visually, it is observed that BOL provide closer values to the observed FAS compared to stochastic method results (Table 3.8).

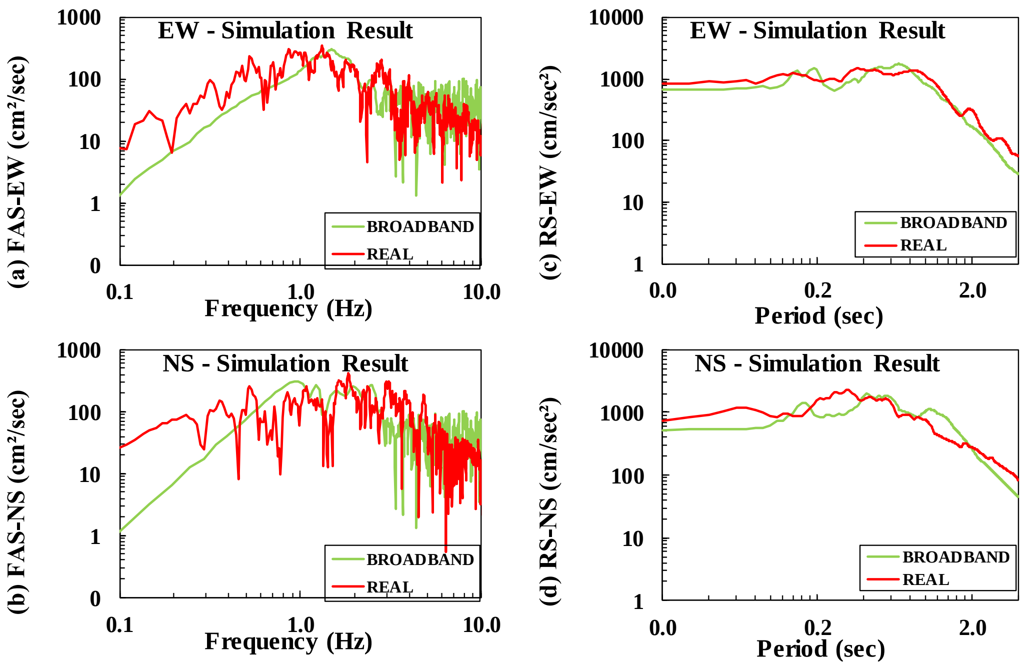

Figure 3.8. Comparison of real and simulated FAS [(a),(b)] and RS with 5% damping [(c),(d)] at station BOL for E-W and N-S components for the 12 November 1999 Duzce earthquake

According to the broadband results, both directions (E-W and N-S) give accurate results compared to stochastic method results. The misfits for broadband simulation and for stochastic method are given numerically in Table 3.8 and Table 3.9 in terms of FAS and RS (with 5% damping ratio) misfits, respectively. The matching frequency for E-W direction is 2.661 Hz and for N-S direction is 2.930 Hz where the deterministic solutions are done up to 3 Hz. The results from deterministic approach ($0 < f < 2.661\ Hz$) are better in E-W direction. FAS misfit is calculated as 0.3122 in E-W direction and 0.3668 in N-S direction. Similarly, for the interval of matching frequency and 10 Hz in E-W direction, the FAS misfit is calculated as 0.3705 and the results are better than in N-S direction. The RS misfits are 0.1619 for E-W component and 0.1841 for N-S component. It is obvious that both FAS and RS misfits for broadband simulation results are satisfactory.

Table 3.8. *FAS misfits of real records and simulation results for E-W and N-S components – station BOL*

Station BOL	Broadband Simulation Misfit			Stochastic Method Misfit
Directions	Matching f	0 Hz - f	f - 10 Hz	0 - 10 Hz
(E-W)	2.661 Hz	0.3122	0.3705	0.4494
(N-S)	2.930 Hz	0.3668	0.4077	0.4949

Table 3.9. *RS misfits of real records and simulation results for E-W and N-S components – station BOL*

Station BOL	Broadband Simulation Misfit	Stochastic Method Misfit
Directions	0 - 4 sec	0 - 4 sec
(E-W)	0.1619	0.5630
(N-S)	0.1841	0.6251

Misfits for PGA and PGV are given in Table 3.10. The PGA and PGV misfits for E-W direction are same, -0.08 which means that an overall close match is obtained between the real records and broadband simulation results for the frequency range between 0 and 10 Hz.

Table 3.10. *PGA and PGV misfits of real records and simulation results for E-W and N-S components – station BOL*

Station BOL / Directions	$Misfit_{PGA}$	$Misfit_{PGV}$
(E-W)	-0.08	-0.08
(N-S)	-0.21	0.28

In brief, it is observed that results of broadband ground motion simulation for BOL station reduces misfits compared to using the stochastic method.

3.5.1.4. Station GYN

Station GYN is placed in the city of Bolu. The coordinates are 40.39659 N°-30.78307 E°.

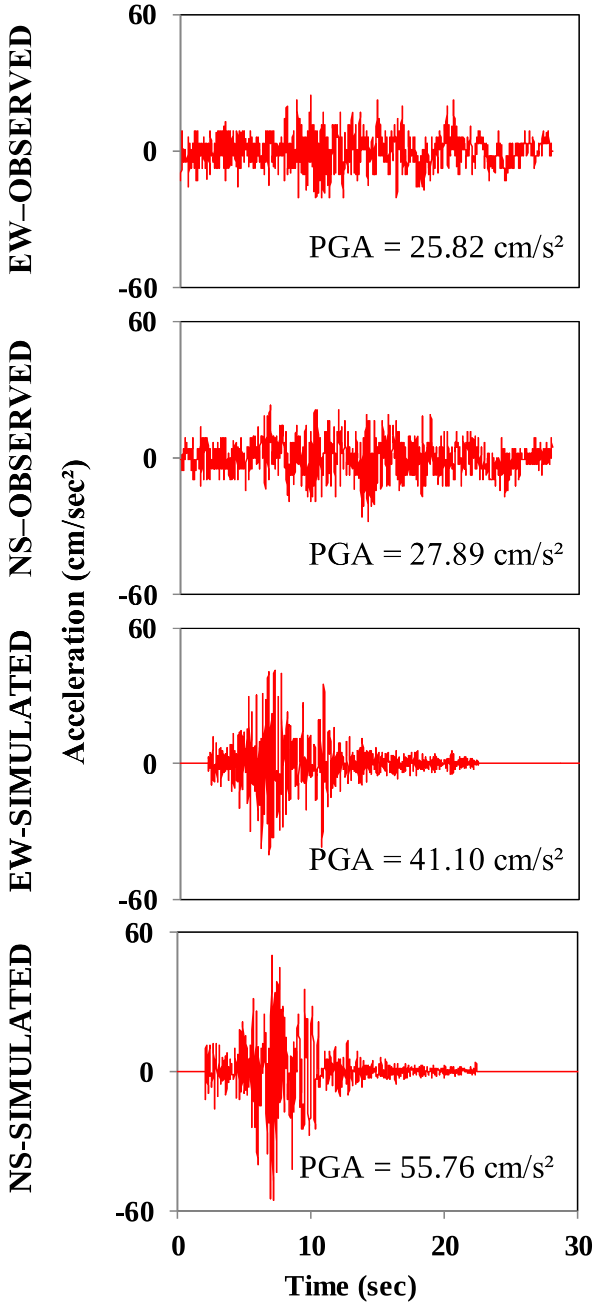

Figure 3.9. Comparison of acceleration-time histories of broadband results with real data for the 12 November 1999 Duzce earthquake in E-W and N-S direction – station GYN

The acceleration-time history comparison with PGA values for station GYN is given in Figure 3.9 in order for observed ground motion in E-W direction, observed ground motion in N-S direction and simulated ground motion by the deterministic method in E-W direction and in N-S direction, respectively. The simulated PGA values by deterministic method are 41.10 cm/s² in E-W direction and 55.76 cm/s² in N-S direction, whereas the peak ground acceleration, that recorded by station GYN for the 1999 Duzce earthquake, in E-W direction is 24.82 cm/s² and N-S direction is 27.89 cm/s².

In Figure 3.10, Comparison of Fourier Amplitude Spectra and the Response Spectra (with 5% damping ratio) of simulation results with real data for the 12 November 1999 Duzce earthquake at station GYN is given. At GYN station, the simulated results for long periods underestimate the observed values while the high frequency amplitudes are overestimated. These discrepancies may be attributed to source and site effects that could not be modeled accurately as well as the lack of surface waves in the simulated spectra.

According to the broadband results, both directions give accurate results where the misfits are given numerically in Table 3.11 and Table 3.12 with matching frequencies for FAS and RS (with 5% damping ratio), respectively. The matching frequency for E-W direction is 3.247 Hz and for N-S direction is 3.125 Hz. The results are better for the interval of 0 Hz and matching frequency in E-W direction, whe`re the FAS misfit is calculated as 0.4097, than in N-S direction. For the interval of matching frequency and 10 Hz in N-S direction, where the FAS misfit is calculated as 0.3858, the results are better than in E-W direction. The RS misfits are calculated as 0.3667 for E-W component and 0.2899 for N-S component where the results are satisfactory as FAS misfits. Other types of misfits for PGA and PGV are given in Table 3.13. In brief, it is observed that using broadband ground motion simulation for GYN station reduces misfit compared to using the stochastic method for the frequency range between 0 and 10 Hz in E-W direction and the misfits are close in N-S direction.

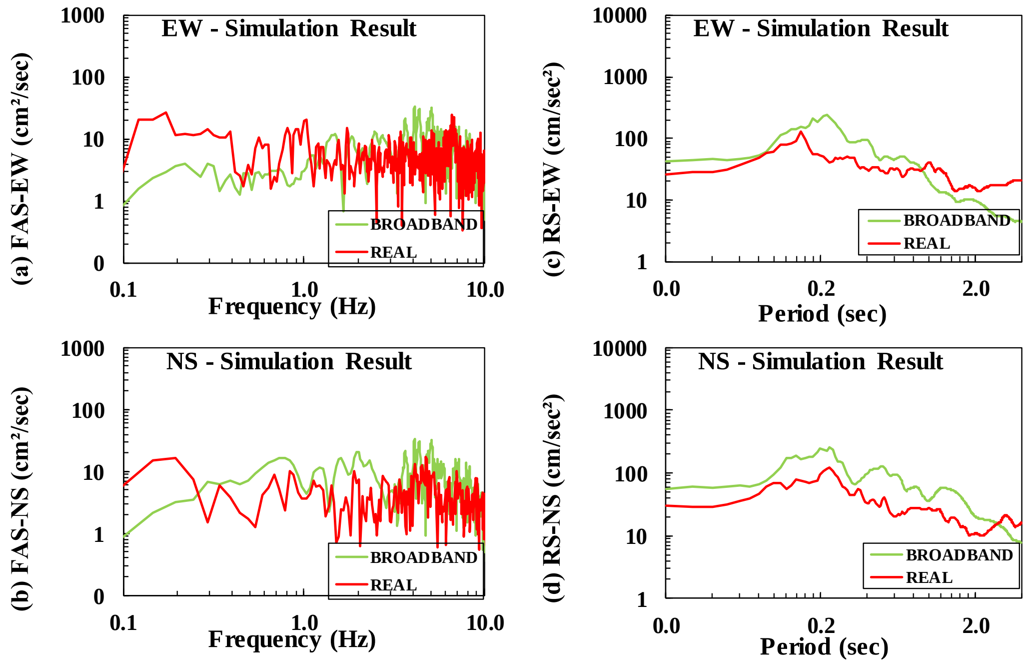

Figure 3.10. Comparison of real and simulated FAS [(a),(b)] and RS with 5% damping [(c),(d)] at station GYN for E-W and N-S components for the 12 November 1999 Duzce earthquake

Table 3.11. *FAS misfits of real records and simulation results for E-W and N-S components – station GYN*

Station GYN	Broadband Simulation Misfit			Stochastic Method Misfit
Directions	Matching f	0 Hz - f	f - 10 Hz	0 - 10 Hz
(E-W)	3.247 Hz	0.4097	0.3944	0.4015
(N-S)	3.125 Hz	0.5060	0.3858	0.4109

Table 3.12. *RS misfits of real records and simulation results for E-W and N-S components – station GYN*

Station GYN	Broadband Simulation Misfit	Stochastic Method Misfit
Directions	0 - 4 sec	0 - 4 sec
(E-W)	0.3667	0.2802
(N-S)	0.2899	0.3096

Table 3.13. *PGA and PGV misfits of real records and simulation results for E-W and N-S components – station GYN*

Station GYN / Directions	$Misfit_{PGA}$	$Misfit_{PGV}$
(E-W)	0.66	-0.68
(N-S)	1.00	-0.47

3.5.1.5. Station SKR

Station SKR is placed in the city of Sakarya. The coordinates are 40.73707 N° – 30.38005 E°.

The acceleration–time history comparison with PGA values for station SKR is given in Figure 3.11 in order for observed ground motion in E-W direction, observed ground motion in N-S direction and simulated ground motion by the deterministic method in E-W direction and in N-S direction, respectively. The simulated PGA values by deterministic method are 82.27 cm/s^2 in E-W direction and 71.30 cm/s^2 in N-S direction, whereas the peak ground acceleration, that recorded by station SKR for the 1999 Duzce earthquake, in E-W direction is 24.72 cm/s^2 and N-S direction is 17.33 cm/s^2.

In Figure 3.12, Comparison of Fourier Amplitude Spectra and the Response Spectra (with 5% damping ratio) of simulation results with real data for the 12 November 1999 Duzce earthquake at station SKR is given. When the result at SKR station is studied visually, it is observed that SKR provide closer values to the observed FAS.

According to the broadband results, both directions give accurate results where the misfits are given numerically in Table 3.14 and Table 3.15 with matching frequencies for FAS and RS (with 5% damping ratio), respectively. The matching frequency for E-W direction is 1.660 Hz and for N-S direction is 0.586 Hz. The results are better for the interval of 0 Hz and matching frequency in N-S direction, where the FAS misfit is calculated as 0.5520, than in E-W direction. For the interval of matching frequency and 10 Hz in E-W direction, where the FAS misfit is calculated as 0.3783, the results are better than in N-S direction. The RS misfits are calculated as 0.3361 for E-W component and 0.5782 for N-S component where the results are satisfactory as FAS misfits. Other types of misfits for PGA and PGV are given in Table 3.16. In brief, it is observed that using broadband ground motion simulation for SKR station reduces misfit compared to using the stochastic method for the frequency range between 0 and 10 Hz in E-W direction and the misfits are close in N-S direction.

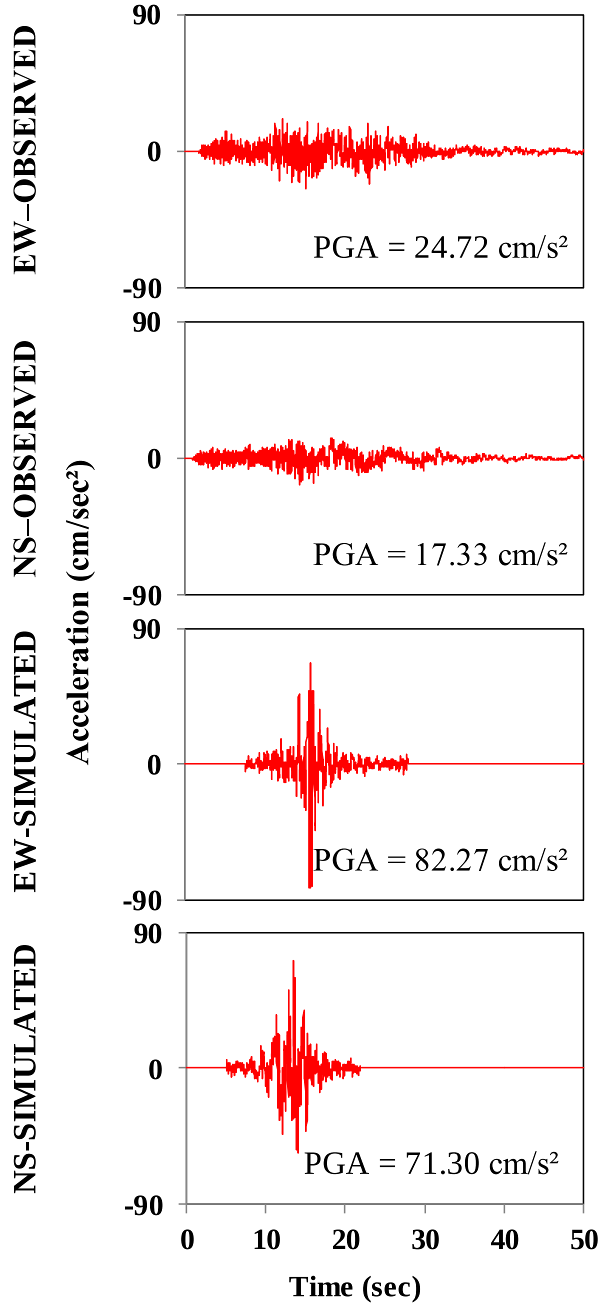

Figure 3.11. Comparison of acceleration-time histories of broadband results with real data for the 12 November 1999 Duzce earthquake in E-W and N-S direction – station SKR

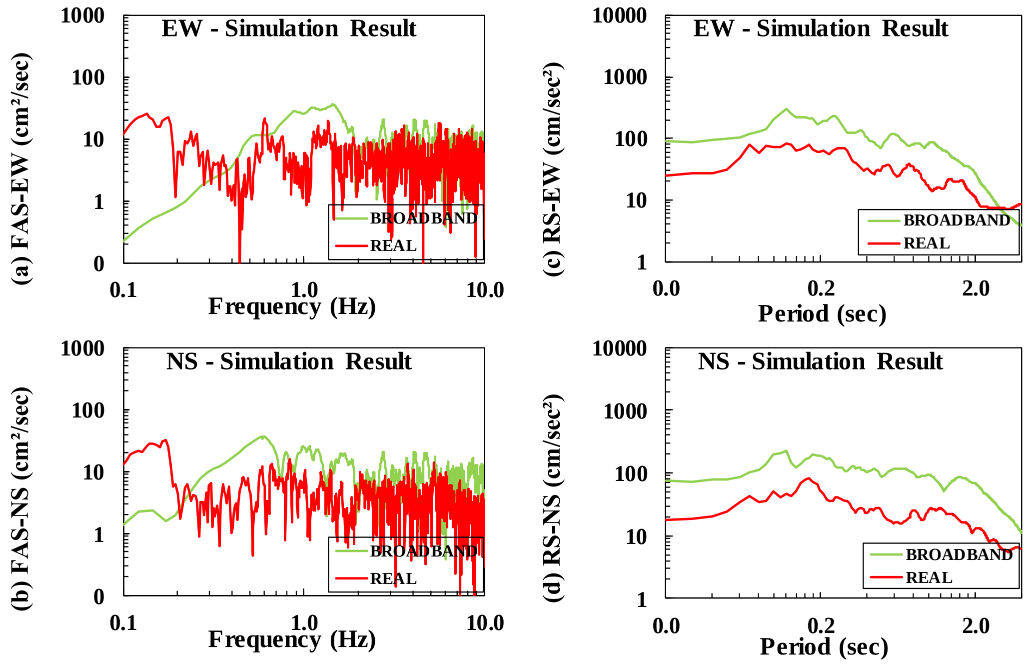

Figure 3.12. Comparison of real and simulated FAS [(a),(b)] and RS with 5% damping [(c),(d)] at station SKR for E-W and N-S components for the 12 November 1999 Duzce earthquake

Table 3.14. *FAS misfits of real records and simulation results for E-W and N-S components – station SKR*

Station SKR	Broadband Simulation Misfit			Stochastic Method Misfit
Directions	Matching f	0 Hz - f	f - 10 Hz	0 - 10 Hz
(E-W)	1.660 Hz	0.6192	0.3783	0.4054
(N-S)	0.586 Hz	0.5520	0.5001	0.5897

Table 3.15. *RS misfits of real records and simulation results for E-W and N-S components – station SKR*

Station SKR	Broadband Simulation Misfit	Stochastic Method Misfit
Directions	0 - 4 sec	0 - 4 sec
(E-W)	0.3361	0.7343
(N-S)	0.5782	0.7623

Table 3.16 *PGA and PGV misfits of real records and simulation results for E-W and N-S components – station SKR*

Station SKR / Directions	$Misfit_{PGA}$	$Misfit_{PGV}$
(E-W)	2.33	0.04
(N-S)	3.11	0.54

3.5.1. Comparison of Spatial Distribution of Simulated Peak Ground Motion Values for the Scenario Earthquakes

Ground motion simulations are performed for the 1999 Duzce event ($M_w = 7.1$) and scenario events ($M_w = 6.5$ and $M_w = 6.0$) at selected nodes located within a region bounded by 40°- 41° latitudes and 30.6°- 32° longitudes with a regular grid spacing of 0.2°. To perform simulations at nodes, where velocity profiles are not available, the velocity model from Asten *et al.* (2014) at the closest possible site is used.

The main aim is to observe the distribution of the simulated peak ground motions in a wider area in the study region. As used in broadband ground motion simulations for selected four real stations, the main average H/V ratio is used for the high frequency portion with a kappa factor of 0.047. In the Figure 3.13, the yellow rectangular shows the region used for spatial distribution. Node numbers that have a grid spacing of 0.2° in both directions are given with blue color in the Figure 3.14.

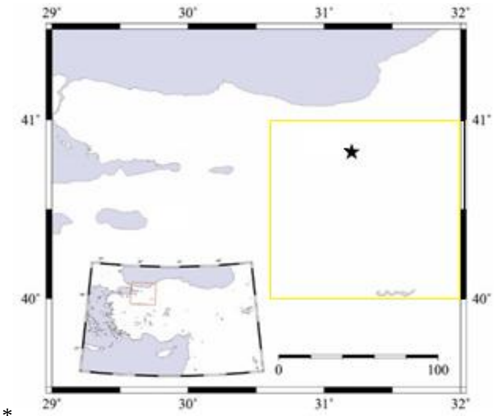

*

Figure 3.13. Region used for synthetics

Spatial distribution of simulated PGA and PGV values are presented in Figure 3.15 for $M_w = 7.1$ event, in Figure 3.16 for $M_w = 6.5$ event, and in Figure 3.17 for $M_w = 6.0$ event. Results reveal that maximum peak ground motion values in both directions are observed at nodes located in close vicinity of the fault plane which also have softer soil conditions. The simulated values for $M_w = 7.1$, $M_w = 6.5$ and $M_w = 6.0$ earthquakes are given in Table 3.17, Table 3.18 and Table 3.19 in terms of PGA and PGV in EW and NS direction with the corresponding coordinates.

The high PGA and PGV values explain the widespread damage observed in the 1999 Duzce earthquake. The spatial distributions of the simulated peaks are consistent with the damage distribution in the region. However, some nodes are close to the hypocenter of the 1999 Duzce earthquake which causes unrealistic results by the deterministic approach (Spudich and Xu, 2003). Similar to results of Station DZC, PGA and PGV values in both EW and NS direction of Node 54 and Node 55 are unrealistic compared to observed values in the 1999 Duzce earthquake. The values can be seen from Table 3.17 and the maximum PGA and PGV values are shown in bolt.

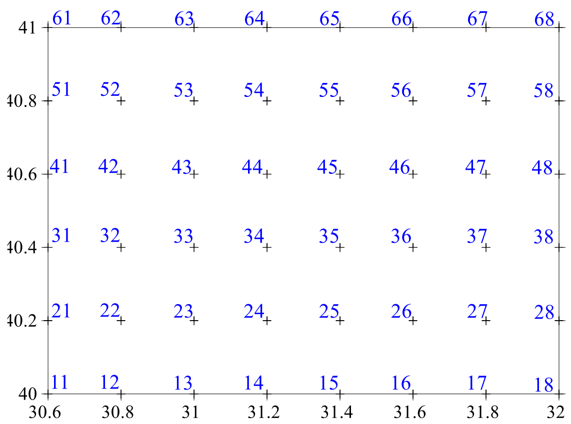

Figure 3.14. Node numbers

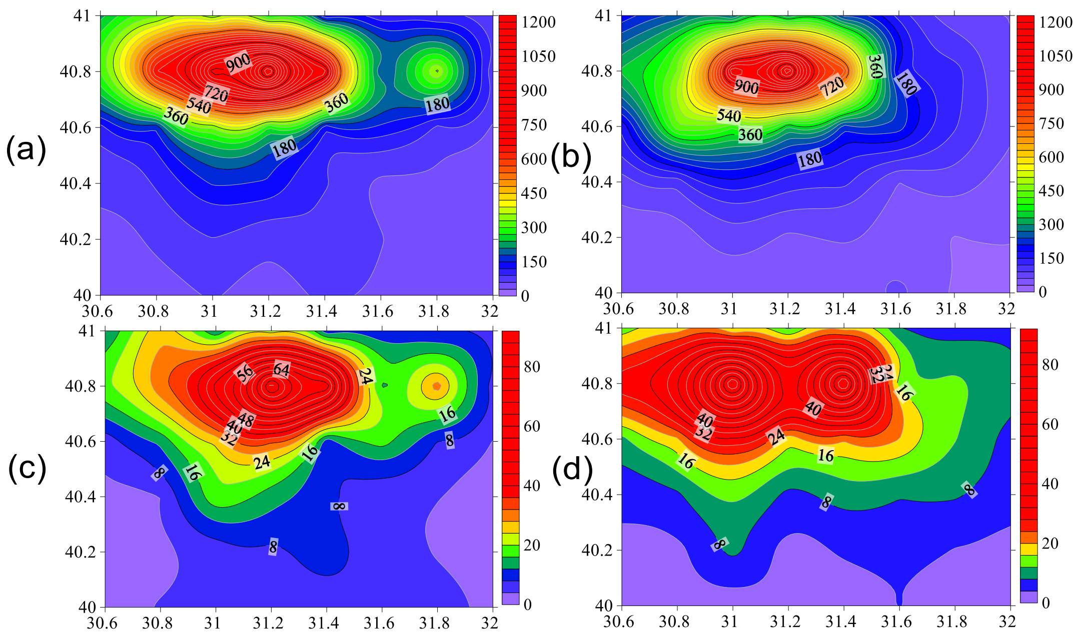

Figure 3.15. Spatial distribution of simulated (a) PGA (cm/s²) in E-W direction, (b) PGA (cm/s²) in N-S direction, (c) PGV (cm/s) in E-W direction and (d) PGV (cm/s) in N-S direction for the 1999 Duzce event (Mw=7.1)

Table 3.17. *Simulated PGA and PGV in E-W and N-S directions for the 1999 Duzce event (Mw=7.1)*

Node	Latitude (°)	Longitude (°)	EW Direction PGA (cm/s²)	EW Direction PGV (cm/s)	NS Direction PGA (cm/s²)	NS Direction PGV (cm/s)
Node 11	40.0	30.6	40.14	2.954	34.907	1.945
Node 12	40.0	30.8	46.153	4.263	35.83	2.3
Node 13	40.0	31.0	62.543	6.08	42.405	2.419
Node 14	40.0	31.2	46.845	5.017	34.147	3.089
Node 15	40.0	31.4	64.893	6.366	39.822	2.444
Node 16	40.0	31.6	53.602	6.412	67.312	4.075
Node 17	40.0	31.8	34.909	5.08	26.637	2.473
Node 18	40.0	32.0	31.74	3.408	17.028	1.978
Node 21	40.2	30.6	41.305	2.454	52.614	3.238
Node 22	40.2	30.8	67.025	2.799	45.609	3.081
Node 23	40.2	31.0	89.303	5.845	77.716	9.026
Node 24	40.2	31.2	65.423	7.266	54.516	2.544
Node 25	40.2	31.4	87.492	9.87	63.746	4.512
Node 26	40.2	31.6	61.81	5.761	45.767	4.818
Node 27	40.2	31.8	34.443	3.803	29.1	3.861
Node 28	40.2	32.0	35.929	2.699	32.612	2.554
Node 31	40.4	30.6	78.445	3.6	76.679	5.546
Node 32	40.4	30.8	94.26	4.056	101.588	7.35
Node 33	40.4	31.0	153.181	19.252	173.135	13.36
Node 34	40.4	31.2	145.879	13.825	138.295	6.951
Node 35	40.4	31.4	94.014	9.052	129.589	10.244
Node 36	40.4	31.6	54.811	5.402	59.943	8.4
Node 37	40.4	31.8	56.702	4.17	76.264	8.485
Node 38	40.4	32.0	43.807	2.593	43.027	5.904
Node 41	40.6	30.6	108.85	5.699	155.217	10.752
Node 42	40.6	30.8	157.222	12.936	442.422	19.325
Node 43	40.6	31.0	335.14	25.139	400.361	31.17
Node 44	40.6	31.2	269.147	32.862	331.595	17.467
Node 45	40.6	31.4	128.663	9.253	225.168	20.768
Node 46	40.6	31.6	142.534	17.725	226.426	20.017
Node 47	40.6	31.8	82.61	7.817	123.376	12.172
Node 48	40.6	32.0	56.28	3.874	66.206	6.569
Node 51	40.8	30.6	302.735	19.177	335.745	31.203
Node 52	40.8	30.8	663.34	30.567	450.723	39.666
Node 53	40.8	31.0	916.974	49.266	1021.222	**81.773**
Node 54	40.8	31.2	**1157.545**	**86.114**	**1176.609**	36.971
Node 55	40.8	31.4	770.5	66.957	801.32	74.083
Node 56	40.8	31.6	187.474	15.391	169.86	13.958
Node 57	40.8	31.8	371.108	30.135	131.423	13.027
Node 58	40.8	32.0	69.951	6.501	59.805	9.271
Node 61	41.0	30.6	228.357	11.639	190.296	13.691
Node 62	41.0	30.8	318.827	27.08	247.826	17.831
Node 63	41.0	31.0	333.934	11.946	260.093	15.414
Node 64	41.0	31.2	262.846	21.714	300.391	10.648
Node 65	41.0	31.4	124.845	8.902	230.425	18.536
Node 66	41.0	31.6	100.708	8.839	139.14	8.235
Node 67	41.0	31.8	93.248	7.852	74.368	6.709
Node 68	41.0	32.0	60.06	6.314	59.043	7.007

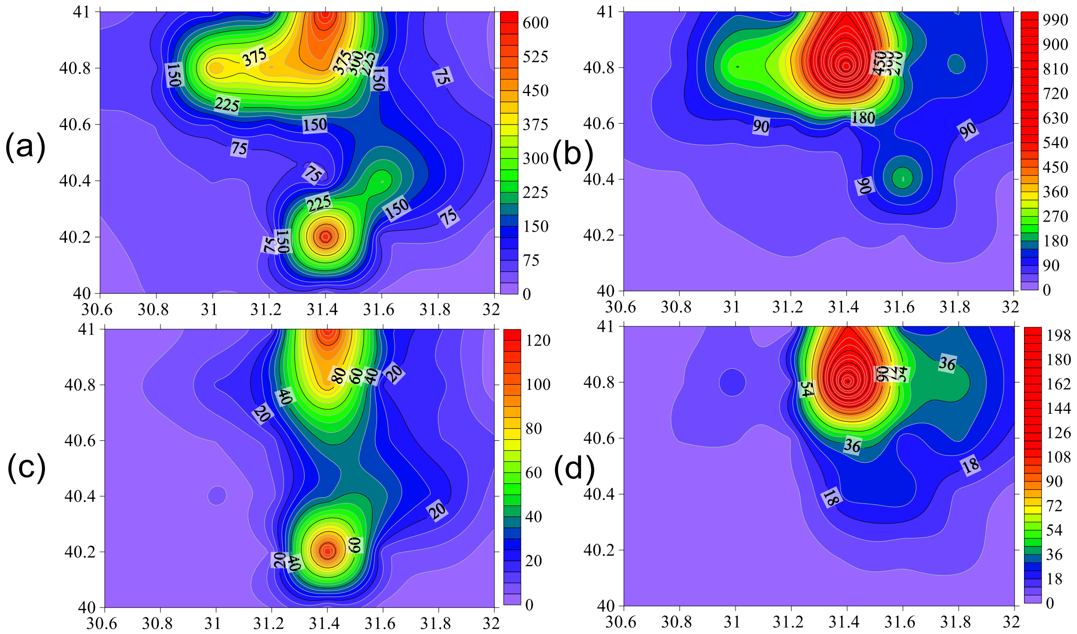

Figure 3.16. Spatial distribution of simulated (a) PGA (cm/s²) in E-W direction, (b) PGA (cm/s²) in N-S direction, (c) PGV (cm/s) in E-W direction and (d) PGV (cm/s) in N-S direction for scenario event Mw=6.5

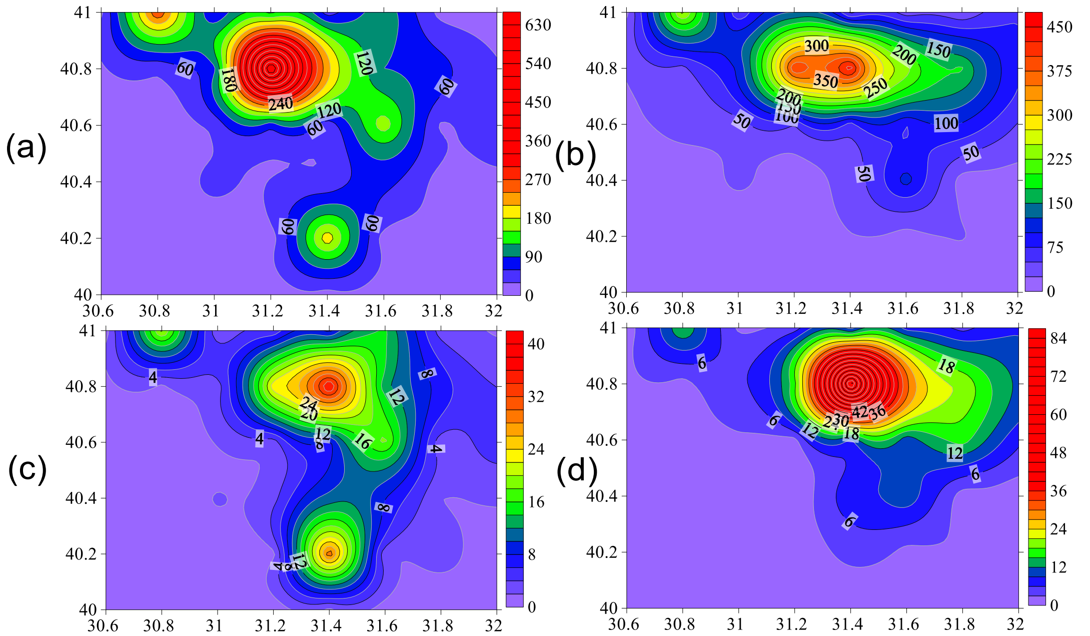

Figure 3.17. Spatial distribution of simulated (a) PGA (cm/s²) in E-W direction, (b) PGA (cm/s²) in N-S direction, (c) PGV (cm/s) in E-W direction and (d) PGV (cm/s) in N-S direction for scenario event Mw=6.0

Table 3.18. *Simulated PGA and PGV in E-W and N-S directions for scenario event Mw=6.5*

Node	Latitude (°)	Longitude (°)	EW Direction PGA (cm/s²)	EW Direction PGV (cm/s)	NS Direction PGA (cm/s²)	NS Direction PGV (cm/s)
Node 11	40.0	30.6	7.785	0.782	11.65	1.08
Node 12	40.0	30.8	29.611	2.521	13.804	1.137
Node 13	40.0	31.0	25.4	4.426	19.033	1.465
Node 14	40.0	31.2	41.437	5.325	24.118	1.145
Node 15	40.0	31.4	29.987	7.874	25.077	3.496
Node 16	40.0	31.6	18.863	2.465	23.177	2.837
Node 17	40.0	31.8	12.639	1.012	9.864	1.386
Node 18	40.0	32.0	11.775	1.086	10.233	1.14
Node 21	40.2	30.6	21.676	1.514	13.793	0.9
Node 22	40.2	30.8	32.999	2.952	22.855	1.119
Node 23	40.2	31.0	39.742	4.448	29.359	2.606
Node 24	40.2	31.2	43.33	5.724	36.344	1.339
Node 25	40.2	31.4	595.392	118.986	30.642	7.687
Node 26	40.2	31.6	54.854	11.59	28.59	7.982
Node 27	40.2	31.8	55.735	8.401	55.688	10.391
Node 28	40.2	32.0	16.092	2.076	23.215	1.691
Node 31	40.4	30.6	30.25	1.622	22.581	1.643
Node 32	40.4	30.8	43.877	2.067	23.665	2.4
Node 33	40.4	31.0	51.359	5.841	52.604	4.314
Node 34	40.4	31.2	60.425	7.531	51.495	3.118
Node 35	40.4	31.4	64.427	33.687	58.385	26.636
Node 36	40.4	31.6	257.041	36.857	219.697	28.733
Node 37	40.4	31.8	137.151	24.531	49.895	10.397
Node 38	40.4	32.0	61.964	7.712	22.165	3.406
Node 41	40.6	30.6	46.035	2.958	42.658	3.872
Node 42	40.6	30.8	51.642	2.917	81.04	6.255
Node 43	40.6	31.0	98.747	5.098	76.059	6.631
Node 44	40.6	31.2	120.518	12.45	92.245	6.003
Node 45	40.6	31.4	138.185	41.692	92.633	39.392
Node 46	40.6	31.6	150.672	26.553	104.585	19.965
Node 47	40.6	31.8	98.026	15.35	98.746	31.74
Node 48	40.6	32.0	73.476	10.816	80.443	15.323
Node 51	40.8	30.6	68.967	4.555	50.734	4.66
Node 52	40.8	30.8	66.691	6.199	65.377	5.471
Node 53	40.8	31.0	430.902	15.625	274.725	15.743
Node 54	40.8	31.2	430.128	30.259	354.016	12.004
Node 55	40.8	31.4	466.914	87.437	**986.801**	**186.586**
Node 56	40.8	31.6	119.081	19.131	162.058	45.499
Node 57	40.8	31.8	77.954	17.195	160.792	40.407
Node 58	40.8	32.0	21.987	2.212	88.011	20.586
Node 61	41.0	30.6	44.263	2.989	29.591	2.895
Node 62	41.0	30.8	60.088	3.278	46.908	2.714
Node 63	41.0	31.0	104.518	6.653	144.966	9.272
Node 64	41.0	31.2	110.704	12.51	88.774	2.144
Node 65	41.0	31.4	**609.338**	**119.102**	629.873	109.408
Node 66	41.0	31.6	158.793	28.822	140.048	26.444
Node 67	41.0	31.8	56.078	15.993	152.75	31.008
Node 68	41.0	32.0	23.281	2.923	67.674	17.324

Table 3.19. *Simulated PGA and PGV in E-W and N-S directions for scenario event Mw=6.0*

Node	Latitude (°)	Longitude (°)	EW Direction PGA (cm/s²)	EW Direction PGV (cm/s)	NS Direction PGA (cm/s²)	NS Direction PGV (cm/s)
Node 11	40.0	30.6	5.929	0.5	6.671	0.464
Node 12	40.0	30.8	11.726	1.001	7.799	0.53
Node 13	40.0	31.0	13.832	1.538	6.441	0.371
Node 14	40.0	31.2	9.46	0.707	9.686	0.61
Node 15	40.0	31.4	17.415	1.422	14.87	1.074
Node 16	40.0	31.6	10.265	0.961	12.641	1.52
Node 17	40.0	31.8	6.193	0.42	7.414	0.62
Node 18	40.0	32.0	7.368	0.612	5.42	0.572
Node 21	40.2	30.6	16.501	0.578	8.921	0.536
Node 22	40.2	30.8	16.232	1.158	9.209	0.501
Node 23	40.2	31.0	14.876	1.954	11.497	0.918
Node 24	40.2	31.2	16.514	1.292	15.141	0.681
Node 25	40.2	31.4	202.712	29.814	24.03	4.051
Node 26	40.2	31.6	17.341	2.434	15.147	2.098
Node 27	40.2	31.8	29.615	3.213	26.941	2.858
Node 28	40.2	32.0	6.638	0.608	10.055	0.753
Node 31	40.4	30.6	11.75	0.585	15.51	0.893
Node 32	40.4	30.8	13.84	0.831	13.382	0.745
Node 33	40.4	31.0	39.21	2.168	29.962	1.381
Node 34	40.4	31.2	30.812	3.327	20.514	1.341
Node 35	40.4	31.4	34.185	10.781	35.515	8.578
Node 36	40.4	31.6	69.442	8.056	110.572	11.082
Node 37	40.4	31.8	18.873	2.028	15.025	1.542
Node 38	40.4	32.0	24.295	2.322	15.458	0.959
Node 41	40.6	30.6	14.043	0.728	22.559	1.272
Node 42	40.6	30.8	21.025	1.004	32.734	2.649
Node 43	40.6	31.0	36.898	2.164	37.801	2.665
Node 44	40.6	31.2	67.903	2.779	50.975	2.012
Node 45	40.6	31.4	36.014	7.353	63.426	8.266
Node 46	40.6	31.6	168.039	18.486	74.885	9.898
Node 47	40.6	31.8	25.744	2.651	98.048	16.381
Node 48	40.6	32.0	55.67	5.63	48.54	6.582
Node 51	40.8	30.6	26.591	1.462	28.563	2.374
Node 52	40.8	30.8	35.482	1.55	41.9	2
Node 53	40.8	31.0	79.956	3.146	105.544	5.429
Node 54	40.8	31.2	**652.897**	23.308	399.462	16.999
Node 55	40.8	31.4	221.466	**36.661**	**440.352**	**87.124**
Node 56	40.8	31.6	89.694	12.521	235.913	30.768
Node 57	40.8	31.8	73.014	7.224	178.239	20.602
Node 58	40.8	32.0	32.063	3.975	77.181	11.314
Node 61	41.0	30.6	24.069	1.151	17.929	1.123
Node 62	41.0	30.8	271.571	20.533	258.078	15.059
Node 63	41.0	31.0	57.409	2.508	54.341	2.429
Node 64	41.0	31.2	112.147	4.424	123.964	4.347
Node 65	41.0	31.4	44.189	7.328	41.613	7.377
Node 66	41.0	31.6	112.328	14.354	35.506	7.533
Node 67	41.0	31.8	20.615	2.96	27.675	4.87
Node 68	41.0	32.0	18.709	1.784	72.532	8.543

3.5.1. Comparison of Attenuation of Simulated Data against Ground Motion Prediction Equations

The results of broadband simulations are compared against selected recent ground motion prediction equations (GMPE). In this study, models by Boore and Atkinson in (2008 BA08) and Akkar and Cagnan in (2010 AC10) are used.

The comparisons are made for two different cases: One is for the peaks of the records of the 1999 Duzce earthquake ($M_w = 7.1$) at the selected four real stations and the other is for the peaks at the nodes where ground motions are simulated for the 1999 Duzce earthquake $M_w = 7.1$, and for the scenario earthquakes $M_w = 6.5$ and $M_w = 6.0$.

The PGA and PGV values calculated using corresponding GMPE's at the 4 stations for the 1999 Duzce earthquake are given in Table 3.20 and Table 3.21, respectively. In these tables, real and simulated PGA and PGV values are also presented. For scenario earthquakes of other M_w values, PGA and PGV values are given in Appendix B in table format.

When we compare the simulated peak ground acceleration values with the one predicted using BA08, it is observed that the values are close to each other except BOL station. For AC10, BOL station in NS direction and DZC station give good match as given in Figure 3.18. The simulated PGV values are also compared with AC10 and BA08 in Figure 3.19. DZC and GYN stations give satisfactory matches with BA08, whereas SKR station matches with AC10 better than with BA08. PGA and PGV values of BOL station are unsatisfactory.

Table 3.20. *Comparison of real and simulated PGA values of four stations with empirical estimates from GMPE's for the 1999 Duzce earthquake (Mw=7.1)*

Stations	PGA (cm/s²)					
	Real EW	Real NS	Simulated EW	Simulated NS	Estimated using BA08	Estimated using AC10
BOL	805.88	739.51	384.19	620.59	255.15	197.39
DZC	513.78	407.69	332.32		521.91	367.97
GYN	24.82	27.89	100.19	104.02	131.73	62.68
SKR	24.72	17.33	52.44	48.89	158.68	83.54

Table 3.21. *Comparison of real and simulated PGV values of four stations with empirical estimates from GMPE's for the 1999 Duzce earthquake (Mw=7.1)*

Stations	PGV (cm/s)					
	Real EW	Real NS	Simulated EW	Simulated NS	Estimated using BA08	Estimated using AC10
BOL	66.61	57.78	40.71	60.74	26.91	20.30
DZC	90.78	66.47	70.69		65.34	36.69
GYN	8.68	9.84	12.33	9.36	12.18	8.77
SKR	5.17	4.81	4.27	2.76	14.78	10.75

Comparison of the simulated PGA and PGV values for the 1999 Duzce earthquake $M_w = 7.1$ at 48 stations are made against AC10 and BA08 GMPE's in Figure 3.20 and Figure 3.21, respectively. Similarly, comparison of simulated PGA and PGV values from the scenario earthquakes of $M_w = 6.5$ and $M_w = 6.0$ at 48 stations are made against AC10 and BA08 in Figure 3.22, Figure 3.23, Figure 3.24 and Figure 3.25. For the 1999 Duzce earthquake of $M_w = 7.1$ and for the scenario earthquakes $M_w = 6.5$ and $M_w = 6.0$, comparison of simulated PGA and PGV values against AC10 and BA08 GMPE's are given in Appendix B, in Table B.1, Table B.2 and Table B.3, respectively.

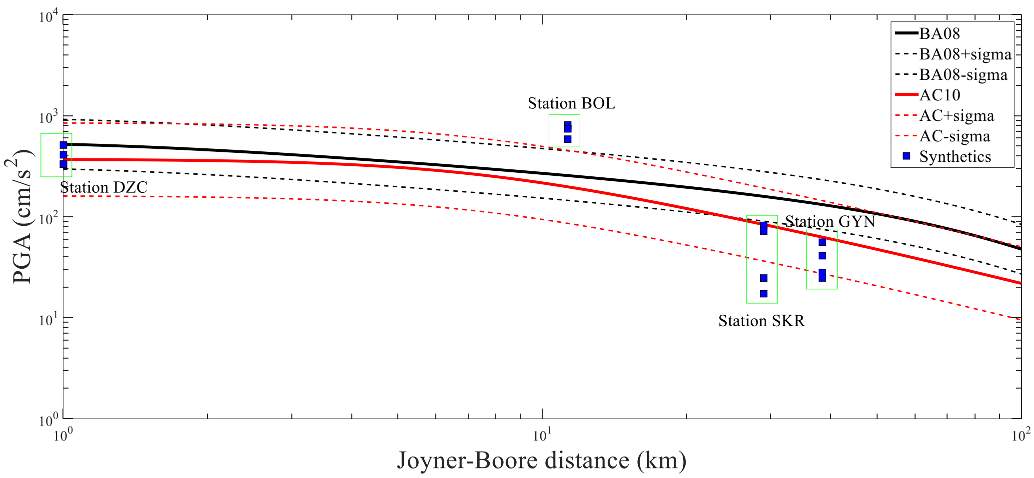

Figure 3.18. Comparison of PGA values of broadband results with PGA values from GMPE's with respect to Joyner – Boore distance at stations DZC, BOL, GYN and SKR

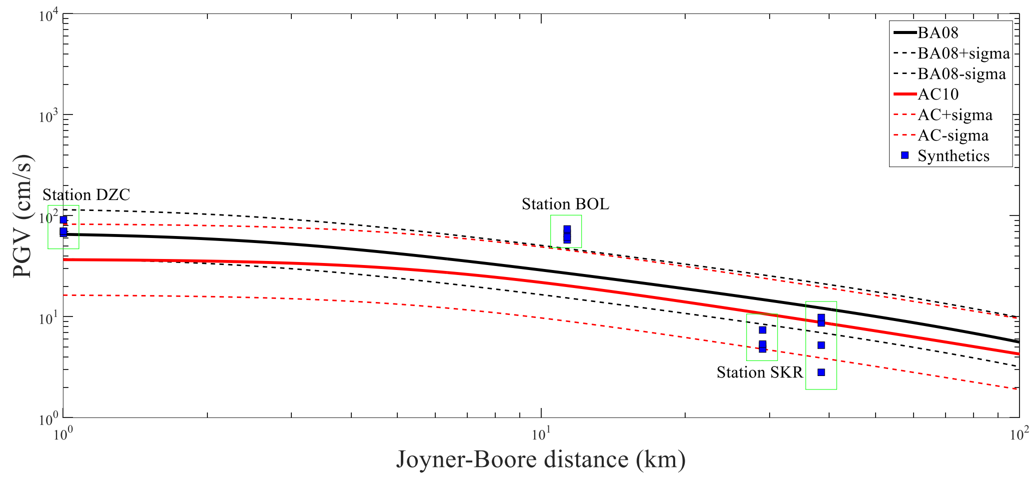

Figure 3.19. Comparison of PGV values of broadband results with PGV values from GMPE's with respect to Joyner – Boore distance at stations DZC, BOL, GYN and SKR

As shown in Figure 3.20, PGA values of broadband results for far nodes, give good match with AC10, meanwhile PGA values of broadband results for near-field nodes, give good match with BA08 for the 1999 Duzce earthquake $M_w = 7.1$. In Figure 3.21, while the Joyner-Boore distances increases, PGV values of broadband results get closer to AC10.

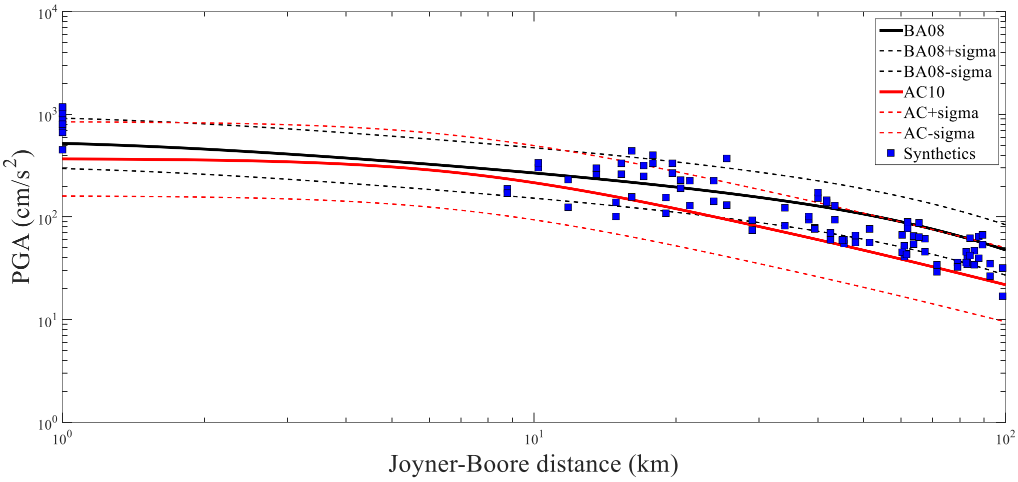

Figure 3.20. Comparison of PGA values of broadband results with PGA values from GMPE's with respect to Joyner – Boore distance for the 1999 Duzce earthquake Mw=7.1

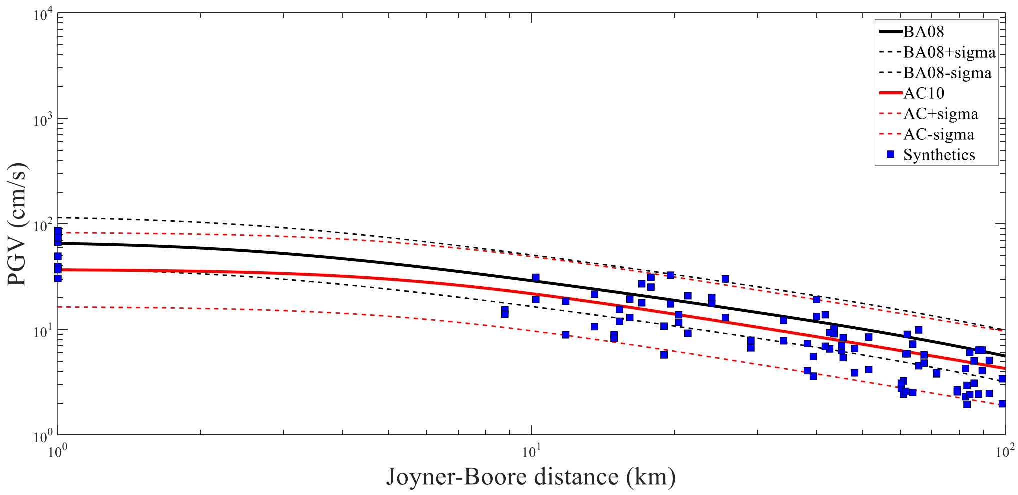

-*Figure 3.21.* Comparison of PGV values of broadband results with PGV values from GMPE's with respect to Joyner – Boore distance for the 1999 Duzce earthquake Mw=7.1

As shown in Figure 3.22, PGA values of broadband results for near-field nodes located on west side of fault plane, give good match with AC10, meanwhile PGA values of broadband results for near-field nodes for near nodes located on east side of fault plane, give good match with BA08 for scenario earthquake $M_w = 6.5$. In Figure 3.23, PGV values of broadband results in some nodes, are overestimated compared to both GMPE's for scenario earthquake $M_w = 6.5$.

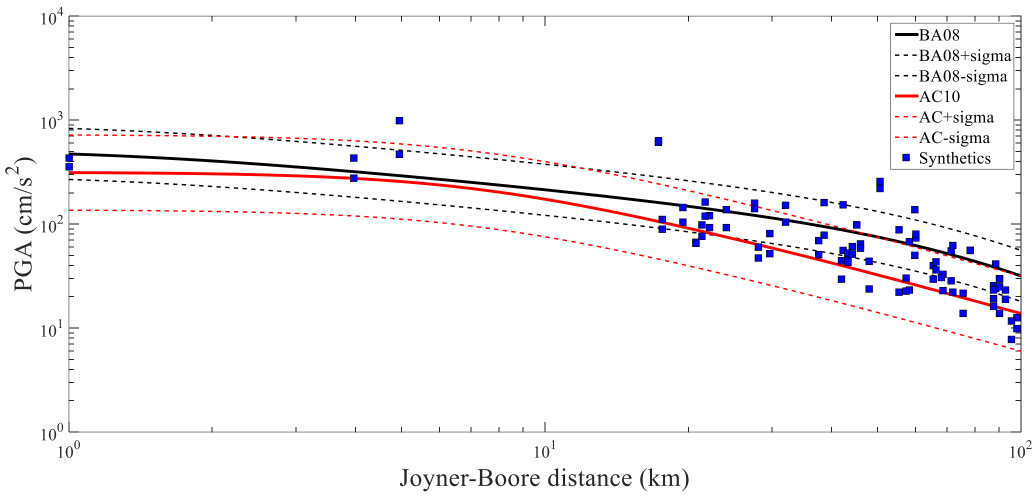

Figure 3.22. Comparison of PGA values of broadband results with PGA values from GMPE's with respect to Joyner – Boore distance for scenario earthquake Mw=6.5

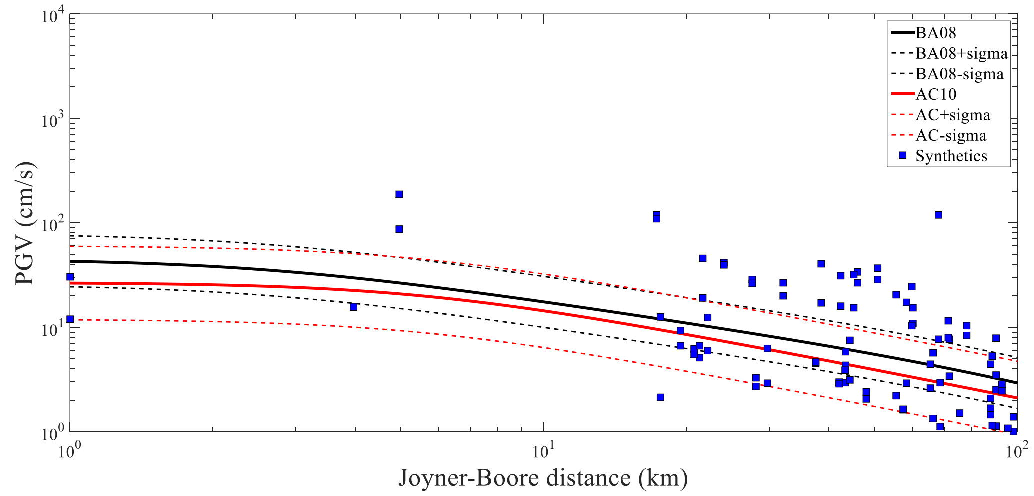

Figure 3.23. Comparison of PGV values of broadband results with PGV values from GMPE's with respect to Joyner – Boore distance for scenario earthquake Mw=6.5

In Figure 2.24 and 2.25, PGA and PGV values of broadband results in some nodes, are overestimated compared to both GMPE's for scenario earthquake $M_w = 6.0$.

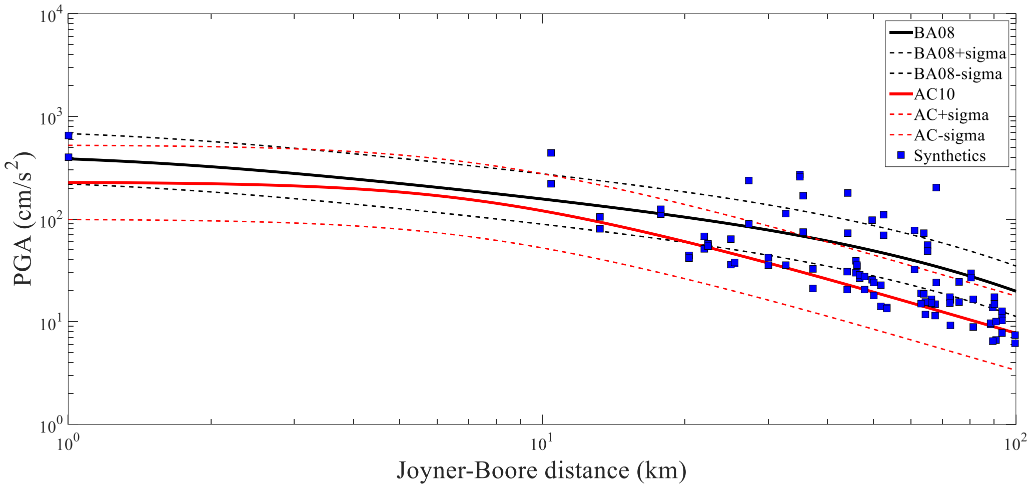

Figure 3.24. Comparison of PGA values of broadband results with PGA values from GMPE's with respect to Joyner – Boore distance for scenario earthquake Mw=6.0

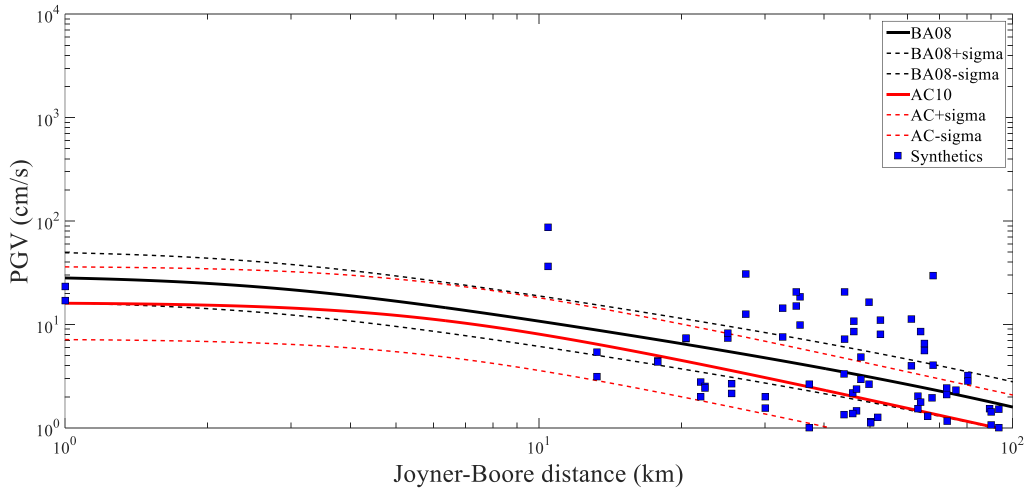

Figure 3.25. Comparison of PGV values of broadband results with PGV values from GMPE's with respect to Joyner – Boore distance for scenario earthquake Mw=6.0

When the simulated PGA values for the scenario earthquakes at the 48 nodes are compared with the values predicted using BA08 are compared, the values are observed to be closer than using AC10. The PGA and PGV values of some far nodes yield unsatisfactory results for all scenario earthquakes.

CHAPTER 4

BUILDING RESPONSE OF SELECTED FRAME BUILDINGS WITH REAL AND SIMULATED RECORDS OF 12 NOVEMBER 1999 DUZCE EARTHQUAKE

4.1. General

In this chapter, building response of selected frame buildings with real and simulated records of 12 November 1999 Duzce earthquake is investigated. In Section 4.2, the methodology for dynamic analysis of frame models is explained. In Section 4.3, the building response simulations of selected frames are given.

The objective of such an exercise is to observe whether the simulated ground motions can be used in earthquake engineering. For this purpose, typical frames are selected and analyzed with both real and simulated data.

4.2. Methodology for Dynamic Analysis: Nonlinear Time History Analysis

Other than comparing with real records, one way to validate the simulated motions is to use them in earthquake engineering analyses. In this thesis, nonlinear Time History Analyses (NLTHA) is carried out to see how the structures behave under real and simulated ground motions. The main reason for selecting this method is to estimate detailed and accurate inelastic behavior of structures. One of the strengths of the method of analysis is its ability to model geometric nonlinearities, distributions of inelasticity in terms of spatial and temporal, and extensive types of inelastic material behaviors.

The Multi-Degree-of-Freedom (MDOF) equation of motion is given as follows:

$$\boldsymbol{M} \cdot \underline{\ddot{u}} + \boldsymbol{C} \cdot \underline{\dot{u}} + \boldsymbol{Fs}(\underline{u}) = -\boldsymbol{M} \cdot \underline{\ddot{u}}_g \tag{4.1}$$

where $\underline{u}$ is the nodal displacement vector, $\underline{\dot{u}}$ and $\underline{\ddot{u}}$ are first and second time derivatives of $\underline{u}$ representing ground velocity and acceleration vectors; $\underline{\ddot{u}}_g$ is the ground acceleration, $\boldsymbol{M}$ is the mass matrix, $\boldsymbol{C}$ is the damping matrix and $\boldsymbol{Fs}(\underline{u})$ is the resisting force vector.

To assess structural responses, OpenSees platform (http://opensees.berkeley.edu) which uses finite element method is employed. The program is developed at the University of California at Berkeley. The performance of structural systems with earthquake ground motions is simulated with the program. Additionally, nonlinear time history analysis can be also performed.

There are some limitations of NLTHA besides the advantages. The inelastic behavior of structures estimated by NLTHA is sensitive to the ground motion records used as input in the analysis. Additionally, because the equation of motion is nonlinear, some uncertainties can occur in the solution depending on the numerical solution approaches and the related assumptions.

In this thesis, since the same algorithms are used in analyses with both real and simulated motions, the corresponding errors are considered to be negligible.

4.3. Selected Frames For Building Response Simulation

Three frames are selected for building response simulations which are regular and symmetric two-dimensional reinforced concrete (RC) frames. The first frame (F3S2B) has 3 storeys (3 m storey height) and 2 bays (6 m bay width). The second frame (F4S3B) has 4 storeys (3 m storey height) and 3 bays (5 m bay width). The third and last frame (F8S3B) has 8 storeys (3.9624 m storey height) and 3 bays (7.3152 m bay width).

F3S2B is the deficient form of an existing structure located in Bursa city center (Turkey) (Karimzadeh, 2016). F4S3B is designed by Karimzadeh (2016) with using seismic zone as Zone 1, which is the most active seismic zone and the effective peak ground acceleration of the design spectrum is 0.4g according to Turkish seismic design code (1997). Lastly, F8S3B is designed according to 1982 Uniform Building Code in California (Kadaş, 2006; Yılmaz, 2007).

The storey masses and fundamental periods of the selected frames are presented in Table 4.1. It is assumed that dead load contributes 100% while live load contributes 25% to the total mass. The damping ratio is selected as 5% for all frames. The cross-sectional views for frames are shown in Figure 4.1 to Figure 4.3. The sectional and geometric properties of the three frames are provided in Table 4.2 to Table 4.4.

Table 4.1. *Total mass and fundamental periods of selected frames*

Frame ID	Storey Masses (tons)		Total Mass (tons)	Fundamental Period (sec)
F3S2B	1st Storey	88.851	226.48	0.7177
	2nd Storey	88.851		
	3rd Storey	48.777		
F4S3B	1st Storey	60.630	212.20	0.6925
	2nd Storey	60.630		
	3rd Storey	60.630		
	4th Storey	30.310		
F8S3B	1st Storey	230.450	1816.07	1.3064
	2nd Storey	230.450		
	3rd Storey	230.450		
	4th Storey	230.450		
	5th Storey	230.450		
	6th Storey	230.450		
	7th Storey	230.450		
	8th Storey	202.920		

In modeling of the selected RC frames, nonlinear fiber-based beam-column elements are selected. The fiber-based element type is the most reliable and efficient in computation of the biaxial bending and axial force models (Taucer *et al.*, 1991). The fiber-based beam-column element model can be expressed as a combination of concrete fibers and longitudinal steel.

In the OpenSees program, plasticity is distributed throughout the element and the dynamic inelastic behavior of structural elements can be chosen with the particular element type. By the integration of the stress-strain relationship of the concrete fibers, the force-deformation relationship of the section is obtained. The definition of the nonlinear force-deformation relationship of the element is not necessary, because the nonlinear behavior of the element is obtained entirely from the nonlinear stress-strain relation of the concrete fibers. Additionally, the shear deformations are neglected, since it is assumed in the model that the plane sections remain plane under any small displacement or deformation during loading history. In the model, the shearing and torsional deformation effects are also assumed as small enough for taken into account in the formulation of the element.

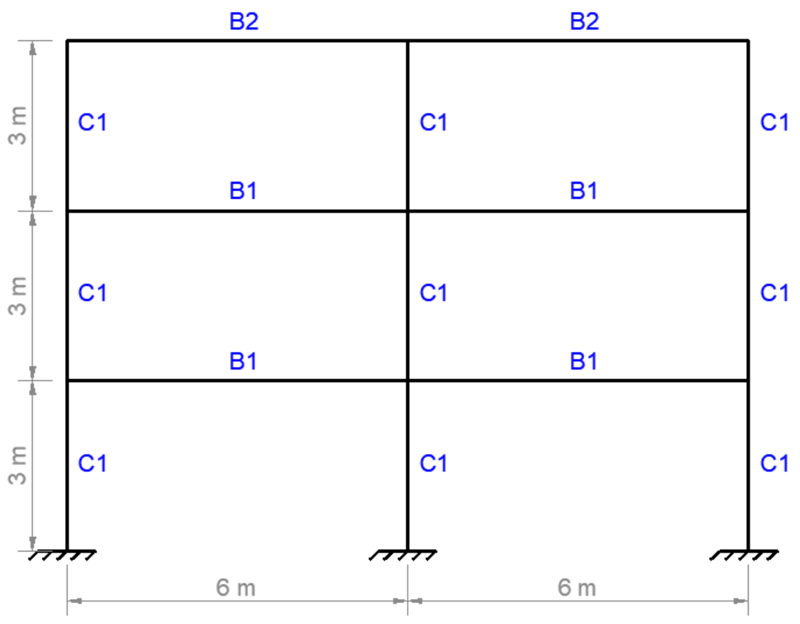

Figure 4.1. Cross-Sectional View of Frame F3S2B

Table 4.2. *Sectional properties of Frame F3S2B*

Structural Member	Width (mm)	Depth (mm)	Clear Cover (mm)	Total Reinforcing Rebar Area (mm^2)	
Column C1	500	500	50	2942.12	
Beam B1	250	500	50	1073.60 (top)	2518.40 (bottom)
Beam B2	250	500	50	1073.60 (top)	2002.40 (bottom)

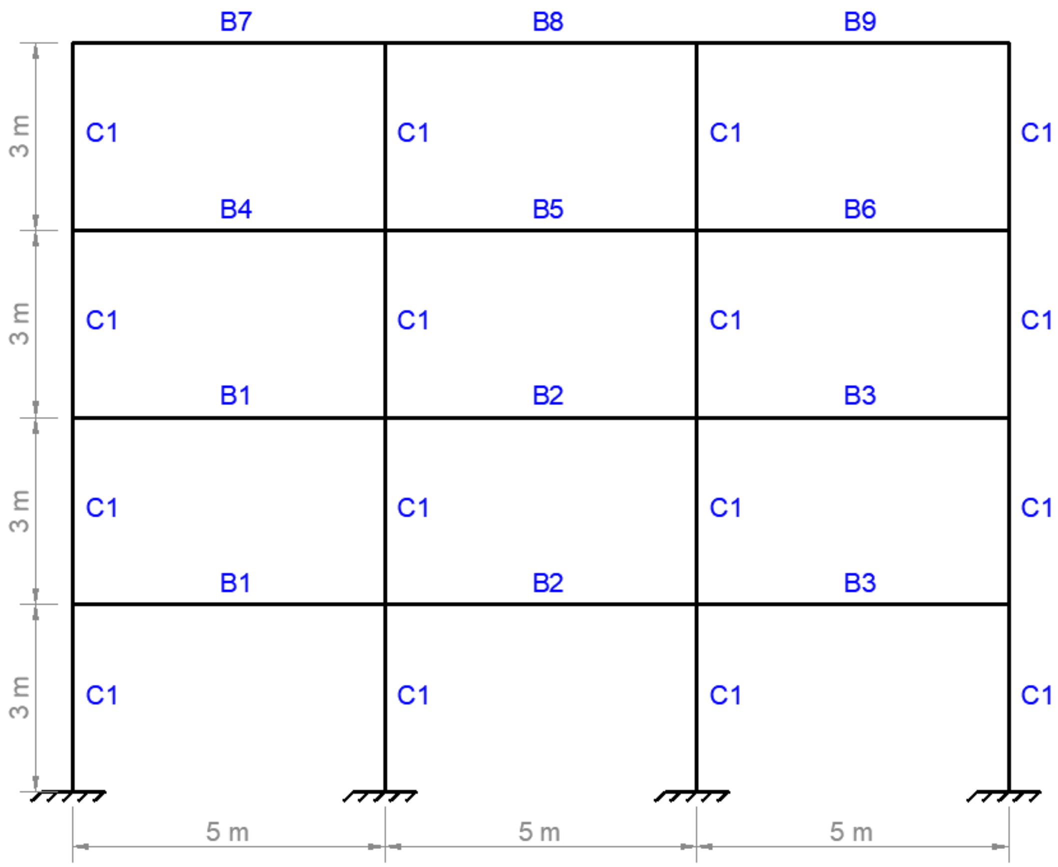

Figure 4.2. Cross-Sectional View of Frame F4S3B

Table 4.3. *Sectional properties of Frame F4S3B*

Structural Member	Width (mm)	Depth (mm)	Clear Cover (mm)	Total Reinforcing Rebar Area (mm^2)	
Column C1	500	500	50	2500.0	
Beam B1	250	550	50	803.0 (top)	432.0 (bottom)
Beam B2	250	550	50	761.0 (top)	432.0 (bottom)
Beam B3	250	550	50	797.0 (top)	432.0 (bottom)
Beam B4	250	550	50	648.5 (top)	416.0 (bottom)
Beam B5	250	550	50	632.0 (top)	406.0 (bottom)
Beam B6	250	550	50	642.0 (top)	416.0 (bottom)
Beam B7	250	550	50	445.0 (top)	287.0 (bottom)
Beam B8	250	550	50	445.0 (top)	290.0 (bottom)
Beam B9	250	550	50	445.0 (top)	284.0 (bottom)

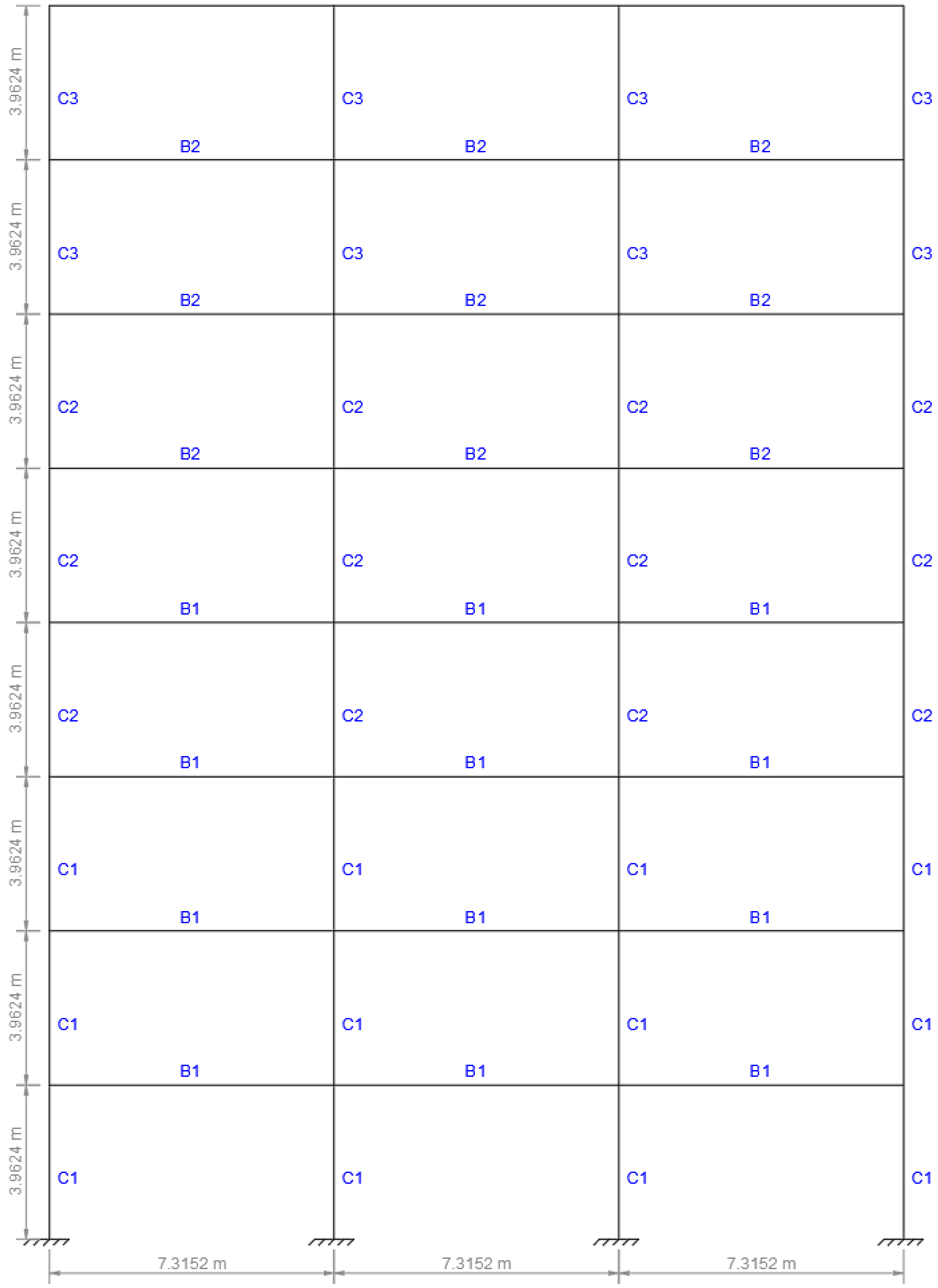

Figure 4.3. Cross-Sectional View of Frame F8S3B

Table 4.4. *Sectional properties of Frame F8S3B*

Structural Member	Width (mm)	Depth (mm)	Clear Cover (mm)	Total Reinforcing Rebar Area (mm^2)	
Column C1	1100	1100	50	18360.0	
Column C2	1000	1000	50	14280.0	
Column C3	920	920	50	10200.0	
Beam B1	500	900	50	5400.0 (top)	4800 (bottom)
Beam B2	400	750	50	4500.0 (top)	3600.0 (bottom)
Beam B3	300	600	50	1800.0 (top)	1125.0 (bottom)

The total number of integration points affects the total response directly, since the numerical integration method is used to determine this response. To get accurate results with less computing time, a single section is divided into sub-sections along its width and length. The graphical representation of this nonlinear fiber-based beam-column element is given in Figure 4.4. The reinforcing steel, confined and unconfined concrete models are also presented in the same figure.

To model confined and unconfined concrete, Kent-Scott-Park concrete model with no tensile strength is preferred which is called as “Concrete01” uniaxial material in OpenSees (Kent and Park, 1971; Scott *et al.*, 1982). A uniaxial Kent-Scott-Park concrete material type with degraded linear unloading/reloading stiffness is constructed by this model (Karsan-Jirsa, 1969). The input parameters for the model are maximum concrete strains and crushing strengths, the 28-day compressive strength, and crushing strength. The material properties of the concrete are presented in Table 4.5 for the selected three frames.

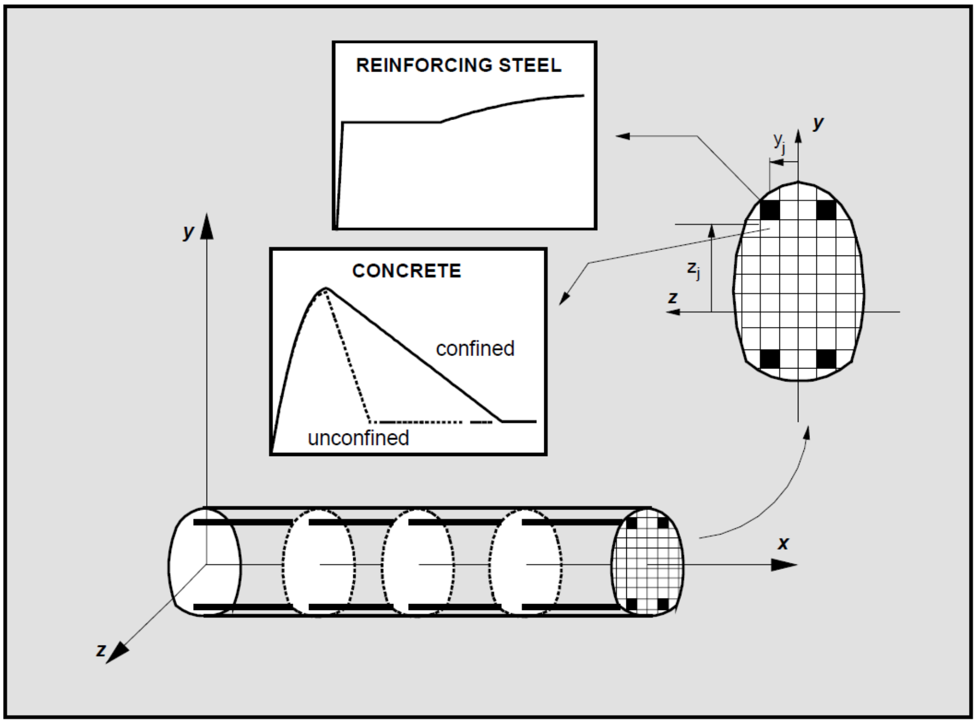

Figure 4.4. The graphical representation of the distribution of control sections and section sub-division into a nonlinear fiber-based beam-column element (Taucer et al., 1991)

To model reinforcing steel in OpenSees, "Steel01" uniaxial material, a uniaxial bilinear model with kinematic hardening, is used. The properties of the reinforcing steel are presented in Table 4.6 for both frames. The strain hardening and initial elastic tangent, E, are selected based on the study of Kadaş (2006).

The frames are modeled numerically by OpenSees platform via the finite element method for spatial discretization. Since the selected frames are symmetric, the models are prepared in two-dimensions only.

The comparisons are done in terms of maximum storey displacements and the results are presented in Section 4.3.1, 4.3.2 and 4.3.3 for three frames separately.

Table 4.5. *Material properties of the concrete*

Frame ID	Type of Concrete	Section	f_c (MPa)	ε_{c0}	f_{cu} (MPa)	ε_{cu}
F3S2B	Unconfined concrete properties	All sections	18.5714	0.0020	0.0007	0.0057
	Confined concrete properties	Beams	21.8014	0.0024	4.3643	0.0180
		Columns	23.8729	0.0026	4.7743	0.0450
F4S3B	Unconfined concrete properties	All sections	20.0000	0.0020	4.0000	0.0063
	Confined concrete properties	Beams	25.8742	0.0025	4.0000	0.0279
		Columns	26.3842	0.0026	4.0000	0.0063
F8S3B	Unconfined concrete properties	All sections	28.0000	0.0020	0.0010	0.0054
	Confined concrete properties	B1	30.7040	0.0022	6.1410	0.0190
		B2	31.5130	0.0023	6.3030	0.0200
		B3	33.0470	0.0024	6.6090	0.0230
		C1	33.8800	0.0024	6.7760	0.0530
		C2	35.0080	0.0025	7.0020	0.0590
		C3	38.3670	0.0027	7.6730	0.0820

Table 4.6. *Material properties of the reinforcing steel*

Frame ID	Section	f_y (MPa)	f_{yw} (MPa)	Hardening ratio	E (GPa)
F3S2B	All sections	494	494	0.005	200
F4S3B	All sections	459	459	0.005	200
F8S3B	All sections	420	420	0.005	200

4.3.1. Results of Frame F3S2B

The maximum storey displacements from the real records and simulation results are calculated for frame F3S2B. Table 4.7 presents the maximum storey displacements in E-W and N-S directions separately, and the geometric mean of both E-W and N-S components at each storey level and station. In addition, the distribution of maximum storey displacements due to real and broadband simulation records of the 1999 Duzce earthquake for F3S2B is given in Figure 4.5.

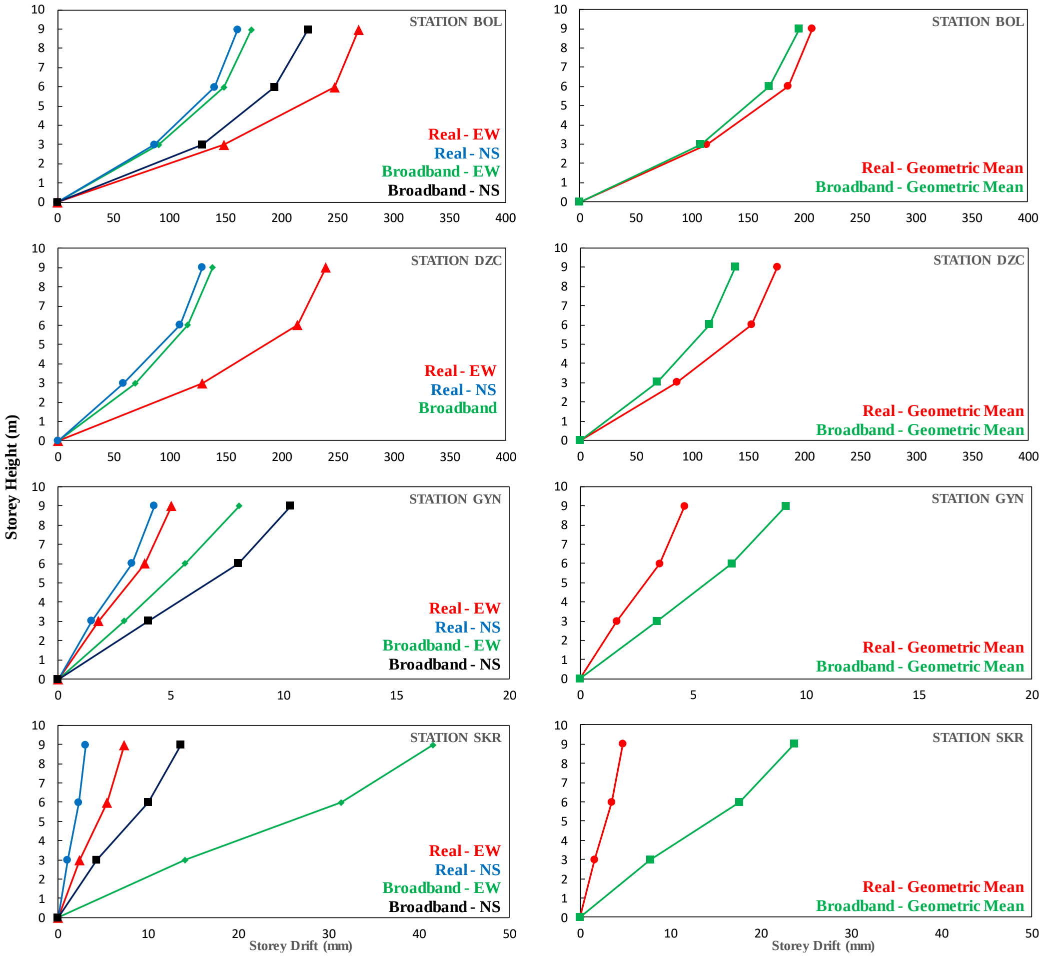

Figure 4.5. Distribution of maximum storey displacements due to real and broadband simulation records of the 1999 Duzce earthquake – F3S2B

Table 4.7. *Maximum storey displacement from real and simulated records at all stations for F3S2B*

Station	Storeys	EW DIRECTION Real Storey Displacement	EW DIRECTION Synthetic Storey Displacement	EW DIRECTION Synthetic / Real Ratio	NS DIRECTION Real Storey Displacement	NS DIRECTION Synthetic Storey Displacement	NS DIRECTION Synthetic / Real Ratio	GEOMETRIC MEAN Real Storey Displacement	GEOMETRIC MEAN Synthetic Storey Displacement	GEOMETRIC MEAN Synthetic / Real Ratio	GEOMETRIC MEAN Stochastic Storey Displacement	GEOMETRIC MEAN Stochastic / Real Ratio
Station BOL	Storey 1	148.82 mm	90.67 mm	0.61	86.89 mm	129.80 mm	1.49	113.72 mm	108.48 mm	0.95	14.59 mm	0.13
	Storey 2	247.27 mm	148.80 mm	0.60	140.39 mm	193.51 mm	1.38	186.32 mm	169.69 mm	0.91	29.78 mm	0.16
	Storey 3	268.99 mm	173.01 mm	0.64	161.02 mm	223.84 mm	1.39	208.12 mm	196.79 mm	**0.95**	38.34 mm	0.18
Station DZC	Storey 1	129.00 mm	68.99 mm	0.53	58.26 mm	68.99 mm	1.18	86.69 mm	68.99 mm	0.80	68.99 mm	0.80
	Storey 2	214.11 mm	115.62 mm	0.54	109.45 mm	115.62 mm	1.06	153.08 mm	115.62 mm	0.76	115.62 mm	0.76
	Storey 3	239.17 mm	138.47 mm	0.58	129.14 mm	138.47 mm	1.07	175.75 mm	138.47 mm	**0.79**	138.47 mm	0.79
Station GYN	Storey 1	1.79 mm	2.93 mm	1.64	1.49 mm	3.99 mm	2.69	1.63 mm	3.42 mm	2.10	3.80 mm	2.33
	Storey 2	3.84 mm	5.65 mm	1.47	3.27 mm	8.02 mm	2.45	3.54 mm	6.73 mm	1.90	8.23 mm	2.32
	Storey 3	5.02 mm	8.02 mm	1.60	4.28 mm	10.33 mm	2.42	4.63 mm	9.10 mm	**1.96**	10.63 mm	2.29
Station SKR	Storey 1	2.39 mm	14.15 mm	5.92	1.05 mm	4.29 mm	4.11	1.58 mm	7.79 mm	4.93	7.65 mm	4.84
	Storey 2	5.41 mm	31.39 mm	5.80	2.30 mm	9.99 mm	4.34	3.53 mm	17.71 mm	5.02	16.66 mm	4.72
	Storey 3	7.34 mm	41.58 mm	5.67	3.07 mm	13.60 mm	4.42	4.75 mm	23.78 mm	**5.01**	22.13 mm	4.66

4.3.2. Results of Frame F4S3B

Similar to F3S2B, the results of frame F4S3B are given in Table 4.8 in E-W and N-S directions separately, and the geometric mean of both E-W and N-S components at each storey level and station. In addition, the distribution of maximum storey displacements due to real and broadband simulation records of the 1999 Duzce earthquake for F4S3B is given in Figure 4.6.

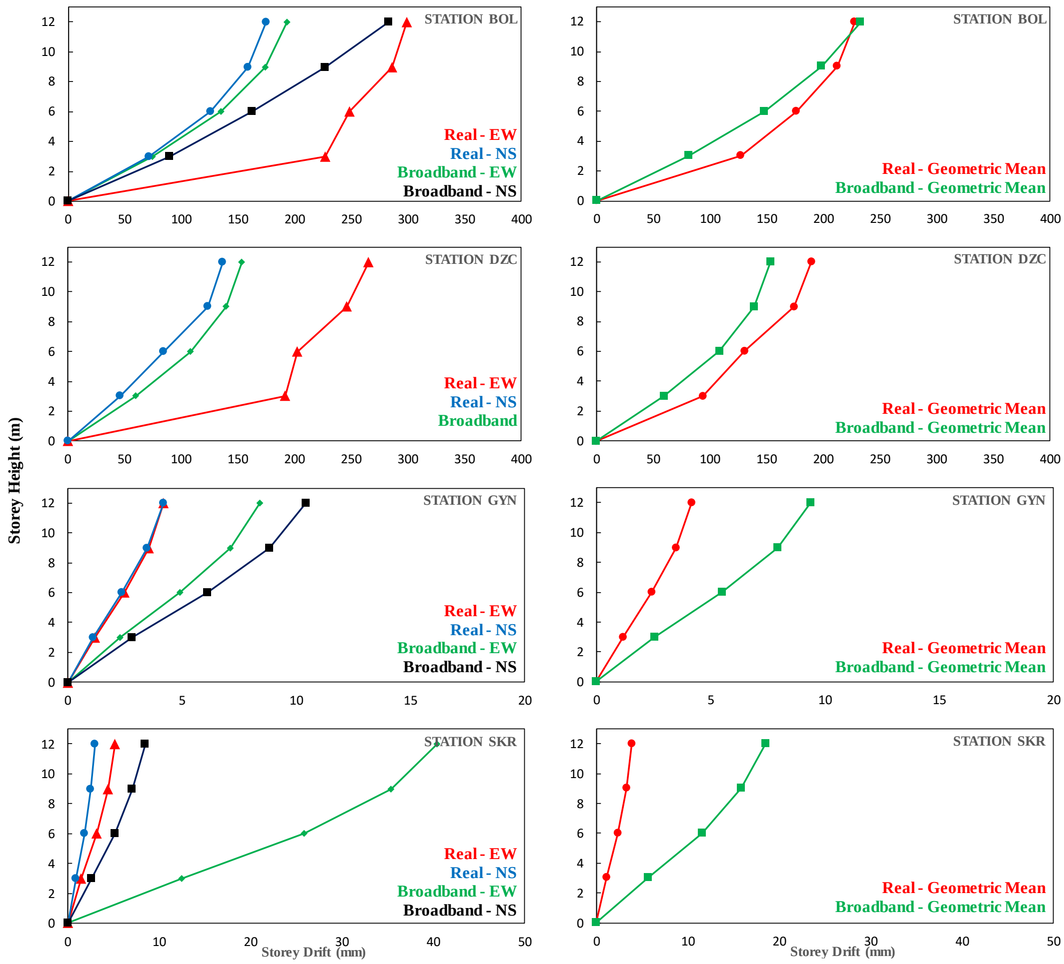

Figure 4.6. Distribution of maximum storey displacements due to real and broadband simulation records of the 1999 Duzce earthquake – F4S3B

Table 4.8. *Maximum storey displacement from real and simulated records at all stations for F4S3B*

		EW DIRECTION			NS DIRECTION			GEOMETRIC MEAN				
	Storeys	**Real Storey Displacement**	**Synthetic Storey Displacement**	**Synthetic / Real Ratio**	**Real Storey Displacement**	**Synthetic Storey Displacement**	**Synthetic / Real Ratio**	**Real Storey Displacement**	**Synthetic Storey Displacement**	**Synthetic / Real Ratio**	**Stochastic Storey Displacement**	**Stochastic / Real Ratio**
Station BOL	Storey 1	226.56 mm	74.35 mm	0.33	71.43 mm	90.00 mm	1.26	127.21 mm	81.81 mm	0.64	9.88 mm	0.08
	Storey 2	248.18 mm	134.82 mm	0.54	125.79 mm	162.59 mm	1.29	176.69 mm	148.05 mm	0.84	20.30 mm	0.11
	Storey 3	285.90 mm	174.13 mm	0.61	158.25 mm	226.70 mm	1.43	212.71 mm	198.68 mm	0.93	27.31 mm	0.13
	Storey 4	298.85 mm	193.05 mm	0.65	174.33 mm	282.57 mm	1.62	228.25 mm	233.56 mm	**1.02**	31.07 mm	0.14
Station DZC	Storey 1	191.73 mm	59.81 mm	0.31	46.24 mm	59.81 mm	1.29	94.16 mm	59.81 mm	0.64	59.81 mm	0.64
	Storey 2	202.54 mm	108.57 mm	0.54	84.63 mm	108.57 mm	1.28	130.93 mm	108.57 mm	0.83	108.57 mm	0.83
	Storey 3	245.95 mm	139.34 mm	0.57	123.63 mm	139.34 mm	1.13	174.37 mm	139.34 mm	0.80	139.34 mm	0.80
	Storey 4	265.35 mm	153.61 mm	0.58	136.33 mm	153.61 mm	1.13	190.20 mm	153.61 mm	**0.81**	153.61 mm	0.81
Station GYN	Storey 1	1.20 mm	2.28 mm	1.90	1.13 mm	2.81 mm	2.48	1.17 mm	2.53 mm	2.17	2.86 mm	2.45
	Storey 2	2.48 mm	4.92 mm	1.98	2.39 mm	6.12 mm	2.56	2.43 mm	5.48 mm	2.25	6.03 mm	2.48
	Storey 3	3.53 mm	7.13 mm	2.02	3.48 mm	8.84 mm	2.54	3.50 mm	7.94 mm	2.27	8.82 mm	2.52
	Storey 4	4.18 mm	8.42 mm	2.01	4.17 mm	10.41 mm	2.49	4.18 mm	9.36 mm	**2.24**	10.48 mm	2.51
Station SKR	Storey 1	1.50 mm	12.46 mm	8.32	0.87 mm	2.58 mm	2.98	1.14 mm	5.67 mm	4.98	5.03 mm	4.42
	Storey 2	3.12 mm	25.87 mm	8.29	1.79 mm	5.17 mm	2.89	2.36 mm	11.56 mm	4.90	10.21 mm	4.33
	Storey 3	4.41 mm	35.39 mm	8.02	2.53 mm	7.09 mm	2.80	3.34 mm	15.84 mm	4.73	13.79 mm	4.12
	Storey 4	5.19 mm	40.40 mm	7.79	2.94 mm	8.51 mm	2.89	3.91 mm	18.55 mm	**4.75**	15.65 mm	4.01

4.3.3. Results of Frame F8S3B

Lastly, the results of frame F8S3B are given in Table 4.9 in E-W and N-S directions separately, and the geometric mean of both E-W and N-S components at each storey level and station. In addition, the distribution of maximum storey displacements due to real and broadband simulation records of the 1999 Duzce earthquake for F8S3B is given in Figure 4.7.

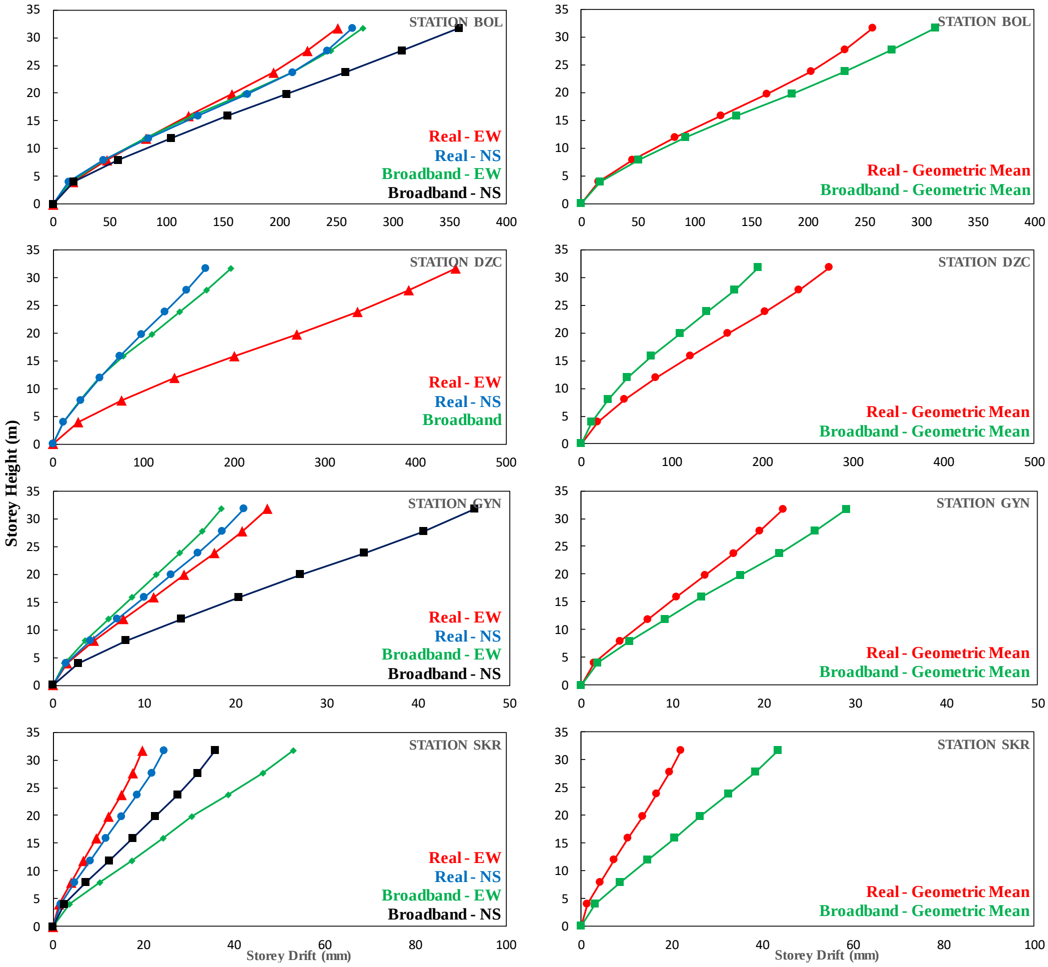

Figure 4.7. Distribution of maximum storey displacements due to real and broadband simulation records of the 1999 Duzce earthquake – F8S3B

Table 4.9. *Maximum storey displacement from real and simulated records at all stations for F8S3B*

		EW DIRECTION			NS DIRECTION			GEOMETRIC MEAN				
	Storeys	**Real Storey Displacement**	**Synthetic Storey Displacement**	**Synthetic / Real Ratio**	**Real Storey Displacement**	**Synthetic Storey Displacement**	**Synthetic / Real Ratio**	**Real Storey Displacement**	**Synthetic Storey Displacement**	**Synthetic / Real Ratio**	**Stochastic Storey Displacement**	**Stochastic / Real Ratio**
Station BOL	Storey 1	17.28 mm	15.62 mm	0.90	13.52 mm	18.44 mm	1.36	15.28 mm	16.97 mm	1.11	5.79 mm	0.38
	Storey 2	47.02 mm	44.80 mm	0.95	44.26 mm	57.16 mm	1.29	45.62 mm	50.61 mm	1.11	15.66 mm	0.34
	Storey 3	81.38 mm	80.81 mm	0.99	83.76 mm	103.93 mm	1.24	82.56 mm	91.65 mm	1.11	27.66 mm	0.34
	Storey 4	118.92 mm	122.80 mm	1.03	127.36 mm	154.03 mm	1.21	123.07 mm	137.53 mm	1.12	40.49 mm	0.33
	Storey 5	157.79 mm	168.20 mm	1.07	171.11 mm	205.71 mm	1.20	164.31 mm	186.01 mm	1.13	54.65 mm	0.33
	Storey 6	194.50 mm	210.98 mm	1.08	211.42 mm	257.99 mm	1.22	202.78 mm	233.30 mm	1.15	68.87 mm	0.34
	Storey 7	223.91 mm	244.98 mm	1.09	241.74 mm	307.80 mm	1.27	232.65 mm	274.60 mm	1.18	80.98 mm	0.35
	Storey 8	250.98 mm	273.47 mm	1.09	263.82 mm	358.39 mm	1.36	257.32 mm	313.06 mm	**1.22**	91.46 mm	**0.36**
Station DZC	Storey 1	28.09 mm	11.47 mm	0.41	11.64 mm	11.47 mm	0.99	18.08 mm	11.47 mm	0.63	11.47 mm	0.63
	Storey 2	75.96 mm	29.74 mm	0.39	30.95 mm	29.74 mm	0.96	48.48 mm	29.74 mm	0.61	29.74 mm	0.61
	Storey 3	134.14 mm	50.87 mm	0.38	51.60 mm	50.87 mm	0.99	83.20 mm	50.87 mm	0.61	50.87 mm	0.61
	Storey 4	200.21 mm	77.93 mm	0.39	73.57 mm	77.93 mm	1.06	121.36 mm	77.93 mm	0.64	77.93 mm	0.64
	Storey 5	269.55 mm	109.40 mm	0.41	97.57 mm	109.40 mm	1.12	162.17 mm	109.40 mm	0.67	109.40 mm	0.67
	Storey 6	335.79 mm	139.70 mm	0.42	123.29 mm	139.70 mm	1.13	203.47 mm	139.70 mm	0.69	139.70 mm	0.69
	Storey 7	392.47 mm	169.60 mm	0.43	147.24 mm	169.60 mm	1.15	240.39 mm	169.60 mm	0.71	169.60 mm	0.71
	Storey 8	444.03 mm	195.99 mm	0.44	168.97 mm	195.99 mm	1.16	273.91 mm	195.99 mm	**0.72**	195.99 mm	**0.72**
Station GYN	Storey 1	1.55 mm	1.24 mm	0.80	1.43 mm	2.74 mm	1.92	1.49 mm	1.84 mm	1.24	2.24 mm	1.51
	Storey 2	4.47 mm	3.54 mm	0.79	4.10 mm	8.02 mm	1.96	4.28 mm	5.33 mm	1.24	6.33 mm	1.48
	Storey 3	7.70 mm	6.08 mm	0.79	7.02 mm	14.02 mm	2.00	7.35 mm	9.23 mm	1.26	10.67 mm	1.45
	Storey 4	10.98 mm	8.66 mm	0.79	9.97 mm	20.35 mm	2.04	10.46 mm	13.27 mm	1.27	14.85 mm	1.42
	Storey 5	14.32 mm	11.26 mm	0.79	12.91 mm	27.13 mm	2.10	13.60 mm	17.48 mm	1.29	19.01 mm	1.40
	Storey 6	17.68 mm	13.90 mm	0.79	15.84 mm	34.16 mm	2.16	16.73 mm	21.79 mm	1.30	23.70 mm	1.42
	Storey 7	20.75 mm	16.31 mm	0.79	18.50 mm	40.58 mm	2.19	19.59 mm	25.73 mm	1.31	27.95 mm	1.43
	Storey 8	23.44 mm	18.40 mm	0.79	20.94 mm	46.18 mm	2.21	22.15 mm	29.15 mm	**1.32**	31.65 mm	**1.43**
Station SKR	Storey 1	1.37 mm	3.66 mm	2.67	1.65 mm	2.56 mm	1.55	1.50 mm	3.06 mm	2.03	4.45 mm	2.95
	Storey 2	3.93 mm	10.38 mm	2.64	4.74 mm	7.32 mm	1.54	4.31 mm	8.72 mm	2.02	12.90 mm	2.99
	Storey 3	6.72 mm	17.49 mm	2.60	8.14 mm	12.50 mm	1.53	7.40 mm	14.78 mm	2.00	22.31 mm	3.02
	Storey 4	9.52 mm	24.26 mm	2.55	11.59 mm	17.63 mm	1.52	10.50 mm	20.68 mm	1.97	32.31 mm	3.08
	Storey 5	12.30 mm	30.62 mm	2.49	15.08 mm	22.69 mm	1.50	13.62 mm	26.36 mm	1.93	43.23 mm	3.17
	Storey 6	15.06 mm	38.72 mm	2.57	18.59 mm	27.65 mm	1.49	16.74 mm	32.72 mm	1.96	54.64 mm	3.27
	Storey 7	17.57 mm	46.30 mm	2.64	21.77 mm	32.02 mm	1.47	19.55 mm	38.50 mm	1.97	65.05 mm	3.33
	Storey 8	19.80 mm	53.14 mm	2.68	24.53 mm	35.76 mm	1.46	22.04 mm	43.59 mm	**1.98**	74.18 mm	**3.37**

4.4. Comparison of Results

The results presented in Table 4.7 - 4.9 reveal that the simulated motions provide close responses to the corresponding real ones. The comparisons in detail are summarizes as:

- Overall, for all stations except SKR a good match is obtained in between the real and estimated dynamic responses in terms of maximum top story displacements.

- The geometric means for station BOL as well as station DZC in N-S direction, an almost perfect match is observed in between the real and simulated responses. This is because the simulated acceleration-time history is close to real.

- At station SKR, the factor of overestimation is over 5 for F3S2B and F4S3B, and over 2 for F8S3B in low periods. This can be attributed to the discrepancies observed between the real and simulated FAS at this station.

- Finally, it is concluded that when the simulated records are acceptable seismologically (for instance: Smaller misfits are obtained in terms of FAS as shown herein), the simulated structural responses are also satisfactory.

CHAPTER 5

SUMMARY AND CONCLUSIONS

5.1. Summary

This thesis presents broadband ground motion simulations and nonlinear building response simulations with real and simulated records of 12 November 1999 Duzce earthquake. The main objectives of this thesis are to study ground motion simulations and building response simulations in a broadband frequency range and to compare the results with stochastic simulations of the same earthquake which is studied previously (Ugurhan and Askan, 2010; Karimzadeh *et al.*, 2017a). A broadband simulation platform is built by combining low and high frequency ground motion simulation approaches.

A total of four stations (DZC, BOL, GYN, and SKR) are selected within a Joyner and Boore distance less than 50 km from the fault plane of the 1999 Duzce earthquake. To evaluate the accuracy of the simulated motions, both seismological and structural measures are used. Real and simulated ground motions are first compared in terms of FAS, RS, PGA and PGV misfits. The results from the broadband simulations are then compared to the results from a previous study that employed only stochastic method for the entire frequency band ($0\ Hz < f < 10\ Hz$). The spatial distribution of the simulated PGA and PGV values are obtained within the selected study area for a set of scenario events. Next, the simulated peak ground motion values are compared against selected local and global GMPE's for verification purposes. Finally, the efficiency of the simulated motions is evaluated in terms of nonlinear dynamic structural responses against the corresponding real values for the typical RC frames.

5.2. Conclusions

The main findings and conclusions derived in this thesis are given as follows:

- The local input parameters of the ground motion simulations, such as quality factor, kappa, site model and velocity model must be carefully selected to get reliable simulations.

- The importance of hybrid ground motion simulations is that broadband frequency range covers the required structural frequency range by combining low and high frequencies.

- The improvement of broadband simulations over only-stochastic ones is obvious in terms of PGA, PGV, FSA and RS misfits.

- The structural aspects of three multi degree of freedom models are investigated similar to a previous study (Karimzadeh *et al.*, 2017b). It is observed that the structural misfits also decreased similar to the seismological misfits when compared to the only-stochastic previous models (Karimzadeh *et al.*, 2017b).

- For the very near-field stations, the deterministic approach cannot effectively simulate the ground motions (e.g.: Station DZC). This is most probably due to the horizontal constraints of the low frequency simulation algorithm.

- A close match in between the simulated peak values and the corresponding values obtained from the GMPE's reveals the use of a physically reasonable source, propagation, and site modeling despite the existing uncertainties.

- In building response simulation, it is noticed that the simulated results improve in over long periods (low frequencies). High-rise buildings give more reliable misfits than low-rise ones. This is most probably due to the scattering in high frequencies compared to the more deterministic low frequencies.

- The numerical results obtained in this study suggest that the use of simulated broadband ground motions for earthquake engineering purposes is promising.

5.3. Assumptions of the Present Study and Future Recommendations

Several assumptions are made in this study, which need to be further investigated in future studies. The related recommendations are given as follows:

- It is very important to study broadband ground motion simulations in regions with different seismotectonic regions. Such a study will augment the conclusions of this thesis.

- With better assessment of velocity models, for example, a 3D model instead of a 1D model, it is possible to have more accurate results in simulations.

- With detailed modeling and extensive field works, more realistic regional parameters such as kappa, quality factor, and site amplifications can be obtained. Such regional models directly increase the accuracy of ground motion simulations.

- To generalize the conclusions for nonlinear response analysis, other building types with different geometry and periods can be studied under real versus simulated ground motions.

REFERENCES

Aki, K. (1957). Space and time spectra of stationary stochastic waves with special reference to microtremors. *Bulletin of the Earthquake Research Institute*, **35(3)**, 415–457.

Aki, K. (1967). Scaling law of seismic spectrum. *Journal of Geophysical Research*, **72(4)**, 1217–1231.

Aki, K. and P. G. Richards (1980). Quantitative Seismology: Theory and methods. Vol Ⅱ, W. H. Freeman and Co., San Francisco, 932 pp.

Akinci, A. and A. Antonioli (2013). Observations and stochastic modelling of strong ground motions for the 2011 October 23 M_w 7.1 Van, Turkey, earthquake. *Geophysical Journal International*, **192(3)**, 1217–1239.

Akkar, S. and J. J. Bommer (2007). Empirical prediction equations for peak ground velocity derived from strong–motion records from Europe and the Middle East. *Bulletin of the Seismological Society of America*, **97(2)**, 511–530, doi: 10.1785/0120060141.

Akkar, S. and Z. Cagnan (2010). A local ground motion predictive model for Turkey and its comparison with other regional and global ground–motion models. *Bulletin of the Seismological Society of America*, **100(6)**, 2978–2995, doi: 10.1785/0120090367.

Akyüz, H. S., Hartleb, R., Barka, A., Altunel, E., Sunal, G., Meyer, B. and R. Armijo (2002). Surface rupture and slip distribution of the 12 November 1999 Düzce Earthquake (M 7.1), North Anatolian Fault, Bolu, Turkey. *Bulletin of the Seismological Society of America*, **92(1)**, 61–66, doi: 10.1785/0120000840.

Ameri, G., Emolo, A., Pacor, F. and F. Gallovič (2011). Ground–motion simulations for the 1980 M 6.9 Irpinia Earthquake (Southern Italy) and scenario events. *Bulletin of the Seismological Society of America*, **101(3)**, 1136–1151, doi: 10.1785/0120100231.

Ameri, G., Pacor, F., Cultrera, G. and G. Franceschina (2008). Deterministic ground–motion scenarios for engineering applications: The case of Thessaloniki, Greece. *Bulletin of the Seismological Society of America*, **98(3)**, 1289–1303, doi: 10.1785/0120070114.

Anderson, J. G. and S. E. Hough (1984). A model for the shape of the Fourier amplitude spectrum of at high frequencies. *Bulletin of the Seismological Society of America*, **74(5)**, 1969–1993.

Ansal, A., Akinci, A., Cultrera, G., Erdik, M., Pessina, V., Tönük, G. and G. Ameri (2009). Loss estimation in Istanbul based on deterministic earthquake scenarios of the Marmara Sea region (Turkey). *Soil Dynamics and Earthquake Engineering*, **29(4)**, 699–709, doi: 10.1016/j.soildyn.2008.07.006.

Askan, A., Sisman, F. N. and B. Ugurhan (2013). Stochastic strong ground motion simulations in sparsely–monitored regions: A validation and sensitivity study on the 13 March 1992 Erzincan (Turkey) earthquake. *Soil Dynamics and Earthquake Engineering*, **55**, 170–181, doi: 10.1016/j.soildyn.2013.09.014.

Asten, M. W., Askan, A., Ekincioglu, E. E., Sisman, F. N. and B. Ugurhan (2014). Site characterisation in north–western Turkey based on SPAC and HVSR analysis of microtremor noise. *Exploration Geophysics*, **45(2)**, 74–85, doi: 10.1071/EG12026.

Asten, M. W., Dhu, T., Jones, A. and T. Jones (2003). Comparison of shear velocities measured from microtremor array studies and SCPT data acquired for earthquake site hazard classification in the northern suburbs of Perth W.A. *Proceedings of a Conference of the Australian Earthquake Engineering Soc.*, 12 p., Melbourne.

Atkinson, G. M. (1984). Attenuation of strong ground motion in Canada from a random vibrations approach. *Bulletin of the Seismological Society of America*, **74(6)**, 2629–2653.

Atkinson, G. M. (2004). Empirical attenuation of ground–motion spectral amplitudes in southeastern Canada and the northeastern United States. *Bulletin of the*

Seismological Society of America, **94(3)**, 1079–1095, doi: 10.1785/0120030175.

Atkinson, G. M. and D. M. Boore (1995). Ground–motion relations for eastern North America. *Bulletin of the Seismological Society of America*, **85(1)**, 17–30.

Atkinson, G. M. and W. Silva (2000). Stochastic modeling of California ground motions. *Bulletin of the Seismological Society of America*, **90(2)**, 255–274, doi: 10.1785/0119990064

Atkinson, G. M., Assatourians, K., Boore, D. M., Campbell, K. and D. Motazedian (2009). A guide to differences between stochastic point–source and stochastic finite–fault simulations. *Bulletin of the Seismological Society of America*, **99(6)**, 3192–3201, doi: 10.1785/0120090058.

Bao, H., Bielak, J., Ghattas, O., Kallivokas, L. F., O'Hallaron, D. R., Schewchuk, J. R., and J. Xu (1998). Large–scale simulation of elastic wave propagation in heterogeneous media on parallel computers. *Computer Methods in Applied Mechanics and Engineering*, **152(1–2)**, 85–102, doi: 10.1016/S0045-7825(97)00183-7.

Baykal, M, Miyake, H., and T. Yokoi (2012). Source model of the 2010 Elazığ Kovancılar Earthquake (M_w 6.1) for broadband ground motion simulation. *Proceedings of the 15th World Conference on Earthquake Engineering*, 10 p., Lisbon.

Beresnev, I. A., and G. M. Atkinson (1997). Modeling finite–fault radiation from the ω^n spectrum. *Bulletin of the Seismological Society of America*, **87(1)**, 67–84.

Beresnev, I. A., and G. M. Atkinson (1998). FINSIM–a FORTRAN program for simulating stochastic acceleration time histories from finite faults. *Seismological Research Letters*, **69(1)**, 27–32, doi: 10.1785/gssrl.69.1.27.

Birgören, G., Sekiguchi, H., and K. Irikura (2004). Rupture model of the 1999 Düzce, Turkey, earthquake deduced from high and low frequency strong motion data. *Geophysical Research Letters*, **31(5)**, L05610, doi: 10.1029/2003GL019194.

Boore, D. M. (1983). Stochastic simulation of high–frequency ground motions based on seismological models of the radiated spectra. *Bulletin of the Seismological Society of America*, **73(6)**, 1865–1894.

Boore, D. M. (1984). Use of seismoscope records to determine M_L and peak velocities. *Bulletin of the Seismological Society of America*, **74(1)**, 315–324.

Boore, D. M. (2003). Simulation of ground motion using the stochastic method. *Pure and Applied Geophysics*, **160**, 635–675.

Boore, D. M. (2013). The uses and limitations of the square–root impedance method for computing site amplification. *Bulletin of the Seismological Society of America*, **103(4)**, 2356–2368, doi: 10.1785/0120120283.

Boore, D. M. and G. M. Atkinson (1987). Stochastic prediction of ground motion and spectral response parameters at hard–rock sites in eastern North America. *Bulletin of the Seismological Society of America*, **77(2)**, 440–467.

Boore, D. M. and G. M. Atkinson (2008). Ground–motion prediction equations for the average horizontal component of PGA, PGV, and 5%–damped PSA at spectral periods between 0.01 s and 10.0 s. *Earthquake Spectra*, **24(1)**, 99–138, doi: 10.1193/1.2830434.

Boore, D. M. and W. B. Joyner (1997). Site amplifications for generic rock sites. *Bulletin of the Seismological Society of America*, **87(2)**, 327–341.

Boore, D. M., Joyner, W. B. and T. E. Fumal (1993). Estimation of response spectra and peak accelerations from western North American earthquakes. *An interim report. U.S. Geological Survey Open–File Report*, 93–509, 72 pp.

Bouchon, M. (1981). A simple method to calculate Green's functions for elastic layered media. *Bulletin of the Seismological Society of America*, **71(4)**, 959 – 971.

Bouin, M. P., Bouchon, M., Karabulut, H. and M. Aktar (2004). Rupture process of the 1999 November 12 Düzce (Turkey) earthquake deduced from strong motion and Global Positioning System measurements. *Geophysical Journal International*, **159(1)**, 207–211, doi: 10.1111/j.1365-246X.2004.02367.x.

Brune, J. N. (1970). Tectonic stress and the spectra of seismic shear waves from earthquakes. *Journal of Geophysical Research*, **75(26)**, 4997–5009, doi: 10.1029/JB075i026p04997.

Brune, J. N. (1971). Seismic sources, fault plane studies and tectonics. *EOS, Transactions American Geophysical Union*, **52(5)**, 178–187, doi: 10.1029/EO052i005pIU178.

Bulut, F., Bohnhoff, M., Aktar, M., and G. Dresen (2007). Characterization of aftershock–fault plane orientations of 1999 Izmit (Turkey) earthquake using high–resolution aftershock locations. *Geophysical Research Letters*, **34(20)**, doi: 10.1029/2007GL031154.

Bürgmann, R., Ergintav, S., Segall, P., Hearn, E. H., McClusky, S., Reilinger, R. E., Woith, H. and J. Zschau (2002). Time–dependent afterslip on and deep below the Izmit Earthquake rupture. *Bulletin of the Seismological Society of America*, **92(1)**, 126–137, doi: 10.1785/0120000833.

Cakir, Z., Barka, A., Chabalier, J. B., Armijo, A., and B. Meyer (2003). Kinematics of the November 12, 1999 (M_W=7.2) Duzce earthquake from SAR interferometry. *Turkish Journal of Earth Sciences*, **12**, 105–118.

Castro, R. R., Pacor, F., Franceschina, G., Bindi, D., Zonno, G., and L. Luzi (2008). Stochastic strong–motion simulation of the Umbria– Marche earthquake of September 1997 (Mw 6): Comparison of different approaches. *Bulletin of the Seismological Society of America*, **98(2)**, 662–670, doi: 10.1785/0120070092.

Castro, R. R., Rovelli, A., Cocco, M., Di Bona, M. and F. Pacor (2001). Stochastic simulation of strong-motion records from the 26 September 1997 (Mw 6), Umbria-Marche (Central Italy) earthquake. *Bulletin of the Seismological Society of America*, **91**, 27–39, doi: 10.1785/0120000011.

Chen, X. and H. Zhang (2001). An efficient method for computing Green's functions for a layered half–space at large epicentral distances. *Bulletin of the Seismological Society of America*, **91(4)**, 858–869, doi: 10.1785/0120000113.

Cohen, G., Joly, P., and N. Tordjman (1993). Construction and analysis of higher–order finite elements with mass lumping for the wave equation. Kleinman R. (Ed.), in Proceedings of the Second International Conference on Mathematical and Numerical Aspects of Wave Propagation, SIAM, Philadelphia, Pennsylvania, 152– 160.

Delouis, B., Lundgren, P. and D. Giardini (2004). Slip distributions of the 1999 Düzce (M_W=7.2) and Izmit (M_W=7.6) earthquakes on the North Anatolian Fault (Turkey): A combined analysis. I*nternal report*.

EXSIM. A FORTRAN program for simulating stochastic acceleration time histories from finite–faults with a dynamic corner frequency approach. http://www.daveboore.com/software_online.html, [last visited on December 2015].

Frankel, A. (1993). Three–dimensional simulations of the ground motions in the San Bernardino Valley, California, for hypothetical earthquakes on the San Andreas Fault. *Bulletin of the Seismological Society of America*, **83(4)**, 1020–1041.

Frankel, A. and J. Vidale (1992). A three–dimensional simulation of seismic waves in the Santa Clara Valley, California, from a Loma Prieta aftershock. *Bulletin of the Seismological Society of America*, **82(5)**, 2045–2074.

Galluzzo, D., Zonno, G. and E. Del Pezzo (2008). Stochastic finite–fault ground–motion simulation in a wave–field diffusive regime: Case study of the Mt. Vesuvius volcanic area. *Bulletin of the Seismological Society of America*, **98(3)**, 1272–1288, doi: 10.1785/0120070183.

Hanks, T. C. (1982). fmax. *Bulletin of the Seismological Society of America*, **72(6A)**, 1867–1879.

Hanks, T. C. and D. M. Boore (1984). Moment–magnitude relations in theory and practice. *Journal of Geophysical Research*, **89(B7)**, 6229–6235, doi: 10.1029/JB089iB07p06229.

Hanks, T. C. and H. Kanamori (1979). A moment magnitude scale. *Journal of Geophysical Research*, **84(B5)**, 2348–2350, doi: 10.1029/JB084iB05p02348.

Hanks, T. C. and R. K. McGuire (1981). The character of high–frequency strong ground motion. *Bulletin of the Seismological Society of America*, **71(6)**, 2071–2095.

Hartzell, S. (1978). Earthquake aftershocks as Green's functions. *Geophysical Research Letters*, **5(1)**, 1–4, doi: 10.1029/GL005i001p00001.

Haskell, N. A. (1960). Crustal reflections of plane SH waves. *Journal of Geophysical Research*, **65**, 4147–4150, doi: 10.1029/JZ065i012p04147.

Haskell, N. A. (1964). Total energy and energy spectral density of elastic wave radiation from propagating faults. *Bulletin of the Seismological Society of America*, **54(6A)**, 1811–1841.

Heaton, T. H. (1990). Evidence for and implications of self–healing pulses of slip in earthquake rupture. *Physics of the Earth and Planetary Interiors*, **64(1)**, 1–20, doi: 10.1016/0031-9201(90)90002-F.

Hisada, Y. (1994). An efficient method for computing Green's functions for a layered half–space with sources and receivers at close depths. *Bulletin of the Seismological Society of America*, **84(5)**, 1456–1472.

Hisada, Y. (2008). Broadband strong motion simulation in layered half–space using stochastic Green's function technique. *Journal of Seismology*, **12(2)**, 265–279, doi: 10.1007/s10950-008-9090-6.

Hisada, Y. and J. Bielak (2003). A theoretical method for computing near–fault ground motions in layered half–spaces considering static offset due to surface faulting, with a physical interpretation of fling step and rupture directivity. *Bulletin of the Seismological Society of America*, **93(3)**, 1154–1168, doi: 10.1785/0120020165.

Housner, G. W. (1947). Characteristics of strong–motion earthquakes. *Bulletin of the Seismological Society of America*, **37(1)**, 19–31.

Housner, G. W. (1955). Properties of strong ground motion earthquakes. *Bulletin of the Seismological Society of America*, **45(3)**, 197–218.

Huang, H. and T. Teng (1999). An evaluation on H/V Ratio vs. spectral ratio for site–response estimation using the 1994 Northridge Earthquake sequences. *Pure and Applied Geophysics*, **156(4)**, 631–649, doi: 10.1007/s000240050316.

Irikura, K. (1986). Prediction of strong acceleration motions using empirical Green's function. In Proc. 7th Japan Earthq. Eng. Symp. 151–156, Tokyo, Japan.

Joyner W and T. Fumal (1985). Predictive mapping of earthquake ground motion. Evaluating Earthquake Hazards in the Los Angeles Region. *An Earth Science Perspective*, **1360**, 203–220.

Kadaş K. (2006). Influence of idealized pushover curves on seismic response. MS Thesis, Middle East Technical University, Ankara, Turkey.

Kamae, K., K. Irikura, and A. Pitarka (1998). A technique for simulating strong ground motion using Hybrid Green's function. *Bulletin of the Seismological Society of America*, **88(2)**, 357–367.

Kanamori, H. and D. L. Anderson (1975). Theoretical basis of some empirical relations in seismology. *Bulletin of the Seismological Society of America*, **65(5)**, 1073–1095.

Karimzadeh, S. (2016). Use of simulated strong ground motion records in earthquake engineering applications. Doctoral Thesis, Middle East Technical University, Ankara, Turkey.

Karimzadeh, S., Askan A. and A. Yakut (2017a). Assessment of simulated ground motions in earthquake engineering practice: A case study for Duzce (Turkey). *Pure and Applied Geophysics*, **174(9)**, 3589–3607, doi: 10.1007/s00024-017-1602-2.

Karimzadeh, S., Askan, A., Yakut A. and G. Ameri (2017b). Assessment of simulation techniques in nonlinear time history analyses of multi–story frame buildings: A case study. *Soil Dynamics and Earthquake Engineering*, **98**, 38–53, doi: 10.1016/j.soildyn.2017.04.004.

Karsan I. D. and J. O. Jirsa (1969). Behavior of concrete under compressive loading. *Journal of Structural Division ASCE*, **95(12)**, 2543–2563.

Kawase, H. (1988). Time–domain response of a semi–circular canyon for incident SV, P, and Rayleigh waves calculated by the discrete wavenumber boundary element method. *Bulletin of the Seismological Society of America*, **78(4)**, 1415–1437.

Kennett, B. L. N. (1983). Seismic wave propagation in a stratified half–space. Cambridge University Press, Cambridge.

Kent, D. C. and R. Park (1971). Flexural members with confined concrete. *Journal of the Structural Division*, **97(7)**, 1969–1990.

Komatitsch, D. (1997). Spectral and spectral element methods for the 2D and 3D elastodynamics equations in heterogeneous media. Doctoral Thesis, *Institut de Physique du Globe*, Paris, France.

Komatitsch, D. and J. P. Vilotte (1998). The spectral element method: An efficient tool to simulate the seismic response of 2D and 3D geological structures. *Bulletin of the Seismological Society of America*, **88(2)**, 368–392.

Komatitsch, D. and J. Tromp (1999). Introduction to the spectral element method for 3-D seismic wave propagation. *Geophysical Journal International*, **139(3)**, 806–822, doi: 10.1046/j.1365-246x.1999.00967.x.

Komatitsch, D., Liu, Q., Tromp, J., Süss, P., Stidham, C. and J. Shaw (2004). Simulations of ground motion in the Los Angeles basin based upon the spectral–element method. *Bulletin of the Seismological Society of America*, **94(1)**, 187–206, doi: 10.1785/0120030077.

Konca A., Leprince S., Avouac J. and D. V. Helmberger (2010). Rupture process of the 1999 M_w 7.1 Duzce Earthquake from joint analysis of SPOT, GPS, InSAR, strong–motion, and teleseismic data: A supershear rupture with variable rupture velocity. *Bulletin of the Seismological Society of America*, **100(1)**, 267–288, doi: 10.1785/0120090072.

Kramer, S. L. (1996). Geotechnical Earthquake Engineering, Prentice Hall, Inc., Upper Saddle River, New Jersey, 653 pp.

Lermo, J., and F. J. Chávez–García (1994). Are microtremors useful in site response evaluation? *Bulletin of the Seismological Society of America*, **84(5)**, 1350–1364.

Li, X., J. Bielak, and O. Ghattas (1992). Three-dimensional earthquake site response on a CM–2. In Proc.10th World Conference on Earthquake Engineering.

Louie, J. (2001). Faster, better: Shear–wave velocity to 100 meters depth from refraction microtremor arrays. *Bulletin of the Seismological Society of America*, **91(2)**, 347–364, doi: 10.1785/0120000098.

Luco, E. J., H. I. Wong and F. C. P. de Barros (1990). Three–dimensional response of a cylindrical crayon in a layered half-space. *Earthquake Engineering and Structural Dynamics*, **19(6)**, 799–817, doi: 10.1002/eqe.4290190603.

Mai, P. M. and G. C. Beroza (2003). A hybrid method for calculating near-source, broadband seismograms: application to strong motion prediction. *Physics of the Earth and Planetary Interiors*, **137(1–4)**, 183–199, doi: 10.1016/S0031-9201(03)00014-1.

Moczo, P., J. Kirstie, V. Vavrycuk, R. J. Archuleta, and L. Halada (2002). 3D heterogeneous staggered–grid finite–difference modeling of seismic motion with volume harmonic and arithmetic averaging of elastic moduli and densities. *Bulletin of the Seismological Society of America*, **92(8)**, 3042–3066, doi: 10.1785/0120010167.

Moratto L., Vuan A and A. Sarao (2015). A hybrid approach for broadband simulations of strong ground motion: The case of the 2008 Iwate–Miyagi Nairiku Earthquake. *Bulletin of the Seismological Society of America*, **105(5)**, 2823–2829, doi: 10.1785/0120150054.

Motazedian, D. (2006). Region-Specific key seismic parameters for earthquakes in Northern Iran. *Bulletin of the Seismological Society of America*, **96(4A)**, 1383–1395, doi: 10.1785/0120050162.

Motazedian, D. and A. Moinfar (2006). Hybrid stochastic finite fault modeling of 2003, M6.5, Bam earthquake (Iran). *Journal of Seismology*, **10(1)**, 91–103, doi: 10.1007/s10950-005-9003-x.

Motazedian, D, and G. M. Atkinson (2005). Stochastic finite–fault modeling based on a dynamic corner frequency. *Bulletin of the Seismological Society of America*, **95(3)**, 995–1010, doi: 10.1785/0120030207.

Nakamura Y. (1989). A method for dynamic characteristics estimation of subsurface using microtremor on the ground surface. *Railway Technical Research Institute, Quarterly Reports*, **30(1)**, 25–33.

Nickham, A. and Y. Eslamian (2010). A hybrid method for simulating near–source, broadband seismograms: Application to the 2003 Bam earthquake (Mw 6.5). *Tectonophysics*, **487(1–4)**, 46–58, doi: 10.1016/j.tecto.2010.03.007.

Olsen, K. B. and R. J. Archuleta (1996). Three-dimensional simulation of earthquakes on the Los Angeles fault system. *Bulletin of the Seismological Society of America*, **86(3)**, 575–596.

Olsen, K. B., Archuleta, R. J. and J. R. Matarese (1996). Three–dimensional simulation of a magnitude 7.75 earthquake on the San Andreas Fault. *Science*, **270(5242)**, 1628–1632, doi: 10.1126/science.270.5242.1628.

Olson, A. H., Orcutt, J. A. and G. A. Frazier (1984). The discrete wavenumber/finite element method for synthetic seismograms. *Geophysical Journal Royal Astronomical Society*, **77(2)**, 421–460, doi: 10.1111/j.1365-246X.1984.tb01942.x.

OpenSees 2.4.5. Computer Software, University of California, Berkeley, CA. Retrieved from http://opensees.berkeley.edu [last visited on December 2014].

Pacor F, Cultrera G, Mendez A and M. Cocco (2005). Finite fault modeling of strong ground motions using a hybrid deterministic–stochastic approach. *Bulletin of the Seismological Society of America*, **95(1)**, 225-240, doi: 10.1785/0120030163.

Papageorgiou, A. S. and K. Aki (1983). A specific barrier model for the quantitative description of inhomogeneous faulting and prediction of strong ground motion, Part I and II. *Bulletin of the Seismological Society of America*, **73(3)**, 693–722 and 953–978.

Park C, Miller R. and J. Xia (1999). Multichannel analysis of surface waves. *Geophysics*, **64(3)**, 800-808, doi: 10.1190/1.1444590.

Pedersen, H. A., Sánchez–Sesma F. J. and M. Campillo (1994). Three–dimensional scattering by two–dimensional topographies. *Bulletin of the Seismological Society of America*, **84(4)**, 1169–1183.

Pitarka, A., Irikura, K., Iwata, T. and H. Sekiguchi (1998). Three–dimensional simulation of the near–fault ground motion for the 1995 Hyogoken Nanbu

(Kobe), Japan, earthquake. *Bulletin of the Seismological Society of America*, **88(2)**, 428–440.

Pitarka, A., Somerville, P., Fukushima, Y., Uetake T. and K. Irikura (2000). Simulation of near–fault strong–ground motion using hybrid Green's functions. *Bulletin of the Seismological Society of America*, **90(3)**, 566–586, doi: 10.1785/0119990108.

Priolo, E., Carcione, J. M. and G. Seriani (1994). Numerical simulation of interface waves by high–order spectral modeling techniques. *The Journal of Acoustical Society of America*, **95(2)**, 681–693, doi: 10.1121/1.408428.

Pulido, N., Ojeda, A., Atakan, K. and T. Kubo (2004). Strong ground motion estimation in the Sea of Marmara region (Turkey) based on a scenario earthquake. *Tectonophysics*, **391(1–4)**, 357–374, doi: 10.1016/j.tecto.2004.07.023.

Raghukanth, S. T. G. and S. N. Somala (2009). Modeling of strong–motion data in Northeastern India: Q, stress drop, and site amplification. *Bulletin of the Seismological Society of America*, **99(2A)**, 705–725, doi: 10.1785/0120080025.

Rial, J. A., Saltzman, N. G. and H. Ling (1992). Earthquake–induced resonance in sedimentary basins. *American Scientists*, **80(6)**, 566–578.

Sánchez–Sesma, F. J. (1987). Site effects on strong ground motion. *Soil Dynamics and Earthquake Engineering*, **6(2)**, 124–132, doi: 10.1016/0267-7261(87)90022-4.

Schmidt, R. (1986). Multiple emitter location and signal parameter estimation. *Antennas and Propagation Society*, IEEE, **34(3)**, 276–280, doi: 10.1109/TAP.1986.1143830.

Schnabel, P. B., Lysmer, J. and H. B. Seed (1972). SHAKE, a computer program for earthquake response analysis of horizontal layered sites, Report No. EERC 72–12.

Scott, B., Park, R. and M. Priestley (1982). Stress–strain behavior of concrete confined by overlapping hoops at low and high strain rates. *J Proc.*, **79(1)**, 13–27.

Shahjouei, A. and S. Pezeshk (2015). Synthetic Seismograms Using a hybrid broadband ground–motion simulation approach: Application to Central and Eastern United States. *Bulletin of the Seismological Society of America*, **105(2A)**, 686–705, doi: 10.1785/0120140219.

Shoja-Taheri J. and H. Ghofrani (2007). Stochastic finite–fault modeling of strong ground motions from the 26 December 2003 Bam, Iran, earthquake. *Bulletin of the Seismological Society of America*, **97(6)**, 1950–1959, doi: 10.1785/0120060059.

Spudich, P. and L. Xu (2003). Documentation of software package COMPSYN: Programs for earthquake ground motion calculations using complete 1–D Green's functions. IASPEI Handbook of Earthquake and Engineering Seismology, Academic Press, 56 pp.

Spudich, P. and R. J. Archuleta (1987). Techniques for earthquake ground–motion calculation with applications to source parameterization of finite faults. *Seismic strong motion synthetics*, **37**, 205–265.

Stokoe, K., Wright, S., Bay, J. A. and J. M. Roesset (1994). Characterization of geotechnical sites by SASW method, in Technical Report-Geophysical Characterization of Sites. ISSMFE Technical Committee #10 for XIII ICSMFE, Geophysical characterization of sites. A. A. Balkema Publishers/Rotterdam & Brookfield, Netherlands, 15–26.

Suzuki, T., Adachi, Y. and M. Tanaka (1993). Application of microtremor measurements to the estimation of earthquake ground motions in Kushiro city during the Kushiro-Oki earthquake of 15 January 1993. *Earthquake Engineering and Structural Dynamics*, **24(4)**, 595–613, doi: 10.1002/eqe.4290240409.

Taucer, F. F., Spacone, E. and F. C. Filippou (1991). A fiber beam-column element for seismic response analysis of reinforced concrete structures. University of California, Berkeley/Earthquake Engineering Research Center, **91(17)**.

Thomson, W. (1959). Spectral aspect of earthquakes. *Bulletin of the Seismological Society of America*, **49(1)**, 91–98.

Toro, G. and R. McGuire (1987). An investigation into earthquake ground motion characteristics in eastern North America. *Bulletin of the Seismological Society of America*, **77(2)**, 468–489.

Toshinawa, T. and T. Ohmachi (1992). Love-wave propagation in a three-dimensional sedimentary basin. *Bulletin of the Seismological Society of America*, **82(4)**, 1661–1677.

Ugurhan, B. and A. Askan (2010). Stochastic strong ground motion simulation of the 12 November 1999 Düzce (Turkey) earthquake using a dynamic corner frequency approach. *Bulletin of the Seismological Society of America*, **100(4)**, 1498-1512, doi: 10.1785/0120090358.

Ugurhan, B., Askan, A., Akinci, A. and L. Malagnini (2012). Strong–ground–motion simulation of the 6 April 2009 L'Aquila, Italy, Earthquake. *Bulletin of the Seismological Society of America*, **102(4)**, 1429–1445, doi: 10.1785/0120110060.

Umutlu, N., K. Koketsu, and C. Milkereit (2004). The rupture process during the 1999 Duzce, Turkey, earthquake from joint inversion of teleseismic and strong-motion data. *Tectonophysics*, **39(1)**, 315–324.

Utkucu, M., Nalbant, S. S., McCloskey, J., Steacy, S., and O. Alptekin (2003). Slip distribution and stress changes associated with the 1999 November 12, Düzce (Turkey) earthquake (Mw = 7.1). *Geophysical Journal International*, **153(1)**, 229–241, doi: 10.1046/j.1365-246X.2003.01904.x.

Yagi, Y. and M. Kikuchi (2000). Source rupture process of the Kocaeli, Turkey, earthquake of August 17, 1999, obtained by joint inversion of near–field data and teleseismic data. *Geophysical Research Letters*, **27(13)**, 1969–1972, doi: 10.1029/1999GL011208.

Yagi, Y., Kikuchi, M., Yoshida, S. and T. Sagiya (1999). Comparison of the coseismic rupture with the aftershock distribution in the Hyuga–nada earthquakes of 1996. *Geophysical Research Letters*, **26(20)**, 3161–3164, doi: 10.1029/1999GL005340.

Yalcinkaya E. (2005). Stochastic finite–fault modeling of ground motions from the June 27, 1998 Adana–Ceyhan earthquake. *Earth, Planets and Space*, **57(2)**, 107–115, doi: 10.1186/BF03352554.

Yılmaz H. (2007). Correlation of deformation demands with ground motion intensity. Master of Science Thesis, Department of Civil Engineering, Middle East Technical University, Ankara, Turkey.

Yomogida K and J. Etgen (1993). 3–D wave propagation in the Los Angeles basin for the Whittier–Narrows earthquake. *Bulletin of the Seismological Society of America*, **83(5)**, 1325–1344.

Zengin, E. and E. Cakti (2014). Ground motion simulations for the 23 October 2011 Van, Eastern Turkey earthquake using stochastic finite fault approach. *Bulletin of Earthquake Engineering*, **12(2)**, 627–646, doi: 10.1007/s11069-012-0263-9.

APPENDICES

A. SIMULATED ACCELERATION-TIME AND VELOCITY-TIME HISTORIES FOR SCENARIO EVENTS

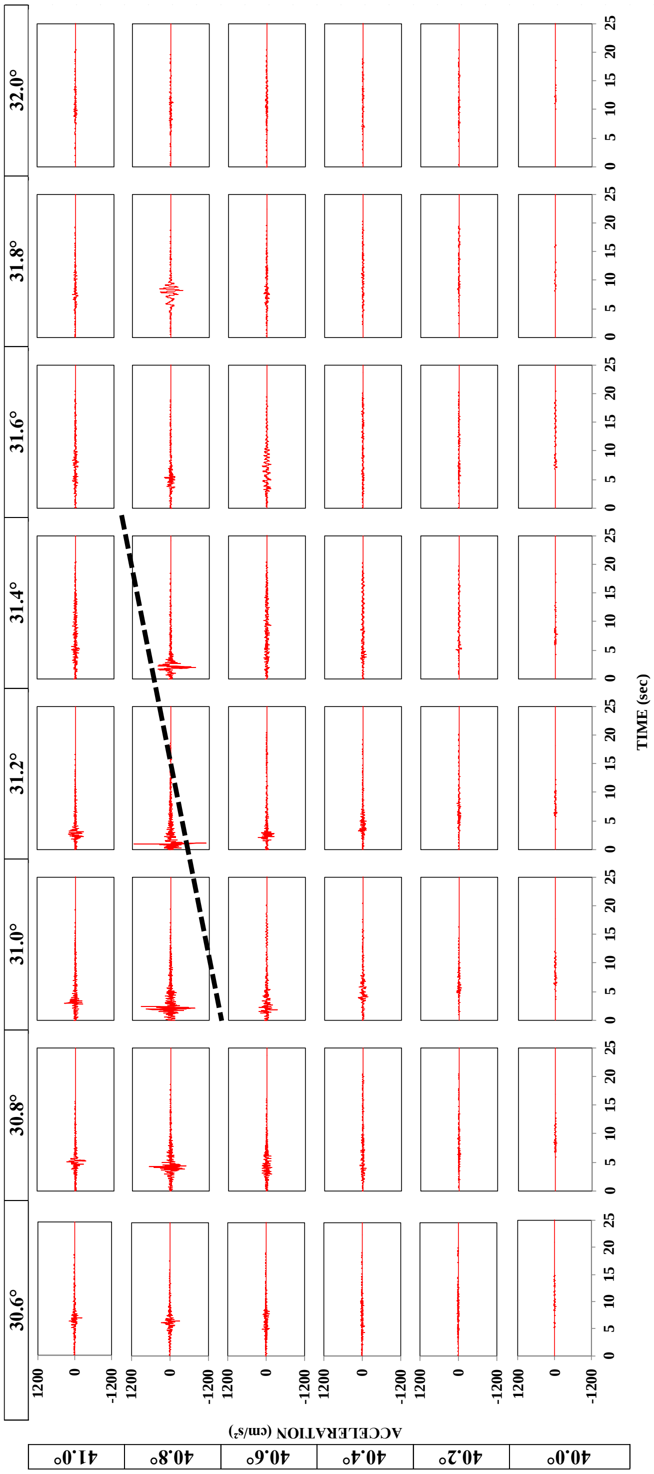

Figure A.1. Simulated acceleration-time histories in E-W direction for the 1999 Duzce event (Mw=7.1) – showing fault plane with black dashed line

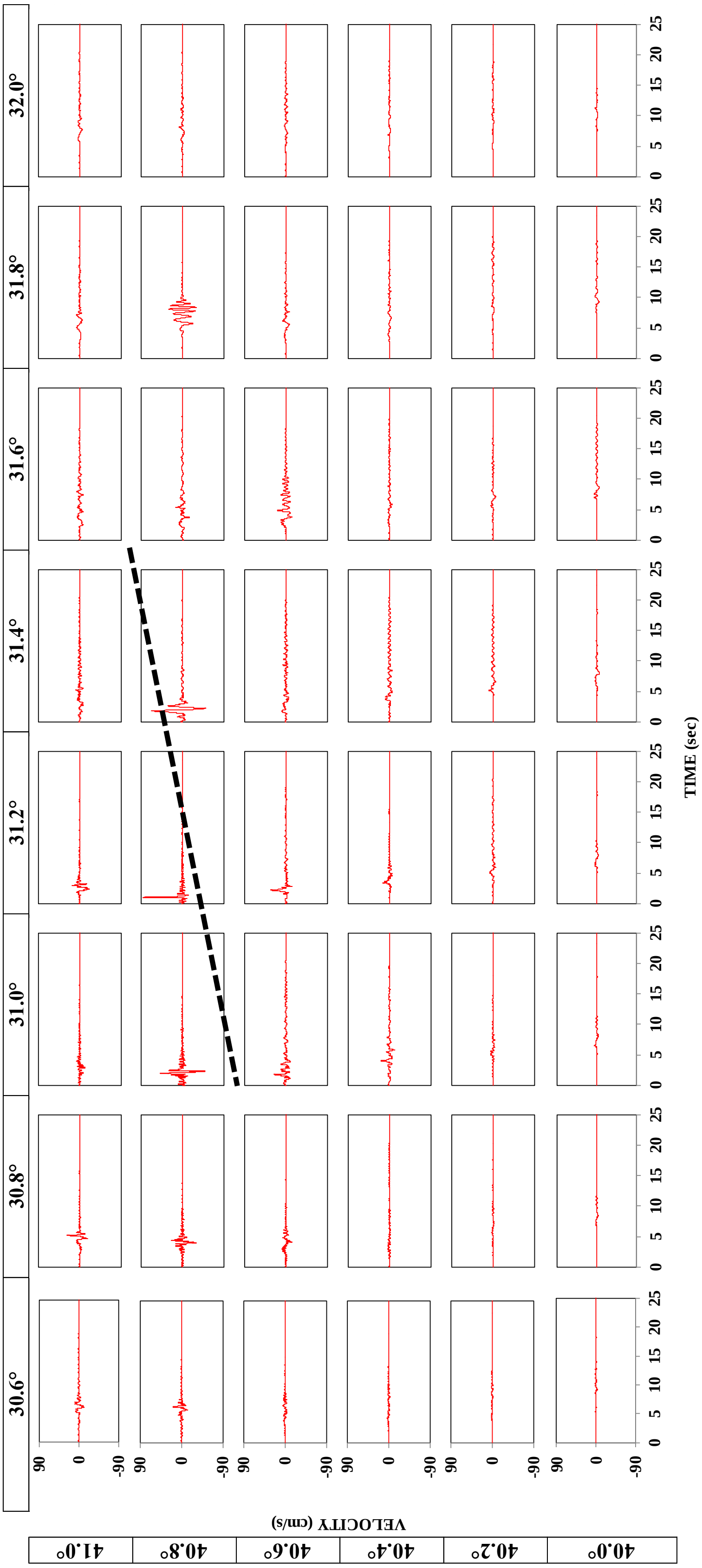

Figure A.2. Simulated velocity-time histories in E-W direction for the 1999 Duzce event (Mw=7.1) – showing fault plane with black dashed line

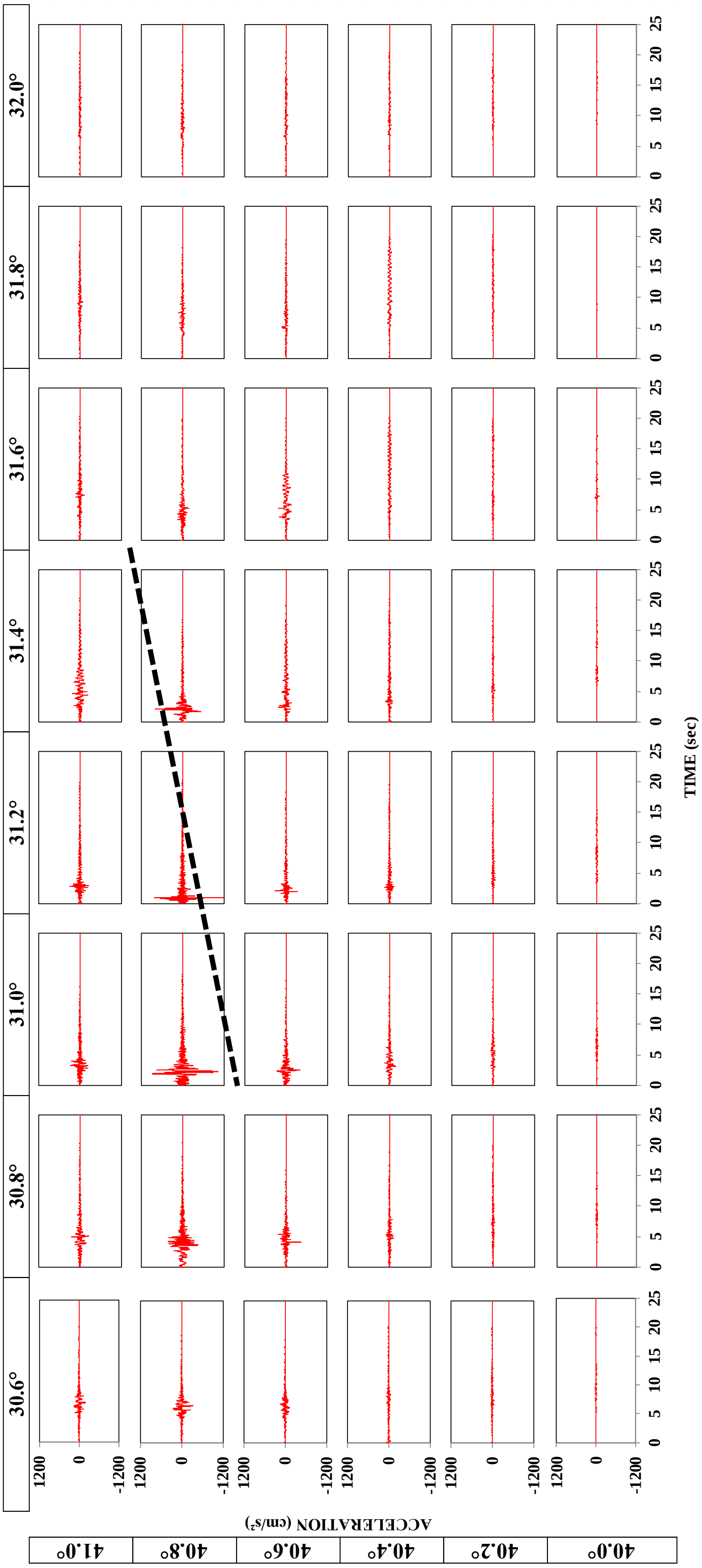

Figure A.3. Simulated acceleration-time histories in N-S direction for the 1999 Duzce event (Mw=7.1) – showing fault plane with black dashed line

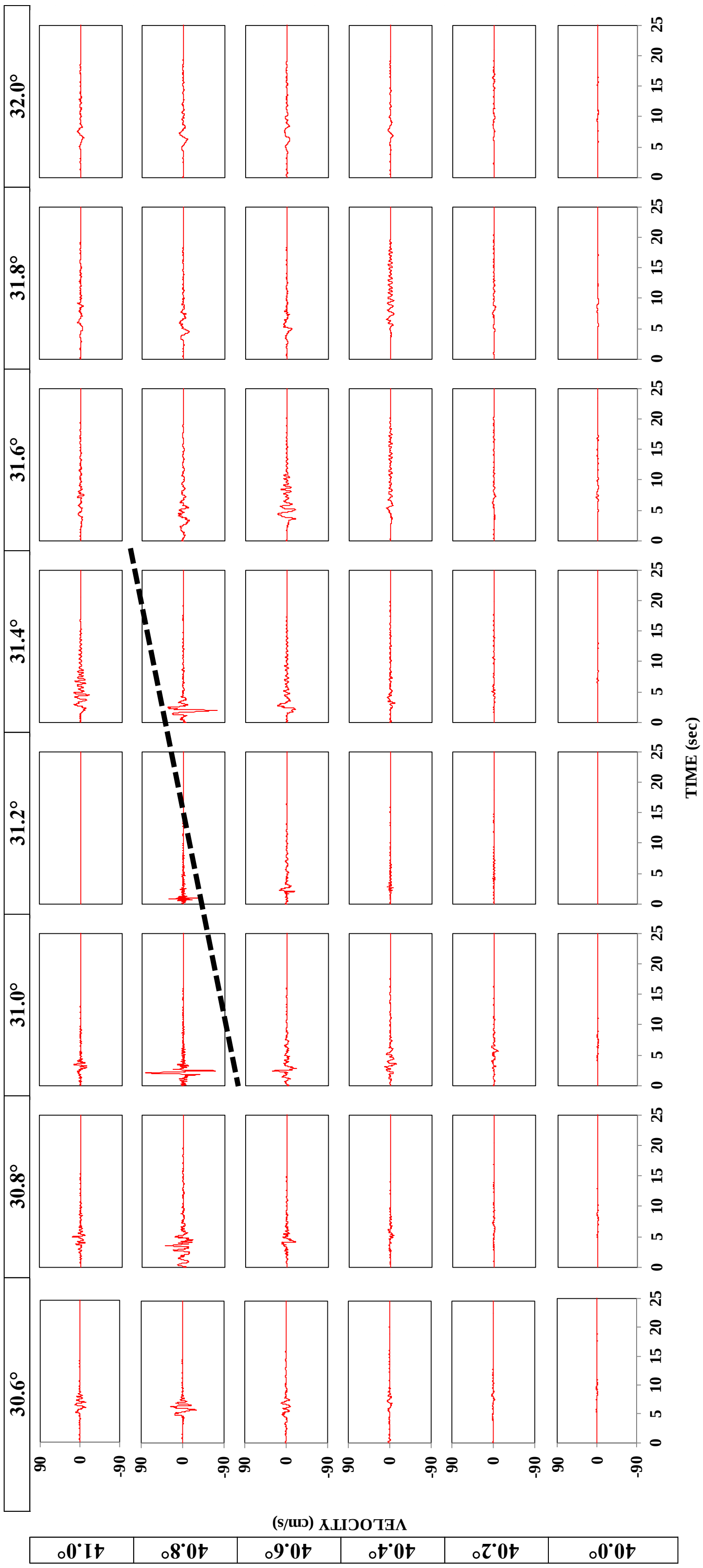

Figure A.4. Simulated velocity-time histories in N-S direction for the 1999 Duzce event (Mw=7.1) – showing fault plane with black dashed line

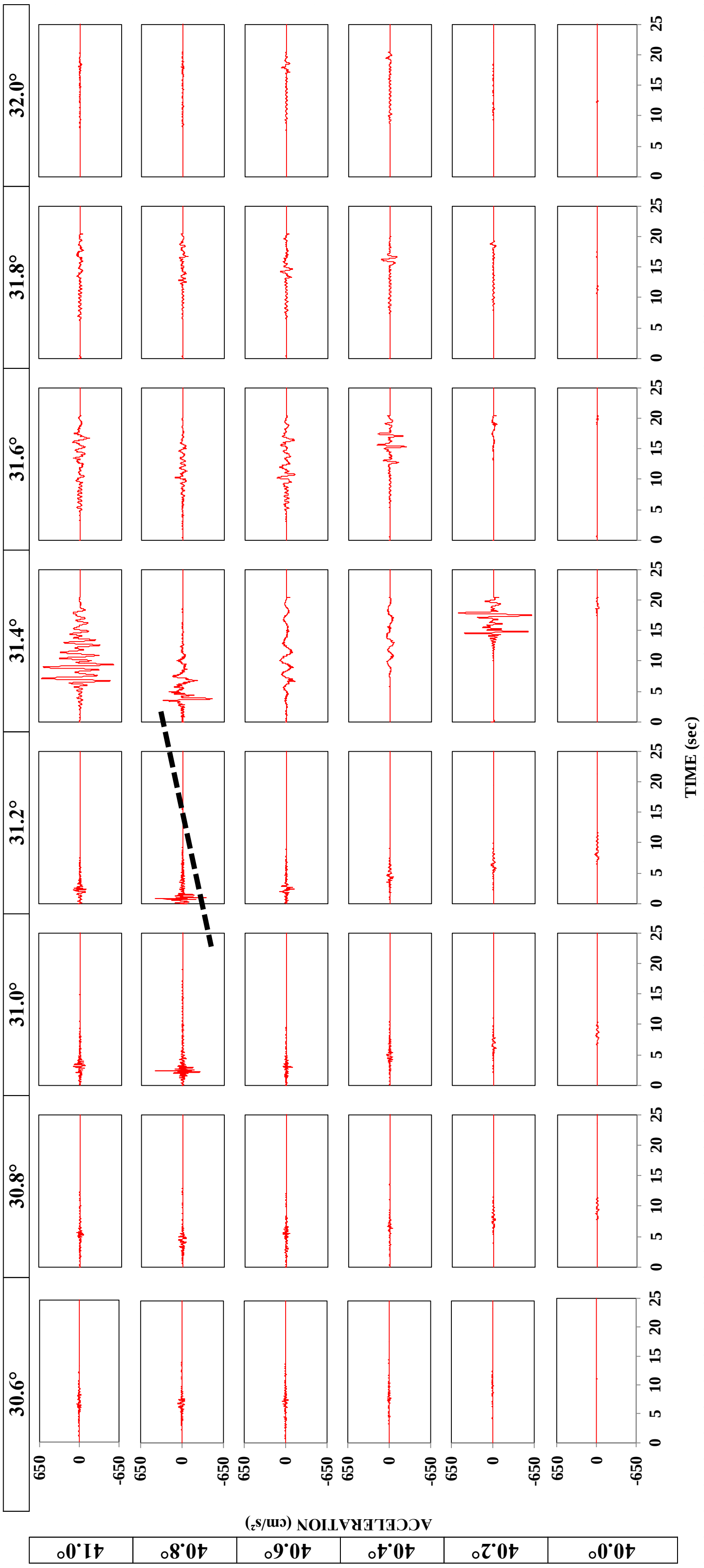

Figure A.5. Simulated acceleration-time histories in E-W direction for scenario event Mw=6.5 – showing fault plane with black dashed line

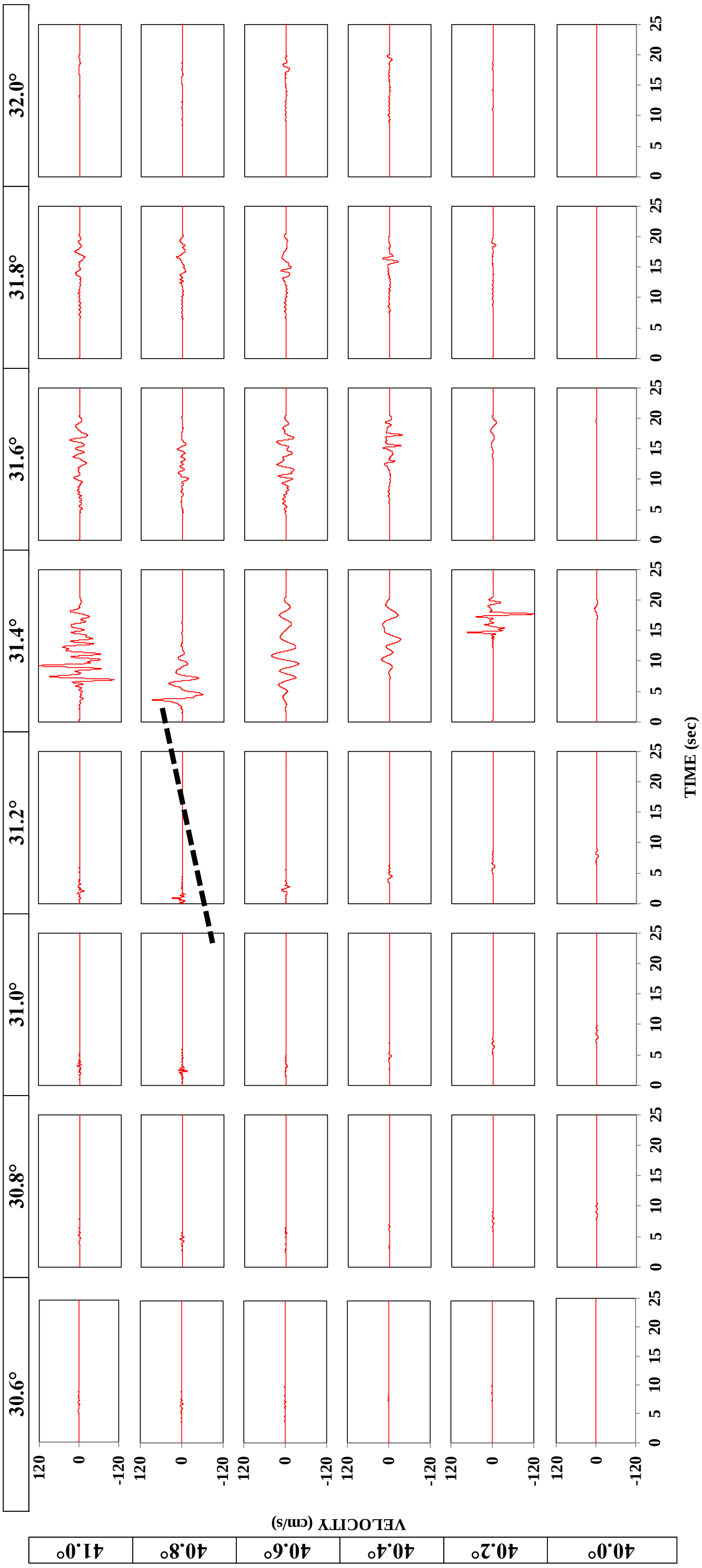

Figure A.6 Simulated velocity-time histories in E-W direction for scenario event Mw=6.5 – showing fault plane with black dashed line

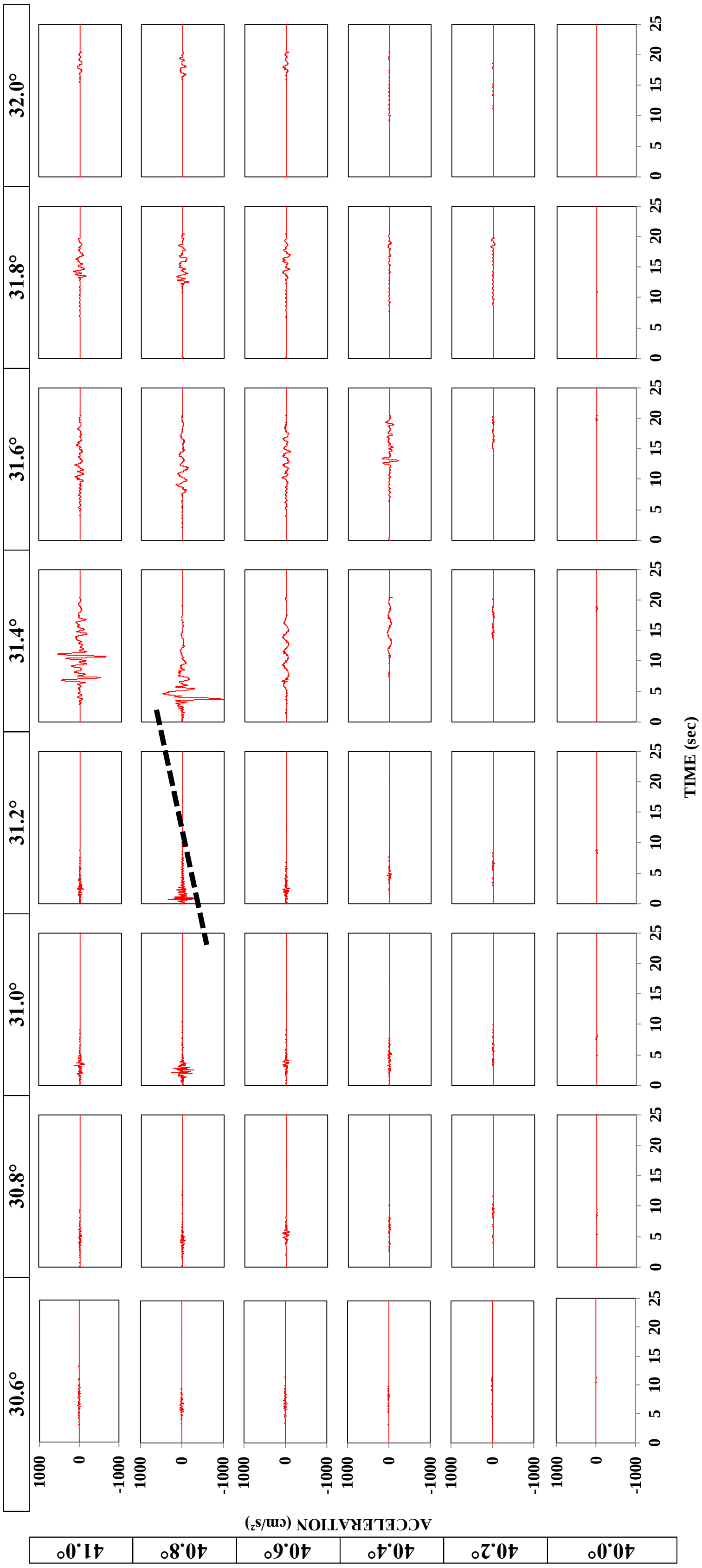

Figure A.7 Simulated acceleration-time histories in N-S direction for scenario event Mw=6.5 – showing fault plane with black dashed line

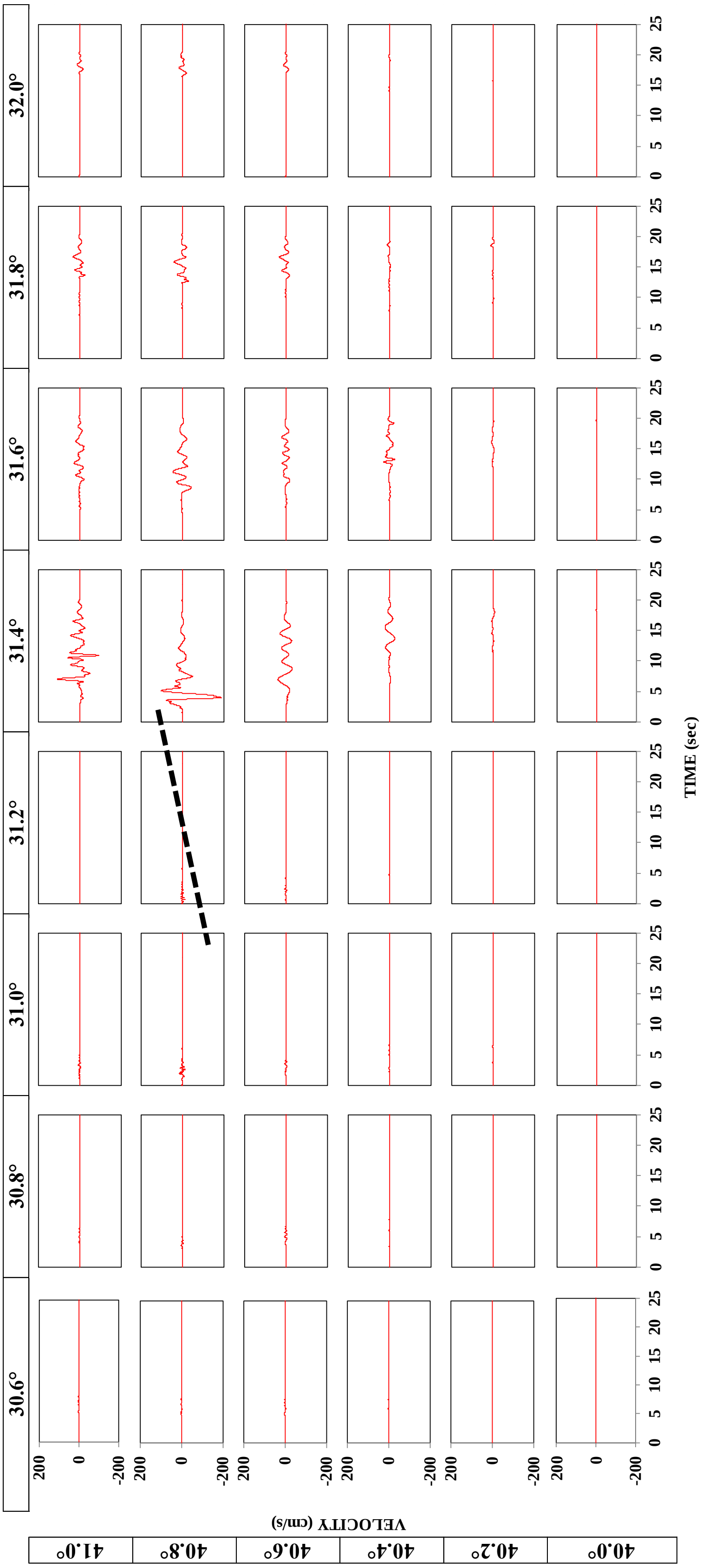

Figure A.8 Simulated velocity-time histories in N-S direction for scenario event Mw=6.5 – showing fault plane with black dashed line

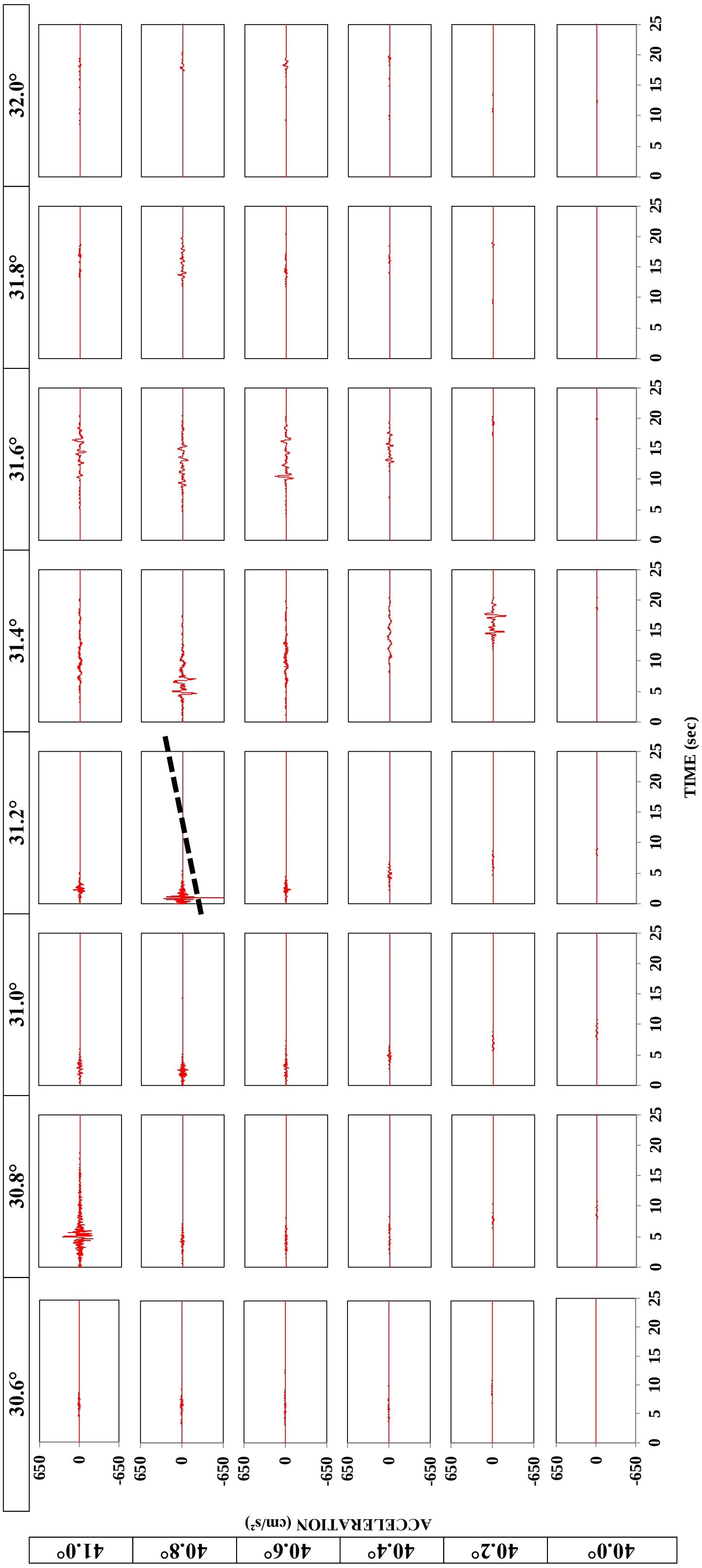

Figure A.9 Simulated acceleration-time histories in E-W direction for scenario event Mw=6.0 – showing fault plane with black dashed line

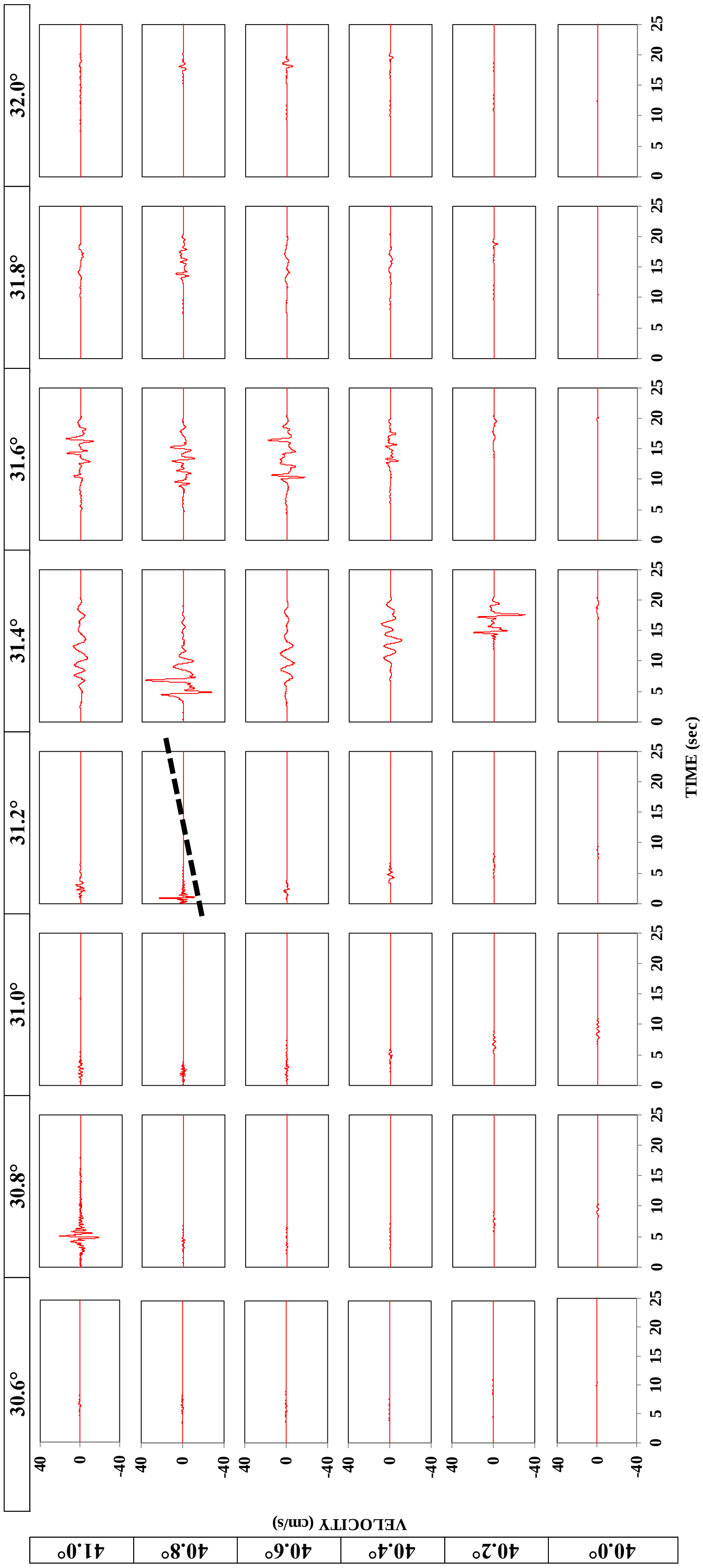

Figure A.10 Simulated velocity-time histories in E-W direction for scenario event Mw=6.0 – showing fault plane with black dashed line

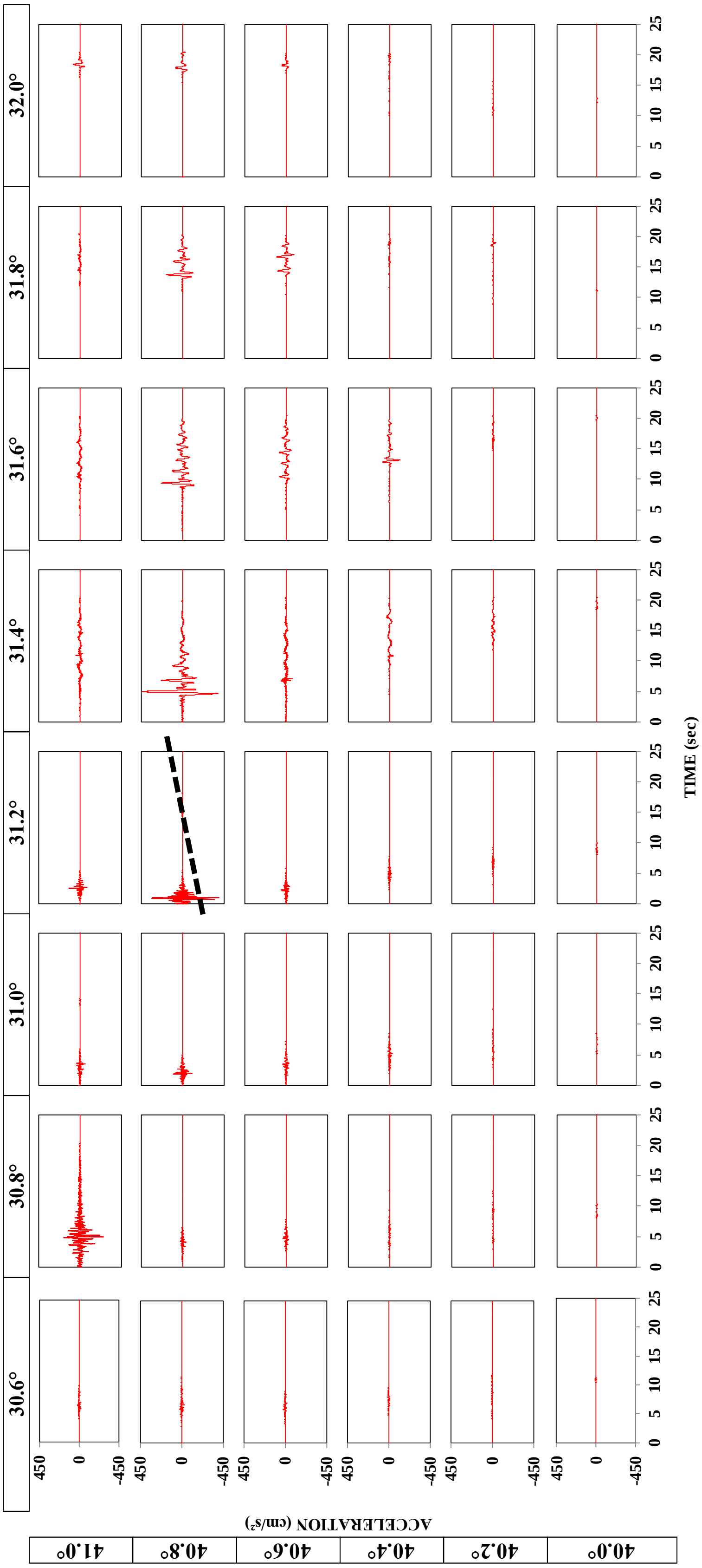

Figure A.11 Simulated acceleration-time histories in N-S direction for scenario event Mw=6.0 – showing fault plane with black dashed line

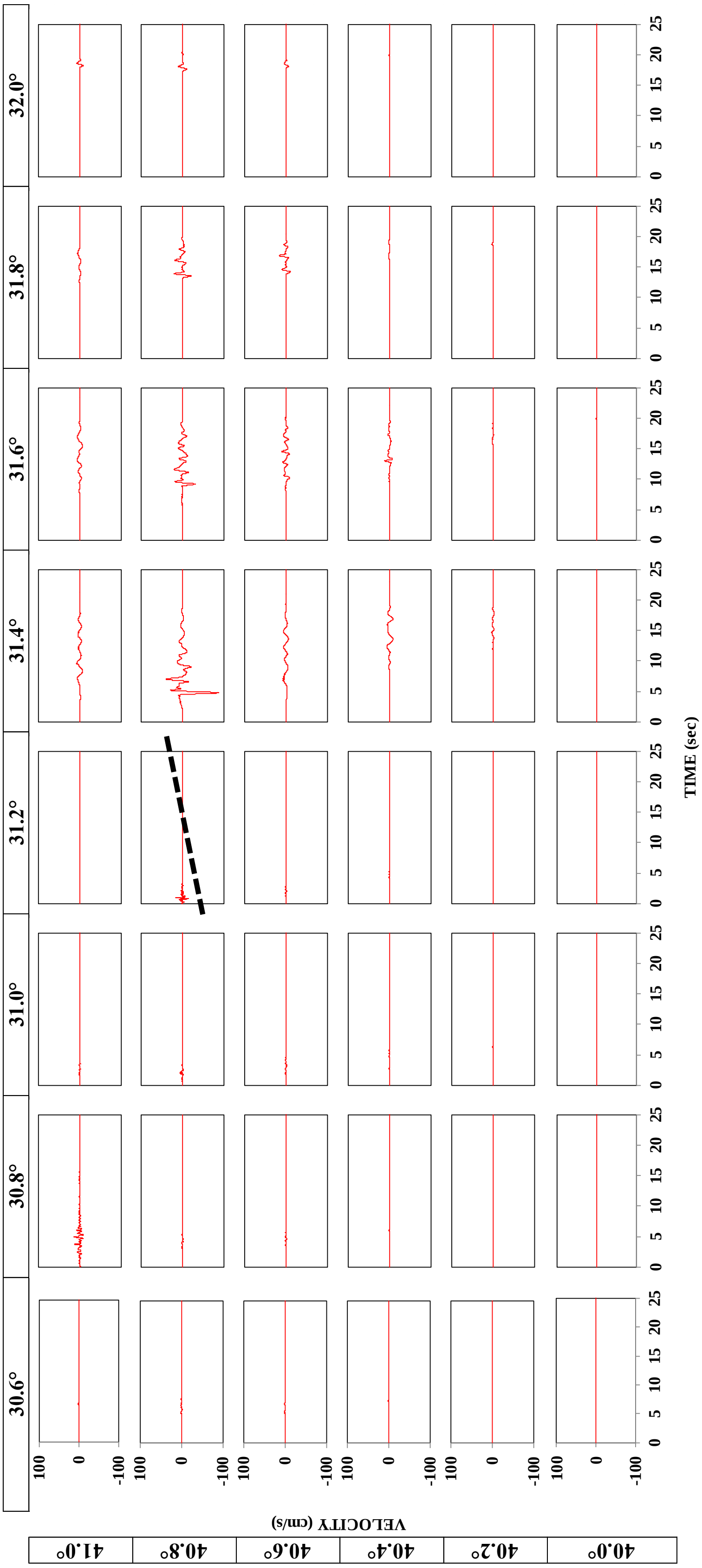

Figure A.12 Simulated velocity-time histories in N-S direction for scenario event Mw=6.0 – showing fault plane with black dashed line

B. GMPE TABLES

Table B.1. *Comparison of simulated peak amplitudes with empirical estimates from GMPE's for the 1999 Duzce earthquake (Mw=7.1)*

Stations	R_{jb} (km)	PGA (cm/s²)				PGV (cm/s)			
		Simulated EW	Simulated NS	Estimated using BA08	Estimated using AC10	Simulated EW	Simulated NS	Estimated using BA08	Estimated using AC10
11	82.94	40.14	34.91	62.03	27.09	2.95	1.95	6.65	4.93
12	82.42	46.15	35.83	62.54	27.28	4.26	2.30	6.68	4.95
13	84.14	62.54	42.41	60.89	26.66	6.08	2.42	6.56	4.87
14	85.91	46.85	34.15	59.21	26.02	5.02	3.09	6.44	4.80
15	87.67	64.89	39.82	57.64	25.44	6.37	2.44	6.33	4.72
16	89.44	53.60	67.31	56.07	24.86	6.41	4.08	6.21	4.65
17	92.63	34.91	26.64	53.38	23.88	5.08	2.47	6.02	4.53
18	98.65	31.74	17.03	48.75	22.24	3.41	1.98	5.67	4.31
21	61.00	41.31	52.61	88.49	38.22	2.45	3.24	8.61	6.23
22	60.29	67.03	45.61	89.57	38.73	2.80	3.08	8.69	6.29
23	62.05	89.30	77.72	86.96	37.52	5.85	9.03	8.50	6.15
24	63.82	65.42	54.52	84.43	36.36	7.27	2.54	8.30	6.02
25	65.58	87.49	63.75	82.00	35.28	9.87	4.51	8.12	5.90
26	67.37	61.81	45.77	79.63	34.24	5.76	4.82	7.94	5.78
27	71.55	34.44	29.10	74.38	32.01	3.80	3.86	7.55	5.52
28	79.19	35.93	32.61	65.81	28.55	2.70	2.55	6.92	5.11
31	39.35	78.45	76.68	129.55	61.21	3.60	5.55	11.98	8.63
32	38.20	94.26	101.59	132.37	63.12	4.06	7.35	12.24	8.81
33	39.97	153.18	173.14	128.07	60.21	19.25	13.36	11.85	8.53
34	41.73	145.88	138.30	123.96	57.55	13.83	6.95	11.49	8.26
35	43.49	94.01	129.59	120.04	55.09	9.05	10.24	11.15	8.02
36	45.44	54.81	59.94	115.89	52.60	5.40	8.40	10.80	7.76
37	51.44	56.70	76.26	104.22	46.06	4.17	8.49	9.84	7.08
38	61.62	43.81	43.03	87.59	37.80	2.59	5.90	8.54	6.18
41	19.06	108.85	155.22	200.52	126.11	5.70	10.75	19.48	14.45
42	16.11	157.22	442.42	217.77	147.18	12.94	19.33	21.67	16.20
43	17.88	335.14	400.36	207.05	133.87	25.14	31.17	20.29	15.10
44	19.64	269.15	331.60	197.47	122.60	32.86	17.47	19.11	14.16
45	21.41	128.66	225.17	188.78	112.90	9.25	20.77	18.08	13.34
46	24.04	142.53	226.43	177.21	100.84	17.73	20.02	16.76	12.29
47	34.04	82.61	123.38	143.34	71.06	7.82	12.17	13.26	9.58
48	48.06	56.28	66.21	110.60	49.55	3.87	6.57	10.36	7.45
51	10.22	302.74	335.75	266.16	212.61	19.18	31.20	28.58	21.55
52	1.00	663.34	450.72	**521.91**	**367.97**	30.57	39.67	**65.34**	**36.69**
53	1.00	916.97	1021.22	**521.91**	**367.97**	49.27	**81.77**	**65.34**	**36.69**
54	1.00	**1157.55**	**1176.61**	**521.91**	**367.97**	**86.11**	36.97	**65.34**	**36.69**
55	1.00	770.50	801.32	**521.91**	**367.97**	66.96	74.08	**65.34**	**36.69**
56	8.78	187.47	169.86	282.95	235.34	15.39	13.96	31.22	23.44
57	25.66	371.11	131.42	170.75	94.51	30.14	13.03	16.05	11.73
58	42.53	69.95	59.81	122.17	56.42	6.50	9.27	11.33	8.15
61	20.45	228.36	190.30	193.38	117.96	11.64	13.69	18.62	13.77
62	17.10	318.83	247.83	211.62	139.46	27.08	17.83	20.87	15.57
63	15.34	333.93	260.09	222.86	153.70	11.95	15.41	22.34	16.74
64	13.57	262.85	300.39	235.69	170.71	21.71	10.65	24.10	18.12
65	11.81	124.85	230.43	250.49	190.95	8.90	18.54	26.22	19.77
66	14.92	100.71	139.14	225.75	157.48	8.84	8.24	22.73	17.05
67	29.02	93.25	74.37	158.71	83.57	7.85	6.71	14.79	10.75
68	45.08	60.06	59.04	116.64	53.04	6.31	7.01	10.86	7.81

Table B.2. *Comparison of simulated peak amplitudes with empirical estimates from GMPE's for scenario earthquake with Mw=6.5*

Stations	R_{jb} (km)	PGA (cm/s²)				PGV (cm/s)			
		Simulated EW	Simulated NS	Estimated using BA08	Estimated using AC10	Simulated EW	Simulated NS	Estimated using BA08	Estimated using AC10
11	95.41	7.79	11.65	34.12	14.63	0.78	1.08	3.07	2.20
12	90.05	29.61	13.80	37.18	15.72	2.52	1.14	3.25	2.32
13	87.67	25.40	19.03	38.65	16.26	4.43	1.47	3.34	2.37
14	88.42	41.44	24.12	38.18	16.08	5.33	1.15	3.31	2.35
15	90.19	29.99	25.08	37.10	15.69	7.87	3.50	3.25	2.31
16	92.74	18.86	23.18	35.59	15.15	2.47	2.84	3.16	2.25
17	98.06	12.64	9.86	32.72	14.14	1.01	1.39	2.99	2.14
18	105.84	11.78	10.23	28.97	12.85	1.09	1.14	2.77	2.00
21	75.54	21.68	13.79	47.31	19.57	1.51	0.90	3.84	2.71
22	68.65	33.00	22.86	53.29	22.03	2.95	1.12	4.19	2.95
23	65.49	39.74	29.36	56.36	23.35	4.45	2.61	4.37	3.08
24	66.34	43.33	36.34	55.51	22.98	5.72	1.34	4.32	3.05
25	68.10	595.39	30.64	53.81	22.25	118.99	7.69	4.22	2.98
26	71.34	54.85	28.59	50.85	21.00	11.59	7.98	4.05	2.85
27	78.13	55.74	55.69	45.28	18.77	8.40	10.39	3.72	2.63
28	87.69	16.09	23.22	38.64	16.25	2.08	1.69	3.34	2.37
31	57.41	30.25	22.58	65.27	27.44	1.62	1.64	4.90	3.47
32	47.99	43.88	23.67	78.11	34.08	2.07	2.40	5.69	4.06
33	43.35	51.36	52.60	85.68	38.45	5.84	4.31	6.18	4.44
34	44.25	60.43	51.50	84.14	37.53	7.53	3.12	6.08	4.36
35	46.01	64.43	58.39	81.22	35.84	33.69	26.64	5.89	4.21
36	50.62	257.04	219.70	74.19	31.95	36.86	28.73	5.45	3.87
37	59.82	137.15	49.90	62.44	26.10	24.53	10.40	4.73	3.34
38	71.85	61.96	22.17	50.41	20.82	7.71	3.41	4.02	2.84
41	43.28	46.04	42.66	85.80	38.52	2.96	3.87	6.19	4.44
42	29.65	51.64	81.04	115.32	59.54	2.92	6.26	8.27	6.15
43	21.34	98.75	76.06	142.56	85.23	5.10	6.63	10.48	8.09
44	22.16	120.52	92.25	139.33	81.87	12.45	6.00	10.20	7.84
45	24.03	138.19	92.63	132.50	75.04	41.69	39.39	9.63	7.34
46	31.99	150.67	104.59	109.26	54.67	26.55	19.97	7.81	5.77
47	45.15	98.03	98.75	82.62	36.63	15.35	31.74	5.98	4.28
48	60.19	73.48	80.44	62.02	25.90	10.82	15.32	4.71	3.32
51	37.54	68.97	50.73	96.69	45.51	4.56	4.66	6.92	5.03
52	20.75	66.69	65.38	144.98	87.81	6.20	5.47	10.69	8.28
53	3.97	430.90	274.73	318.92	274.89	15.63	15.74	29.73	22.52
54	1.00	430.13	354.02	**472.31**	**312.56**	30.26	12.00	**42.82**	**26.48**
55	4.95	466.91	**986.80**	291.92	257.07	87.44	**186.59**	26.60	20.91
56	21.68	119.08	162.06	141.21	83.82	19.13	45.50	10.37	7.99
57	38.54	77.95	160.79	94.67	44.14	17.20	40.41	6.78	4.92
58	55.41	21.99	88.01	67.75	28.65	2.21	20.59	5.05	3.58
61	42.02	44.26	29.59	88.03	39.89	2.99	2.90	6.33	4.56
62	28.06	60.09	46.91	119.75	63.31	3.28	2.71	8.61	6.44
63	19.47	104.52	144.97	150.53	93.86	6.65	9.27	11.18	8.72
64	17.63	110.70	88.77	159.32	103.91	12.51	2.14	11.98	9.44
65	17.31	**609.34**	629.87	160.98	105.88	**119.10**	109.41	12.13	9.58
66	27.58	158.79	140.05	121.14	64.52	28.82	26.44	8.72	6.54
67	42.33	56.08	152.75	87.48	39.55	15.99	31.01	6.30	4.53
68	58.24	23.28	67.67	64.27	26.97	2.92	17.32	4.84	3.42

Table B.3. *Comparison of simulated peak amplitudes with empirical estimates from GMPE's for scenario earthquake with Mw=6.0*

Stations	R_{jb} (km)	PGA (cm/s^2)				PGV (cm/s)			
		Simulated EW	Simulated NS	Estimated using BA08	Estimated using AC10	Simulated EW	Simulated NS	Estimated using BA08	Estimated using AC10
11	100.15	5.93	6.67	19.77	7.72	0.50	0.46	1.59	0.93
12	93.40	11.73	7.80	22.10	8.48	1.00	0.53	1.71	0.99
13	89.37	13.83	6.44	23.64	8.99	1.54	0.37	1.79	1.04
14	88.43	9.46	9.69	24.02	9.12	0.71	0.61	1.81	1.05
15	90.01	17.42	14.87	23.39	8.91	1.42	1.07	1.78	1.03
16	93.48	10.27	12.64	22.07	8.47	0.96	1.52	1.71	0.99
17	99.73	6.19	7.41	19.90	7.76	0.42	0.62	1.60	0.93
18	108.27	7.37	5.42	17.34	6.96	0.61	0.57	1.46	0.86
21	81.22	16.50	8.92	27.19	10.22	0.58	0.54	1.97	1.14
22	72.74	16.23	9.21	31.61	11.84	1.16	0.50	2.20	1.28
23	67.49	14.88	11.50	34.81	13.08	1.95	0.92	2.36	1.38
24	66.24	16.51	15.14	35.63	13.41	1.29	0.68	2.40	1.40
25	68.00	202.71	24.03	34.48	12.95	29.81	4.05	2.34	1.37
26	72.53	17.34	15.15	31.73	11.89	2.43	2.10	2.20	1.28
27	80.42	29.62	26.94	27.57	10.36	3.21	2.86	1.99	1.15
28	90.80	6.64	10.06	23.08	8.81	0.61	0.75	1.76	1.02
31	64.44	11.75	15.51	36.86	13.91	0.59	0.89	2.46	1.44
32	53.35	13.84	13.38	45.84	17.86	0.83	0.75	2.93	1.74
33	45.93	39.21	29.96	53.58	21.73	2.17	1.38	3.34	2.02
34	44.08	30.81	20.51	55.79	22.92	3.33	1.34	3.46	2.11
35	46.18	34.19	35.52	53.29	21.58	10.78	8.58	3.33	2.01
36	52.63	69.44	110.57	46.51	18.18	8.06	11.08	2.96	1.77
37	63.06	18.87	15.03	37.84	14.32	2.03	1.54	2.51	1.47
38	75.84	24.30	15.46	29.90	11.20	2.32	0.96	2.11	1.22
41	51.90	14.04	22.56	47.23	18.52	0.73	1.27	3.00	1.79
42	37.25	21.03	32.73	65.22	28.45	1.00	2.65	3.99	2.49
43	25.52	36.90	37.80	88.30	45.42	2.16	2.67	5.42	3.58
44	21.98	67.90	50.98	98.04	54.15	2.78	2.01	6.08	4.12
45	25.05	36.01	63.43	89.50	46.45	7.35	8.27	5.50	3.65
46	35.56	168.04	74.89	67.92	30.18	18.49	9.90	4.15	2.60
47	49.71	25.74	98.05	49.43	19.60	2.65	16.38	3.12	1.87
48	65.17	55.67	48.54	36.36	13.71	5.63	6.58	2.44	1.43
51	46.84	26.59	28.56	52.53	21.18	1.46	2.37	3.29	1.98
52	30.04	35.48	41.90	78.05	37.26	1.55	2.00	4.76	3.07
53	13.26	79.96	105.54	134.06	93.22	3.15	5.43	8.83	6.45
54	1.00	**652.90**	399.46	**385.88**	**227.32**	23.31	17.00	**28.18**	**16.05**
55	10.45	221.47	**440.35**	153.12	115.97	**36.66**	**87.12**	10.45	7.81
56	27.31	89.69	235.91	83.99	41.87	12.52	30.77	5.14	3.36
57	44.19	73.01	178.24	55.66	22.85	7.22	20.60	3.46	2.10
58	61.06	32.06	77.18	39.32	14.94	3.98	11.31	2.59	1.52
61	50.14	24.07	17.93	48.98	19.38	1.15	1.12	3.10	1.85
62	34.98	271.57	258.08	68.88	30.81	20.53	15.06	4.21	2.65
63	22.43	57.41	54.34	96.71	52.91	2.51	2.43	5.99	4.04
64	17.82	112.15	123.96	112.32	68.57	4.42	4.35	7.12	4.99
65	20.43	44.19	41.61	102.93	58.88	7.33	7.38	6.42	4.41
66	32.71	112.33	35.51	72.88	33.52	14.35	7.53	4.45	2.82
67	47.87	20.62	27.68	51.39	20.59	2.96	4.87	3.22	1.94
68	63.90	18.71	72.53	37.24	14.07	1.78	8.54	2.48	1.45

C. MISFIT COMPARISONS

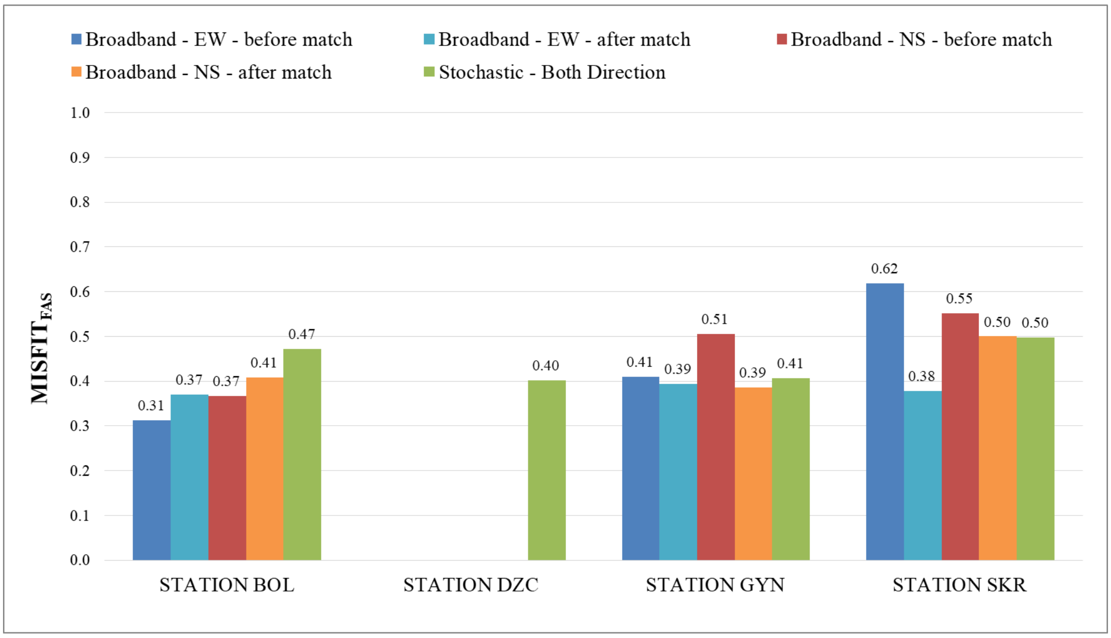

Figure C.13. FAS misfit comparisons of real and simulated records for E-W and N-S components – all stations

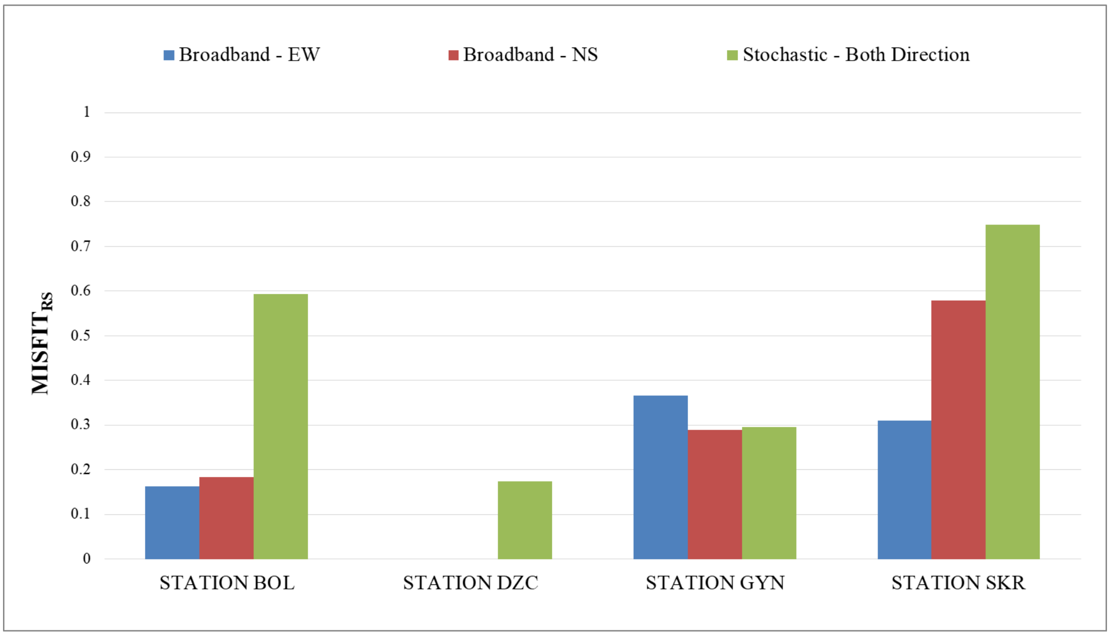

Figure C.2. RS misfit comparisons of real and simulated records for E-W and N-S components – all stations

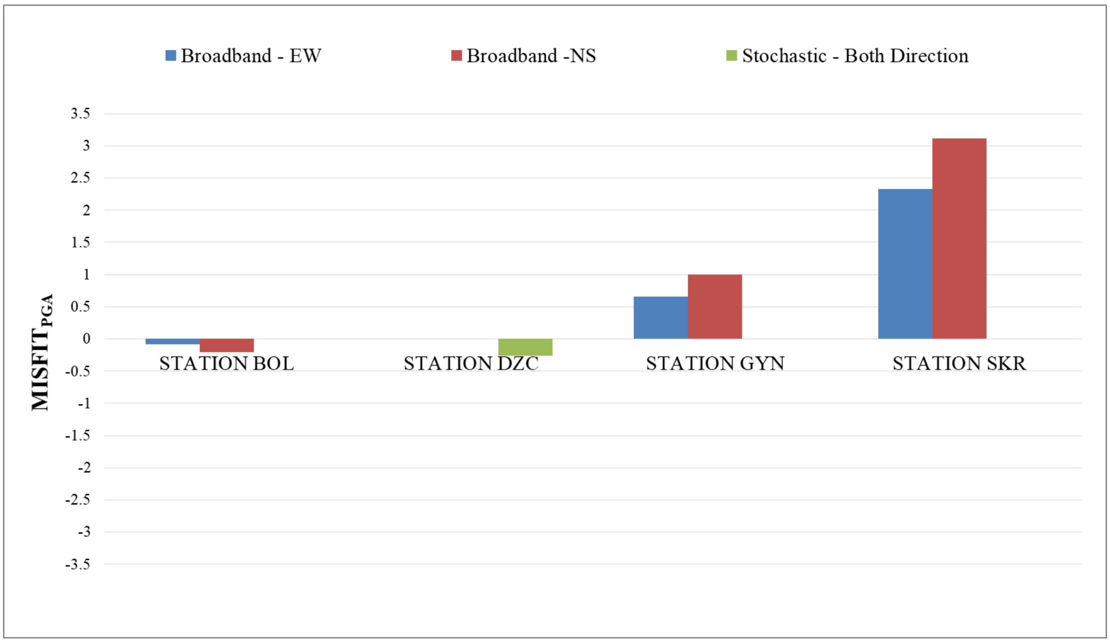

Figure C.3. PGA misfit comparisons of real and simulated records for E-W and N-S components – all stations

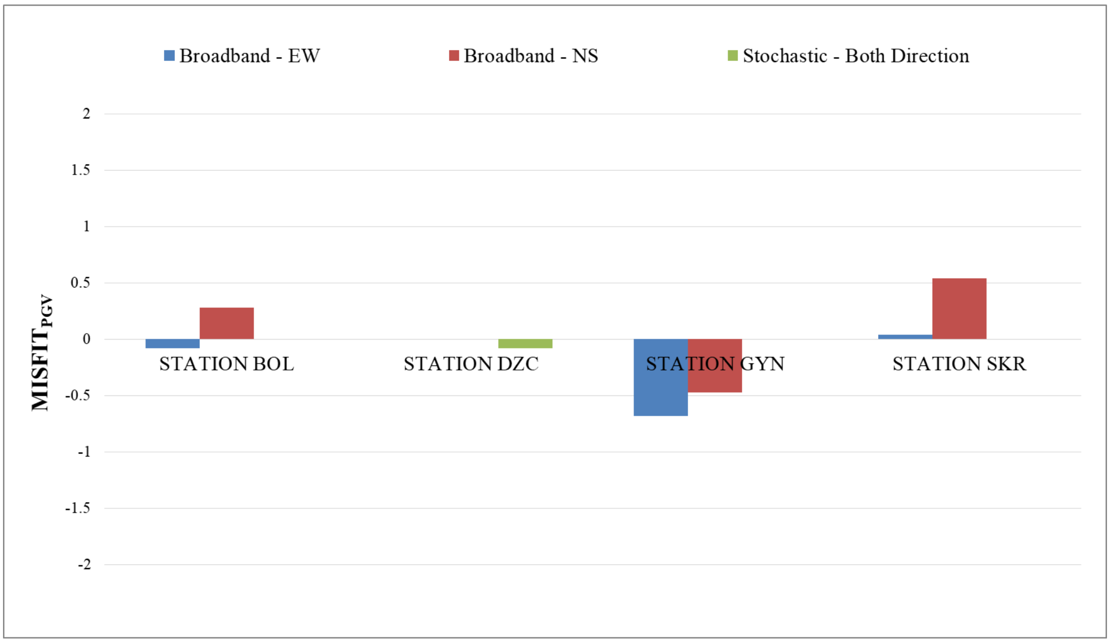

Figure C.14. PGV misfit comparisons of real and simulated records for E-W and N-S components – all stations

CURRICULUM VITAE

PERSONAL INFORMATION

Surname, Name	: Özmen, Ekin
Nationality	: Turkish (TC)
Date and Place of Birth	: 22 October 1990, Ankara
Phone	: +90 506 403 94 10
E-mail	: ekin.ozlu@metu.edu.tr

EDUCATION

Degree	Institution	Year of Graduation
BS	METU Civil Engineering	2014
Minor Program	METU German Language	2013
High School	Hacı Ömer Tarman High School, Ankara	2008

WORK EXPERIENCE

Year	Place	Enrollment
2019-Present	Yüksel Proje Uluslararası A.Ş.	Bridge Engineer
2018-2019	Fhecor Ingenieros Consultores	Bridge Engineer
2015-2018	Deha Proje Eng. And Con. Ltd. Co.	Bridge Engineer
2014-2015	Es Proje Design Eng. Con. Ltd. Co.	Structural Engineer
2014-2014	Yolsu Engineering Services Ltd. Co.	Structural Engineer
2012 July	University of Kassel Civil Eng. Dep.	Intern Earthquake Engineering Student
2011 July	METU Civil Eng. Dep.	Intern Civil Engineering Student

FOREIGN LANGUAGES

Advanced English, Fluent German.

HOBBIES

Pixel art, Traveling, Poetry.